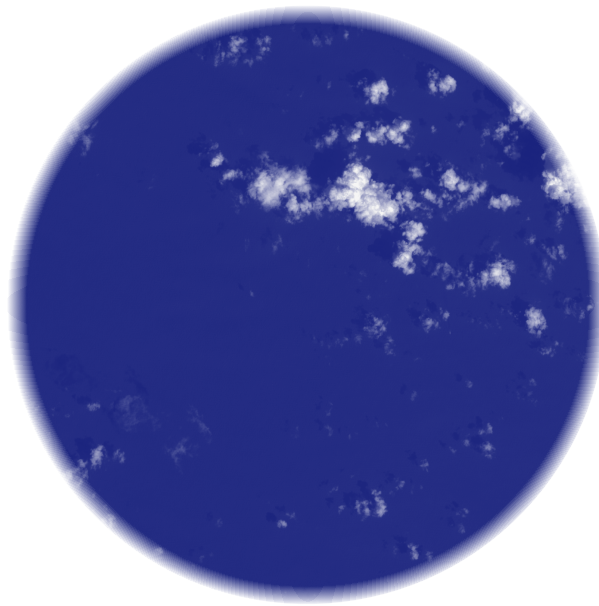


SMALL AND OPTICALLY THIN CLOUDS IN THE TRADES



Dissertation
with the aim of achieving a doctoral degree
at the Faculty of Mathematics, Informatics and Natural
Sciences Department of Earth Sciences
at Universität Hamburg

Submitted by Theresa Mieslinger
from Schwäbisch Gmünd, Germany

Hamburg, 2021

Accepted as Dissertation at the Department of Earth Sciences

Day of oral defense:

01.10.2021

Reviewers:

Prof. Dr. Stefan A. Buehler

Prof. Dr. Bjorn Stevens

Chair of the Subject Doctoral Committee:

Prof. Dr. Hermann Held

Dean of Faculty of MIN:

Prof. Dr. Heinrich Graener

A cloud is made of billows upon billows upon billows that look like clouds. As you come closer to a cloud you don't get something smooth, but irregularities at a smaller scale.

— Benoit Mandelbrot

The front cover shows a small snapshot of an ASTER image showing bright trade cumulus clouds (white) over the dark tropical ocean (blue color).

This document was typeset using the classicthesis template developed by André Miede and Ivo Pletikosić available at: <https://bitbucket.org/amiede/classicthesis/>.

ABSTRACT

The trades and the inherent trade cumulus clouds cover large parts of the tropical oceans. Trade cumulus clouds are ubiquitous but also very small in their horizontal and vertical extent posing huge challenges on observing systems such as satellite imagers. Climate models exhibit a significant spread in the response of trade cumulus clouds to global warming motivating their intense study in recent years. Within this thesis, I use high-resolution satellite images to gain new insights on small and optically thin clouds in the trades.

The way trade wind clouds change with surface warming is decisive for their feedback, which defines whether clouds further amplify or dampen the warming of the climate system. Cloud feedback estimates can be investigated from so-called cloud-controlling factors, their relation to cloud properties in the current climate and their change with global warming. Results from my first study indicate a wind-speed driven boundary layer in the trades. The surface trade winds show the most powerful control on cloud properties such as cloud sizes, top heights or cloud clustering. Furthermore, the Bowen ratio was firstly tested from observations and emerges as a potential new control factor. Trade cumulus cloud properties also show a susceptibility to the sea surface temperature and the stability of the lower troposphere which are both projected to change in a warming climate and may thus impact cloud feedbacks.

Investigating cloud-controlling factors is an ongoing task and seems to be within reach from extensive measurements of the recent field campaign EUREC⁴A. First analysis of cloud observations from multiple instruments indicate the frequent occurrence of not only small, but also optically thin clouds. Due to their low reflectance, such clouds are challenging to detect from passive imagers. High-resolution imagers are able to detect small clouds, but, do conventional satellite cloud products still miss optically thin clouds?

Within another study, I follow a new approach for defining the total cloud cover consisting of clouds detected by conventional cloud masking schemes and of undetected optically thin clouds. By simulating the well-understood clear-sky signal I can extract clouds as a residual from the all-sky observation and circumvent conventional but problematic thresholding tests in cloud masking schemes. From evaluating a high-resolution satellite dataset collected during EUREC⁴A, I find that optically thin clouds contribute 45 % to the total cloud cover and reduces the average cloud reflectance by 29 %. Undetected optically thin clouds can have major implications for estimates of the radiative effect of clouds and thus, cloud feedbacks.

ZUSAMMENFASSUNG

Die Passatwind-Region und die dort heimischen Cumulus-Wolken bedecken große Teile unserer tropischen Ozeane. Passatwolken sind omnipräsent aber auch sehr klein in ihrer horizontalen und vertikalen Ausdehnung und stellen somit eine große Herausforderung für Beobachtungssysteme wie beispielsweise Satellitenaufnahmen dar. Klimamodelle sind sich uneins darin wie sich Passatwolken mit der Erderwärmung verändern. Diese Uneinigkeit intensivierte die Erforschung der Wolken in den letzten Jahren. In der vorliegenden Arbeit verwende ich daher hochauflösende Satellitenbilder, um neue Erkenntnisse über kleine und optisch dünne Wolken in der Passatwind-Region zu gewinnen.

Die Art und Weise, wie sich Passatwolken mit der Oberflächenerwärmung verändern, ist entscheidend für ihre Rückkopplung. Die Rückkopplung wiederum bestimmt, ob Wolken die Erwärmung des Klimasystems weiter verstärken oder dämpfen. Schätzungen der Wolkenrückkopplung können anhand sogenannter wolkenkontrollierender Faktoren, ihrer Beziehung zu den Wolkeneigenschaften im aktuellen Klima und ihrer Veränderung mit der globalen Erwärmung untersucht werden. Die Ergebnisse meiner ersten Studie deuten auf eine windgesteuerte Passat-Grenzschicht hin. Die Passatwinde an der Oberfläche zeigen den stärksten Einfluss auf die Wolkeneigenschaften wie beispielsweise die Wolkengrößen, die Höhe der Wolkenobergrenze oder die Clusterbildung. Außerdem wurde das Bowen-Verhältnis zum ersten Mal anhand von Beobachtungen getestet und zeichnet sich als potenzieller neuer Kontrollfaktor ab. Darüber hinaus zeigen die Eigenschaften von Passatwolken eine Empfindlichkeit gegenüber der Meeresoberflächentemperatur und der Stabilität der unteren Troposphäre, welche sich beide in einem sich erwärmenden Klima ebenfalls ändern dürften und somit Auswirkungen auf die Rückkopplung von Wolken haben können.

Die Untersuchung der wolkensteuernden Faktoren ist eine fortwährende Aufgabe und scheint nach den umfangreichen Messungen der jüngsten Messkampagne EUREC⁴A in Reichweite zu sein. Erste Analysen von Wolkenbeobachtungen aus mehreren Instrumenten zeigen das häufige Auftreten von nicht nur kleinen, sondern auch optisch dünnen Wolken. Aufgrund ihres geringen Reflexionsgrades sind derartige Wolken mit passiven Sensoren nur schwer zu erkennen. Mit hochauflösenden Imagern sind wir in der Lage, kleine Wolken zu sehen. Aber verpassen herkömmliche Satellitenwolkenprodukte dennoch die optisch dünnen Wolken?

In einer weiteren Studie verfolge ich einen neuen Ansatz zur Definition einer Gesamtbewölkung, die sich aus Wolken, welche durch konventionelle Wolkenerkennungsverfahren bestimmt werden, und aus nicht erkannten optisch dünnen Wolken zusammensetzt. Die Idee dabei ist, das Signal einer wolkenfreien Beobachtung zu nutzen, um die Wolken selbst als Residuum zu extrahieren. Durch Simulieren

einer wolkenfreien Beobachtung kann das Signal der Wolken selbst als Residuum extrahiert werden. Die Methodik umgeht elegant die problembehafteten Schwellenwerttests in konventionelle Wolkenerkennungsverfahren. Durch die Auswertung eines hochauflösenden Satellitendatensatzes finde ich heraus, dass optisch dünne Wolken 45 % zur gesamten Wolkenbedeckung beitragen und die durchschnittlichen Helligkeit der Wolken um 29 % reduzieren. Unentdeckte optisch dünne Wolken können große Auswirkungen auf die Schätzung des Strahlungseffekts von Wolken haben und damit auch auf die Wolkenrückkopplung.

PUBLICATIONS

The following publications are part of this dissertation. Publications as first author are included in the appendices:

APPENDIX A

Mieslinger, T., Horváth, Á., Buehler, S. A., and Sakradzija, M. (2019). The dependence of shallow cumulus macrophysical properties on large-scale meteorology as observed in ASTER imagery. *Journal of Geophysical Research: Atmospheres*, 124, 11477–11505. <https://doi.org/10.1029/2019JD030768>

APPENDIX B

Mieslinger, T., Stevens, B., Kölling, T., Brath, M., Wirth, M., and Buehler, S. A.: Optically thin clouds in the trades, *Atmos. Chem. Phys. Discuss.* [preprint], <https://doi.org/10.5194/acp-2021-453>, in review, 2021.

Further publications related to this dissertation with co-authorship:

Stevens, B., Bony, S., Farrell, D., and 290 co-authors: EUREC4A, *Earth Syst. Sci. Data Discuss.*, 2021, 1–78, <https://doi.org/10.5194/essd-2021-18>, 2021.

Konow, H., Ewald, F., George, G., Jacob, M., Klingebiel, M., Kölling, T., Luebke, A. E., **Mieslinger, T.**, Pörtge, V., Radtke, J., Schäfer, M., Schulz, H., Vogel, R., Wirth, M., Bony, S., Crewell, S., Ehrlich, A., Forster, L., Giez, A., Göttsche, F., Groß, S., Gutleben, M., Hagen, M., Hirsch, L., Jansen, F., Lang, T., Mayer, B., Mech, M., Prange, M., Schnitt, S., Vial, J., Walbröl, A., Wendisch, M., Wolf, K., Zinner, T., Zöger, M., Ament, F., and Stevens, B.: EUREC4A's HALO, *Earth Syst. Sci. Data Discuss.* [preprint], <https://doi.org/10.5194/essd-2021-193>, in review, 2021.

ACKNOWLEDGMENTS

This is it — tropical cumuli are what I want to work on!

— Joanne Simpson

Just like Joanne Simpson, I started overly enthusiastic into this PhD. And I would like to sincerely thank my PhD advisors Stefan A. Buehler, Cathy Hohenegger, and Bjorn Stevens for listening to my ideas, taking the time and interest in my projects, and also for sorting them out when needed. I am especially grateful for Bjorn's idea for the second study that I had so much fun with. Thanks for your scientific input, enriching discussions at any given day- or nighttime and your contagious enthusiasm about clouds. I'd further like to thank Stefan for allowing me to participate in such a wonderful and exciting field campaign as EUREC⁴A. EUREC⁴A was a game changer in my PhD and I will never forget the moment when we were flying above a thin cloud layer that the radar was blind to while the lidar beam fought against its attenuation.

Two working groups supported me during my PhD, the Radiation and Remote Sensing group at UHH and the Tropical Cloud Observations group at MPI. I would like to thank all members for providing constructive feedback and posing questions that were often on the point and helped me develop my projects. Another group I am indebted to is the IMPRS office team consisting of Antje, Connie, and Michaela who paved the way through the administrative landscape of my stipend. I especially want to thank Antje for comforting afternoons with coffee and cookies, negotiation tips and career ideas. Antje, I will definitely stop by at your garden in Bremen this summer!

I am incredibly grateful for all of my wonderful office mates starting with Elina, Freddy, and Lukas until Corona split us apart, and lately my (home) office mate Tobi. Thank you so much for your patience and for never being openly frustrated by my repetitive questions about computers, models and the world! In particular, I am most thankful to Lukas and Tobi. You both gave me the possibility to greatly improve my programming and IT skills in so many ways ranging from docker images, python classes, and opendap protocols all the way to programming webpages. You are the best idea-to-code translators and no neuronal network will ever be able to replace you! Neuronal networks also cannot drink beers.

Over the years I talked to many people from in- and outside of my work environment that supported me in one or the other way. Looking back, I realized that I definitely have to mention Heike Konow here for introducing me to the right people at the right time. Also, I am very grateful for inspiring discussions on clouds and radiation with Robert Pincus, Bernhard Mayer, Fabian Jakub, Ákos Horváth, Mirjana, Sakradzija, Martin Wirth, and Jean-Louis Dufresne.

More recently, I received so much help from Lukas, Freddy, Tobi, Anne, Anna Lea, Theresa, and Geet who provided feedback on parts of this dissertation at various stages. Thank you all for your constructive feedback, and the smilies and nice words that kept me going. The readers of this dissertation will surely appreciate it. I would further like to thank Freddy for his encouragement, advice, and some really cool technical tricks, Lukas for teaching me irony, Theresa for two amazing weeks on Barbados as team T², Anne for the "probabilistic" Friday talks on land slides and clouds, and Anna Lea for those wonderful talks on how we think about the trades and about life in general during a nice bike ride through Altes Land. Two people deserve an extra note, my MPI colleagues and dear friends Geet and David. Thank you so much for our bi-weekly *selfis* (semi-lonely friends in science) meetings and the comforting and motivating words whenever the workload seemed frightening.

Last but not least, I am very grateful for having such a nice group of friends and family. In particular, I would like to thank my flatmates Karo, Tarek, and Domme for bearing with me during those intense and exciting times. Thanks to the whole Wilhelmsburg community and the IMPRS friends for those many nice evenings on the dike and "beim Portugiesen", the biking trips, and other fun activities that gave me such a great time. Thanks to my parents, grandparents, sisters and the whole family for believing in me and my work despite knowing little about my faraway big-city life. It remains to thank Tobi again. Thank you for being the happiest person on Earth! And for your great idea to organize another sailing trip that particularly motivated me to finish this thesis now.

CONTENTS

I UNIFYING ESSAY

1	INTRODUCTION	3
1.1	Trade cumulus clouds and their role in global climate	3
1.2	History of cloud observations	5
1.3	Outline of this thesis	7
2	PROPERTIES OF TRADE CUMULUS CLOUDS AND THEIR CONTROLLING FACTORS	9
2.1	Solving the mystery of a spread in cloud size distribution measures	11
2.2	Large-scale cloud-controlling factors	14
3	CLOUD OBSERVATIONS DURING EUREC ⁴ A	19
3.1	The EUREC ⁴ A ASTER dataset	20
3.2	HALO cloud cover observations	21
4	OPTICALLY THIN CLOUDS IN THE TRADES	25
4.1	Identifying optically thin clouds in ASTER observations	26
4.2	Total cloud cover and cloud reflectance	28
4.3	Implications of optically thin clouds	29
5	SUMMARY AND CONCLUSION	31
5.1	Results in a nutshell	31
5.2	Outlook	33

II APPENDIX

A	THE DEPENDENCE OF SHALLOW CUMULUS MACROPHYSICAL PROPERTIES ON LARGE-SCALE METEOROLOGY AS OBSERVED IN ASTER IMAGERY	37
A.1	Introduction	39
A.2	Data and Methods	42
A.2.1	ASTER Imagery	42
A.2.2	ASTER Cloud Mask and Cloud Object Labeling	43
A.2.3	Fractal Dimension	45
A.2.4	Cloud Size Distribution	46
A.2.5	Cloud Spatial Distribution	48
A.2.6	Cloud Top Height	51
A.2.7	ERA-Interim Reanalysis and MODIS data	51
A.2.8	Analysis Method	52
A.3	Statistical Overview of Cloud Field Properties	53
A.3.1	Cloud Fraction, Cloud Top Height, Cloud Spatial Distribu- tion, and Fractal Dimension	53
A.3.2	A Critical View of the Power-Law Fitting of Cloud Size Dis- tributions	56
A.4	Relations of Cloud Field Properties to Large-scale Meteorological Parameters	61

A.4.1	Lower-Tropospheric Stability and Subsidence	61
A.4.2	Sea Surface Temperature and Moisture	63
A.4.3	Surface Easterly Trade Winds	64
A.4.4	Bowen Ratio	68
A.4.5	Schematic Summary of Observed Correlations	69
A.5	Summary and Conclusions	69
A.6	Appendix	72
A.6.1	Dependence of scaling parameters on cloud size measure and binning method	72
B	OPTICALLY THIN CLOUDS IN THE TRADES	85
B.1	Introduction	87
B.2	Observations	89
B.2.1	The ASTER dataset for EUREC ⁴ A	89
B.2.2	WALES airborne lidar measurements	90
B.2.3	Surface wind speed estimates	91
B.3	Methodology	92
B.3.1	A simplified clear-sky model (SCSM)	92
B.3.2	Identifying optically thin clouds in all-sky observations	94
B.3.3	Robustness of optically thin cloud estimation	97
B.4	Results	100
B.4.1	Visualizing optically thin clouds in an ASTER image	100
B.4.2	The OTC equivalence in Lidar data	101
B.4.3	The contribution of OTC to the total cloud cover	103
B.4.4	The cloud reflectance - cloud cover relationship in ASTER observations	106
B.5	Discussion	108
B.5.1	Implication for CRE estimates	109
B.5.2	Optically thin clouds in the aerosol-cloud interaction context	110
B.6	Conclusions	111
B.7	Appendix	113
B.7.1	Components and equations to the simple clear-sky model (SCSM)	113
B.7.2	Derivation of the clear-sky fraction	118
	BIBLIOGRAPHY	121

ACRONYMS

AOD	aerosol optical depth
ASTER	Advanced Spaceborne Thermal Emission and Reflection Radiometer
CALIOP	Cloud-Aerosol Lidar with Orthogonal Polarization
CCF	cloud-controlling factor
CRE	cloud radiative effect
CMIP	Coupled Model Intercomparison Project
EUREC4A	Elucidating the Role of Cloud-Circulation Coupling in Climate
GOES	Geostationary Operational Environmental Satellite
HALO	High Altitude and Long-range Research Aircraft
ICON	Icosahedral Nonhydrostatic Weather and Climate Model
LES	large-eddy simulation
LTS	lower-tropospheric stability
MODIS	Moderate-resolution Imaging Spectroradiometer
NASA	National Aeronautics and Space Administration
SST	sea surface temperature
WALEX	Water Vapor Lidar Experiment in Space demonstrator
WCRP	World Climate Research Programme

Part I

UNIFYING ESSAY

Within the unifying essay I will motivate and describe accomplishments from my PhD work on trade cumulus clouds. The introduction provides an overview on trade cumulus clouds as well as background knowledge to the studies and publications related to this dissertation. The following chapters describe the gained scientific insights from studying trade cumulus clouds in high spatial resolution observations from space as well as from airborne observations during the recent field campaign ELUcidating the RolE of Cloud-Circulation Coupling in ClimAte ([EUREC4A](#)).

INTRODUCTION

*The cumulus cloud is the queen of beauty
in the realm of the atmosphere.*

— Herbert Riehl

The introduction will guide the reader through the basics that motivate this dissertation and it provides context to the two main studies summarized in chapter 2 and 4. I will start with the story of the trades and the history and innovations in cloud observations that pave the way to investigating trade cumulus clouds and lead to the main research objectives of this dissertation.

1.1 TRADE CUMULUS CLOUDS AND THEIR ROLE IN GLOBAL CLIMATE

The trades enfold Earth's equatorial trough region from about 30 °S to 30 °N and are famous for their prevailing easterly winds at the surface that fostered global trade by opening ways for explorers to sail between continents. Early maps showing the surface winds over the ocean basins date back to Edmond Halley in 1686 (Halley, 1686). However, the theory behind this persistent wind pattern was first successfully formulated in 1734 by George Hadley in his article on the cause of the general trade winds (Hadley, 1734). Till date, the trade winds are seen as part of a larger atmospheric circulation pattern, the Hadley circulation, which describes rising air masses near the equator, their redirection to the poles at the tropical tropopause, the enhanced cooling and sinking of those air masses with increasing distance to the equator, and a backward flow to the equator at the surface in form of the easterly trade winds. The sketch in Fig. 1.1 illustrates the Hadley circulation together with the inherent clouds.

The clouds in the trades grow in an environment that is characterized by a strong subsidence and a stable troposphere. While areas of large-scale subsiding air masses over continents produce the largest deserts on Earth, subsidence areas over ocean show a rich collection of clouds and cloud formations (Malkus and Riehl, 1964; Stevens et al., 2019). Fundamental to all convective processes in the atmosphere is the heating of the surface by shortwave solar radiation and the cooling of the atmosphere by longwave radiation creating an instability through radiative imbalance. This instability is balanced by convection. Surface heat and moisture fluxes transport moisture from the ocean reservoir upwards forming low and shallow trade cumulus clouds. Trade cumulus clouds are part of the so-called

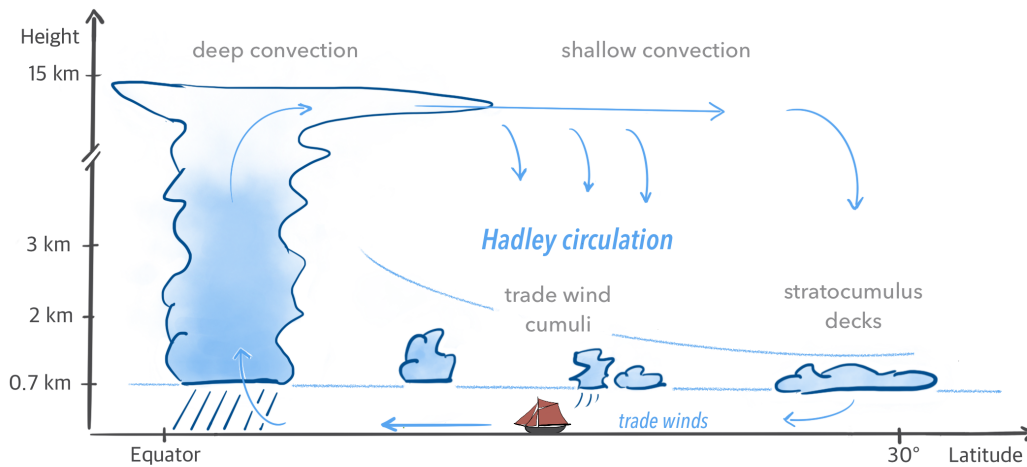


Figure 1.1: Sketch showing the Hadley circulation (blue arrows) with deep convection at the equator, shallow convection due to subsidence in the trade wind region, and the prominent trade winds at the surface.

marine low clouds which typically exhibit a low base and low thickness and cover as much as 18 % of the Earth (Myers et al., 2021). Viewed from space, small cumuli cloud resemble popcorn and their distribution might be best imagined as if a bucket of popcorn was emptied over a small lake such as the Außenalster in Hamburg.

Trade cumulus clouds play an important role in the context of global energy balance and climate projections. While the net cloud radiative effect of deep convection is about zero, the trade cumulus clouds as part of marine low clouds have a net cooling effect on Earth's energy budget (Hartmann and Short, 1980). However, how trade wind clouds change in a warming climate is highly uncertain. Several studies in the past have shown that the poor understanding of marine low clouds leads to a large disagreement among modelled climate projections as well as to a large disagreement between observations and modelled current climate in the trades (Bony and Dufresne, 2005; Vial, Dufresne, and Bony, 2013; Zelinka et al., 2020). The most recent Coupled Model Intercomparison Project (CMIP) phase 6 shows a significant model spread in low cloud response to warming in the trades, albeit to a somewhat reduced extent than in previous intercomparison projects (Zelinka et al., 2020).

A better understanding of the change in trade cumulus clouds as quantified by their cloud feedbacks was one of the goals formulated in the World Climate Research Programme (WCRP)'s grand challenge on "Cloud, Circulation, and Climate Sensitivity" (Bony et al., 2015) and fostered several research projects within recent years. Cloud feedbacks quantify the change in radiative balance at the top of atmosphere due to a change in cloud properties that is induced by global surface warming. The sign of cloud feedbacks defines whether the change in cloud properties will amplify (positive) or dampen (negative) the perturbation and is

therefore of main interest. The CMIP6 multi-model mean cloud feedback in the trades is positive meaning that trade cumulus clouds amplify global warming through a reduction in their cooling effect. However, similar to earlier CMIPs, the models largely disagree on the change in cloud properties.

Can we use observations to constrain cloud feedbacks? We would like to be able to tell, which climate projections and the respective models are more plausible and which are less. The impact of clouds on the radiation balance is quantified by the cloud radiative effect (CRE) which is predominantly a function of the cloud cover and cloud brightness. Climate models tend to represent the current CRE correctly but for compensating biases - they underestimate cloud cover while they overestimate cloud brightness ("Too few, too bright"-bias, Nam et al., 2012; Klein et al., 2013). The CRE is strongly linked to cloud feedback and the aforementioned biases are thought to amplify the spread in cloud feedback and climate sensitivity estimates in climate models (Brient and Bony, 2012; Nam et al., 2012). Further observational constraints of current trade wind cloud cover and cloud brightness may provide insights on model biases and help improve cloud feedback estimates.

In recent years, another approach in studying cloud feedbacks emerged wherein cloud feedbacks are decomposed into a factor describing the change of the large-scale atmospheric environment with warming and a second factor that describes the influence of those factors on cloud properties (Klein et al., 2018; Myers and Norris, 2016; Qu et al., 2015). The approach is rooted in the idea that climate models agree on the former, while they strongly disagree on the latter part. However, we can use observations to constrain the latter part, that is, how cloud properties change with an extensive set of environmental factors or so-called cloud-controlling factors (CCFs). A better understanding of the sensitivity of cloud properties to CCFs from observations in the current climate may bridge the gap to an improved cloud representation in a warmer climate. Accurate cloud observations are thus at the core of all investigations and some insights on possibilities and challenges in the realm of observations are provided in the following.

1.2 HISTORY OF CLOUD OBSERVATIONS

Clouds have fascinated people since time immemorial. One of the earliest documented observations of weather and clouds goes back to Aristotle. Around 340 BC, he named clouds and all other parts floating in the air as meteors, thus creating the term meteorology. While philosophers and artists depicted clouds as divine creatures for a long time, scientific observation came to the foreground around 1800. It was the age of scientific description of nature and everything seemed explainable despite the constant change to which nature seemed to be subject. The English pharmacist Luke Howard was the first to classify the basic cloud forms *cumulus*, *stratus* and *cirrus* (Howard, 1803), which decisively influenced the first Cloud Atlas

published in 1890 in Hamburg. The authors state that "It is hardly possible to give a sufficient verbal definition of such indeterminate and changeable forms as those of the clouds; graphical representations are therefore requisite" (Hildebrandsson, Köppen, and Neumayer, 1890). The Latin term *cumulus* means "heaped", describes any kind of clustered cloud, and prevailed over terms in other languages and cultures such as *sheep sky* / *clouds* in French and German, *mackerel sky* in English, and *celestial cobblestone* in Spanish.

While the cloud atlas of the time aimed to standardise ground-based observations by humans, the possibilities for cloud observations have multiplied in the 20th century. Observations of weather and clouds were long bound to land or took place on isolated sea routes by explorers such as Alexander von Humboldt, who may have produced the first global climate analysis in the form of a temperature map. The exploration of the lower atmosphere by aircraft started in the 20th century and the era of weather satellites in 1960, both providing valuable input for the conception, construction and validation of weather and climate models including clouds. Technological progress opened the path to observations of rain and clouds by radars, lidars and spectrometers working at various wavelengths to view different aspects of clouds and cloud fields. While enormous progress has been made in modelling as well as in satellite meteorology to date, it became clear several years ago that a lack of understanding of trade cumulus clouds is still a key aspect preventing the scientific field from making further progress (Bony et al., 2015).

What makes it so challenging to study clouds in the trades? Most native to the trades are cumulus clouds. The definition of cumulus in the most recent version of the International Cloud Atlas goes back to Luke Howard and says "Detached clouds, generally dense and with sharp outlines.[...] Sometimes Cumulus is ragged." (WMO-No. 407, ch. II.3.9.1, p.45¹) The challenge of observing trade cumulus clouds lies in their nature of a typical small extent with fractal, and sometimes fuzzy, edges. As surface-based observations over the ocean are sparse, we often rely on satellite imagery with measurements at 1 km or coarser resolution where clouds with a smaller horizontal extent are unresolved. This poses the question of what resolution is sufficient to investigate trade cumulus clouds from remote sensing. In an early study by Wielicki and Parker (1992) the authors estimate the need for 250 m pixel resolution to study cumulus clouds. Such or higher resolution does not only prevent significant over- or underestimations in cloud cover estimates, it also opens the way to a more in-depth analysis of the fractal nature of cumulus clouds.

A high resolution enables the study of the smallest clouds and their scaling behaviour, that is, the lower end of the distribution of cloud sizes as it was started in early studies by Plank (1969) and Wielicki and Welch (1986) and many more. Cloud size distributions even found their way into cloud parameterization schemes

¹ https://cloudatlas.wmo.int/docs/wmo_407_en-v1.pdf

in recent years (Neggers, 2015). Also, Lovejoy suggested a way to depict the complexity of cloud perimeters based on and motivated by Mandelbrot's theory of fractals (Lovejoy, 1982). Further important parameters characterizing trade cumulus clouds are their top height and spatial clustering. Both are decisive in terms of a change in outgoing longwave radiation due to clouds. The spatial clustering of clouds has been shown to impact the Earth energy balance through a change in outgoing longwave radiation from very dry cloud-free areas (Hohenegger and Stevens, 2016). The clustering in trade cumulus cloud fields can only be investigated from data at high spatial resolution that allows for the detection of distinct cloud objects.

1.3 OUTLINE OF THIS THESIS

To make progress on the shortcomings in cloud representation in models, and to ultimately narrow the range of uncertainty in climate projections in the trades, I exploit the potential of high-resolution passive satellite images from the Advanced Spaceborne Thermal Emission and Reflection Radiometer (ASTER) at 15 m pixel resolution in showing undiscovered details of trade cumulus cloud fields. In chapter 2, I examine properties of trade cumulus cloud fields and their relation to the large-scale meteorological field with the aim to define the most prominent CCFs. Previous similar studies mostly focused on stratocumulus clouds and few investigate explicitly the trade wind region. Also, I go beyond most studies in investigating CCFs not only based on the bulk cloudiness, but view them in light of a range of cloud properties including their sizes, top heights, and spatial clustering. The consideration of various properties makes it possible to confine possible physical mechanisms that regulate the trade wind boundary layer on the basis of observational data.

The study of clouds and their relation to CCFs was one of the key motivations for a recent field campaign EUREC⁴A (Bony et al., 2017; Stevens et al., 2021). Chapter 3 describes my contributions to cloud observations during EUREC⁴A. A proposal for high-resolution satellite observations lead to the collection of images in support of numerous aircraft, ship-based and ground-based observations. I show a first analysis of cloud cover estimates from aircraft and satellite observations. Further, I use the high-resolution satellite observations collected during EUREC⁴A to follow a new approach for investigating cloud cover from a clear-sky perspective in chapter 4. This third study reveals shortcomings in cloud detection that have the potential to impact estimates of the radiative effect of clouds and thus, cloud feedback estimates in the trades.

PROPERTIES OF TRADE CUMULUS CLOUDS AND THEIR CONTROLLING FACTORS

Clouds have an infinite variety of shapes, but a limited number of forms corresponding to different physical processes in the atmosphere which are responsible for their formation and evolution.

— F. H. Ludlam

The large spread in cloud feedback estimates in climate models is decisively determined by the inability of the models to project trade cumulus cloud properties into the future (Bony and Dufresne, 2005; Zelinka et al., 2020). However, the models agree better on the change in large-scale meteorological variables with global warming (Myers et al., 2021). Several studies in the past followed the idea to decompose cloud feedbacks into the susceptibility of cloud properties to large-scale meteorological variables and the change of those with global warming (Klein et al., 2018; Myers and Norris, 2016; Myers et al., 2021; Qu et al., 2015; Stevens and Feingold, 2009). The latter is typically based on model simulations while the huge advantage of this approach lies in the possibility to constrain cloud properties from observations. A crucial part of the approach is a good understanding of the relevant large-scale meteorological variables or so-called cloud-controlling factors (CCFs) that govern trade cumulus cloud properties.

For readers that like to think in equations, the relation of cloud feedback to CCFs is best expressed by a first-order Taylor approximation for the change in radiative balance (F) at the top of atmosphere with global warming, the latter being represented by the global mean surface temperature (T):

$$\frac{dF}{dT} = \sum_i \frac{\partial F}{\partial CCF_i} \cdot \frac{dCCF_i}{dT} \quad i \in \{LTS, SST, \dots\} \quad (2.1)$$

The radiative balance at top of atmosphere is a function of cloud properties, that is macrophysical properties such as cloud cover and microphysical properties which are mostly related to the brightness of clouds or their ability to reflect sun light. The term $\frac{\partial F}{\partial CCF_i}$ is typically assumed to be invariant over time and independent of (T) (Klein et al., 2018). CCFs are meteorological parameters describing the atmospheric environment that the clouds form in and interact with, such as the sea surface temperature (SST), atmospheric moisture, or atmospheric vertical motion. A well-established factor indicating areas of low-level clouds is the mean subsiding motion given by the subsidence rate and the related stability within the lower troposphere. The latter is quantitatively described by the lower-tropospheric

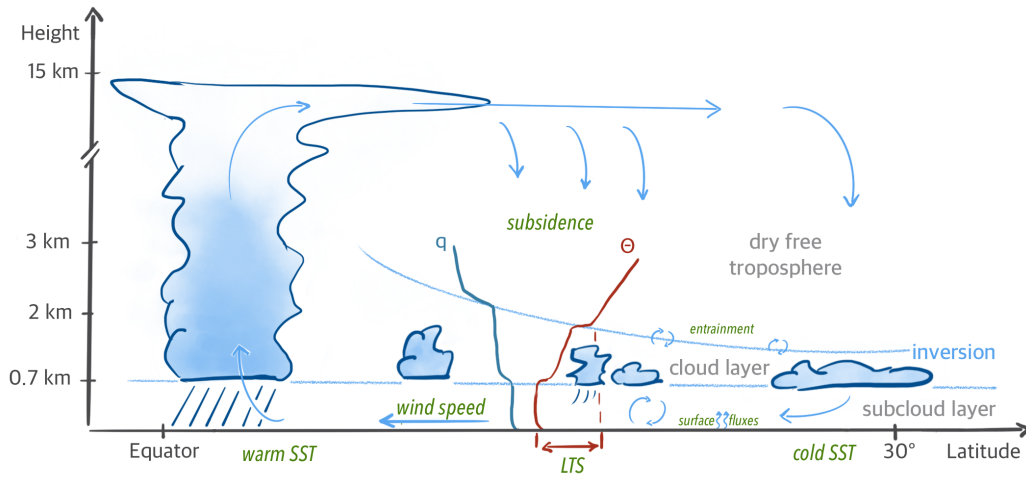


Figure 2.1: Sketch showing the trade wind region together with typical cloud-controlling factors (green letters), among them the sea surface temperature (SST), lower-tropospheric stability (LTS), and the easterly surface trade winds. The general vertical structure is built up by a well-mixed subcloud layer and a cloud layer together forming the trade wind boundary layer. The boundary layer is separated from the dry free troposphere by a strong capping inversion as indicated by jumps in the moisture (q) and potential temperature (Θ) profiles.

stability (LTS), which is the potential temperature difference between 700 hPa and the surface (Klein and Hartmann, 1993; Slingo, 1987). Furthermore, the surface wind speed largely determines the surface moisture and heat fluxes that potentially transport the moisture up above the condensation level and form clouds. Fig. 2.1 illustrates the CCFs that are touched upon within this essay.

Many of the proposed hypotheses concerning CCFs for marine low clouds focus on stratocumulus and only few have been tested explicitly for trade cumulus clouds (Brueck, Nuijens, and Stevens, 2015; Myers and Norris, 2016). Even fewer go beyond studying the cloud cover as a sole measure for cloudiness and do not investigate further cloud properties. Studies that investigate properties of trade wind cumuli from high-resolution imager data demonstrate the general ability of those to observe properties such as the distribution of cloud sizes, their top heights, and their spatial clustering (Benner and Curry, 1998; Cahalan and Joseph, 1989, and many more). Cloud size distributions are of particular interest as they can be used in cloud parametrization schemes in large-eddy simulation (LES) to calculate the mass flux and energy balance within single cloud entities (Neggers, Jonker, and Siebesma, 2003). Furthermore, the boundary layer height, which can be investigated from cloud top heights, is less observed but serves as a key ingredient in hypothesized physical mechanisms regulating the trade wind boundary layer and its clouds. The clustering of clouds is another property of the cloud field that can affect the environment of clouds mainly through intensified rain formation

and through stronger radiative cooling within larger and drier cloud-free areas (Hohenegger and Stevens, 2016; Tobin et al., 2013; Tobin, Bony, and Roca, 2012). Though observational constraints on trade cumulus cloud properties and CCFs have the potential to constrain cloud feedback, previous attempts to relate cloud properties such as cloud sizes to CCFs failed due to a lack of statistical significance from using too few data samples (Zhao and Di Girolamo, 2007).

In the study included in Appendix A, I use an extensive dataset of high-resolution passive satellite observations from ASTER to derive properties of trade cumulus clouds such as their size distribution, cloud top heights, spatial clustering, as well as the cloud cover and show the susceptibility of cloud properties to CCFs. The study goes beyond the statement by Ludham introducing the current chapter by relating the *shapes* of clouds, that is, their sizes and clustering directly to the *physical processes* that we view through the lense of cloud-controlling factors. In terms of cloud properties I focus on cloud macrophysical properties as they are thought to have the stronger impact on a change in the radiative balance compared to microphysical properties such as the cloud optical thickness. The description of cloud properties, in particular cloud size distributions, is largely inconsistent among published studies and requires a detailed assessment in the first place to ensure its robust application. Within the remainder of this chapter I will focus on providing background and explicit answers to the following questions:

- **What causes the spread in proposed scaling behaviours of trade cumulus cloud sizes?**
- **Which cloud-controlling factors and related physical mechanisms known for stratocumulus clouds or suggested from LES studies can be confirmed for trade cumulus clouds?**

The analysis builds upon ASTER images with their exceptional high pixel resolution of 15 m. For further data specifications the reader is referred to Appendix A or chapter 3 where the ASTER dataset collected during the recent field campaign EUREC⁴A is described.

2.1 SOLVING THE MYSTERY OF A SPREAD IN CLOUD SIZE DISTRIBUTION MEASURES

Power laws have been commonly used to describe cloud size distributions in the trades in previous observational (Benner and Curry, 1998; Cahalan and Joseph, 1989; Koren et al., 2008; Zhao and Di Girolamo, 2007) as well as modelling studies (Heus and Seifert, 2013; Neggers, Jonker, and Siebesma, 2003). The frequency of cloud sizes $n(D)$ is proportional to the size D to the power of a scaling parameter b .

$$n(D) \sim D^b \tag{2.2}$$

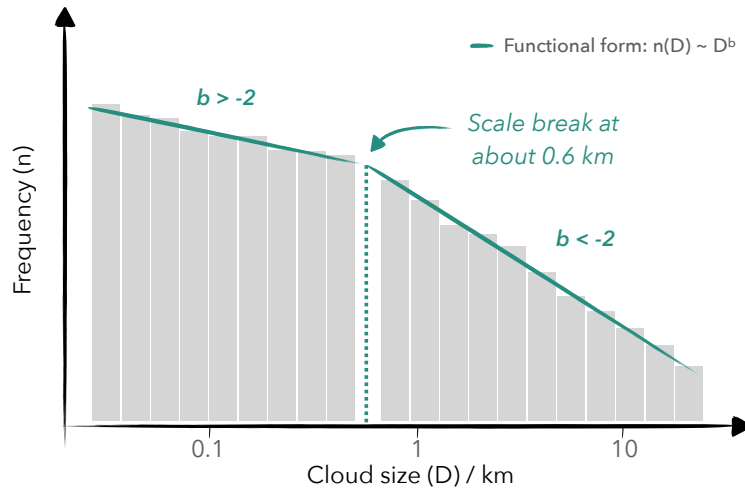


Figure 2.2: Sketch of a typical size distribution of trade cumulus clouds displayed on doubly logarithmic axes.

In practice, the sampling of cloud sizes at the lower end of the distribution is limited by a given data resolution, while limitations on the upper end of the distribution can be subject to poor sampling in limited domains. Though the tails of a distribution are important to prove an actual power law behaviour of clouds, previous studies showed the successful application of power laws to cloud size distributions. In particular, single and double power laws have been proposed that are characterized by their slope or scaling parameters and if applicable, a scale break. Fig. 2.2 shows a sketch of a typical trade cumulus cloud distribution that follows a double power law. The scaling parameters describe the shape of the distribution and are commonly derived from a least-squares linear regression applied to a binned histogram of cloud sizes in a doubly logarithmic diagram. However, the exact shape of trade wind cloud size distributions as described by scaling parameters and scale breaks is largely inconsistent in literature.

Previous studies differ in their derivation of scaling parameters from 1D cloud size measures such as a cloud area-equivalent diameter or cloud length versus 2D cloud areas and also the histogram bins can be equally spaced in the linear or logarithmic space. A transformation of variables can map between the approaches. The derivation of scaling parameters in the logarithmic space is less applied in the literature, but should be favoured as it is more robust and allows the full range of sizes to be taken into account including the noisy upper end of the distribution. Inconsistencies in the range of published scaling parameters may arise from differing fitting strategies, variations in sample size, and lower/upper cutoffs applied to the data. A first-order harmonization of published values is described in detail in Appendix A.3.2.3.

Clouds detected from the [ASTER](#) dataset are in close agreement with the harmonized values and indicate a double power law with the characteristic scaling parameters -1.7 for cloud sizes below and -3.1 for cloud sizes above the scale break size at 0.6 km. The values for cloud sizes refer to the area-equivalent diameter, which is calculated from the cloud area by assuming a perfectly circular cloud. A scaling parameter of -2 would imply the equal contribution of all cloud sizes to the total cloud cover based on the theoretical relation of cloud sizes and their frequency of occurrence to the cloud cover. A smaller value, as it is the case for cloud sizes larger than the scale break size, means that within that range, the smaller clouds contribute more to the total cloud cover. The opposite is the case for clouds which exhibit sizes smaller than the scale break meaning that clouds with sizes at the scale break contribute most to the total cloud cover.

The scale break size was subject to much speculation in the past. While some studies blame it to be an artefact due to insufficient resolution or poor sampling (Heus and Seifert, 2013), early studies by Plank (1969) and by Cahalan and Joseph (1989) relate it to physical mechanisms in the trade wind boundary layer. The authors hypothesize that the most frequent cloud size is constrained by the depth of the trade-wind boundary layer itself. Trade cumulus clouds are often found to exhibit cloud aspect ratios of about one at the scale break size that is close to the size of the largest possible eddies in the boundary layer. Clouds larger than the scale break size tend to have several overshooting tops indicating merged but independent updrafts Cahalan and Joseph (1989). The results from analysing trade cumulus cloud fields in [ASTER](#) observations support the existence of a scale break. Moreover, the scale break seems to be a good indicator for the shape of the cloud size distribution. An increase in the scale break size indicating the relative occurrence of larger clouds consistently leads to higher cloud cover.

Knowing the shape of cloud size distributions from observations, can we learn something about cloud parametrizations? A simple comparison of cloud size distributions from [ASTER](#) observations and high-resolution [LES](#) output shows shortcomings in the simulation of clouds (Fig. 2.3). The scaling of clouds larger than 1.7 km in equivalent diameter agrees well between the observations and simulations on a common grid spacing of about 0.1 km. However, the simulations fail to reproduce the scaling of smaller clouds showing a significant underestimation of the occurrence of small clouds possibly due to too high model diffusion that is related to the effective model resolution. The effective resolution of the Icosahedral Nonhydrostatic Weather and Climate Model ([ICON](#))-[LES](#) was estimated to be eight times the grid spacing in Heinze et al. (2017). The distribution is therefore not representative up to at least about 1.2 km. The [ASTER](#) cloud size distribution suggests that the small clouds which are poorly represented in [LES](#) contribute significantly to the total cloud cover. In particular, 43% of the detected cloud cover is comprised of clouds with diameters below 1.7 km according to the [ASTER](#) observations. High-resolution [LES](#) might benefit from sub-grid parametrizations including an

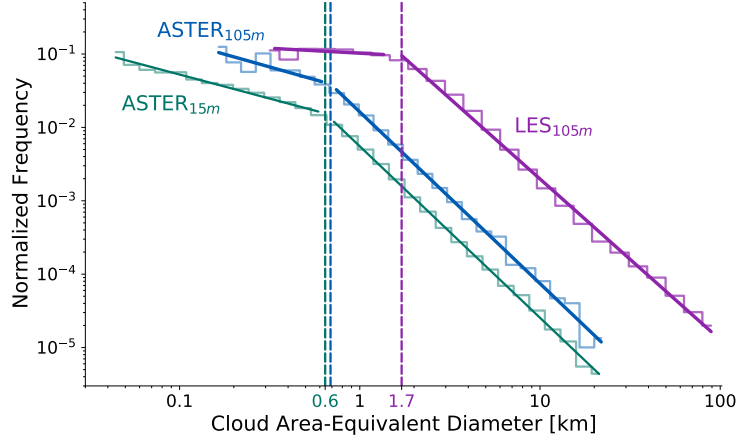


Figure 2.3: Comparison of cloud size distributions from [ASTER](#) observations and [LES](#) output. The [ASTER](#) dataset is a subset of the dataset described in Appendix A restricted to the Atlantic ocean where the [LES](#) domain is located. The high-resolution [ICON-LES](#) simulations are described in Klocke et al. (2017). A threshold of 0.001 kg m^{-2} in liquid water path is applied to the model output to define clouds and calculate their sizes. The distributions from [ASTER](#) observations are shown for the original high resolution as well as derived from a degraded resolution of 105 m to match the grid-spacing of the [LES](#). The [LES](#) original triangular grid is remapped to a regular grid keeping the grid-area approximately constant and resulting in about 103 m grid spacing.

implementation of such a robust feature as a cloud size distribution with a scale break. Including the significant contribution of the smallest clouds to the total cloud cover in models might improve the low-cloud bias and potentially lead to more accurate cloud feedback estimates.

2.2 LARGE-SCALE CLOUD-CONTROLLING FACTORS

Studying the large-scale [CCFs](#) introduced in the beginning of this chapter and sketched in Fig. 2.1, four factors stick out in their strong correlation to cloud properties. I will focus on those factors, namely the [LTS](#), [SST](#), wind speed, and Bowen ratio, while further factors are discussed in detail in the publication in Appendix A chapter A.4.

The most robust mechanism proposed in the literature is the increase in cloud cover with increasing [LTS](#) and the related stronger trade wind inversion (Klein and Hartmann, 1993; Myers and Norris, 2013; Slingo, 1987; Wood and Bretherton, 2006). Physically, a higher [LTS](#) and stronger capping inversion at the top of the trade wind boundary layer reduces the entrainment of dry air at cloud top from the free troposphere into the cloud layer promoting a moister boundary layer. Results from the high-resolution [ASTER](#) dataset support this mechanism by indicating a rate of cloud cover increase with [LTS](#) of about 3 % per K for trade cumulus clouds. This

estimate is lower compared to values reported for stratocumulus clouds (6 % per K, Klein and Hartmann, 1993). While cloud tops remain at about the same height, cloud sizes increase indicating the lateral spreading of clouds at the inversion height.

Cases of high LTS can be caused by strong subsidence. Strong subsiding motion moves air masses fast downwards giving them less time to cool radiatively. As such, they reach the inversion height at a higher temperature compared to weak subsidence and thereby increase the inversion temperature jump and the LTS. While higher LTS favors higher cloud cover, a particularly strong subsidence can move the inversion height below the condensation level and lead to reduced cloud. In the acASTER dataset there is no significant change in cloud properties associated with a change in the subsidence rate possibly due to the opposing mechanisms described above. While the ASTER dataset is representative for the large scale, dynamic factors such as the low-level subsidence have the potential to control the cloud cover in the trades on the meso scale which was recently shown by (George et al., 2021).

The SST is not only subject to strong signals in terms of a warming climate, but has also been shown to drive the breakup of marine stratocumulus to trade cumulus clouds in the tropics suggesting a strong control on low-level cloudiness. The cloud cover is consistently found to decrease when moving from low SSTs at about 30 degree north and south towards higher SSTs at the equator (Klein and Hartmann, 1993; Qu et al., 2015). While previous studies agree on the robust negative correlation of cloud cover to SST, they disagree on the underlying physical mechanisms. Cloud cover and cloud top height estimates from the ASTER dataset support a mechanism proposed by Bretherton and Blossey (2014) where higher SST increases the surface moisture and heat fluxes and intensifies the turbulence. Increased turbulence in the boundary layer increases the mixing of dry free tropospheric air into the cloud layer leading to cloud thinning and lower cloud tops. Lower cloud top heights are indicated by the ASTER dataset, which however stays in contrast to and rules out other proposed mechanisms for example by Rieck, Nuijens, and Stevens (2012).

Most characteristic of the trades are the strong and persistent surface easterly trade winds. As early as 1997, Klein (1997) showed a regulating role of surface winds on the cloud cover that was confirmed by observational and modelling studies (Brueck, Nuijens, and Stevens, 2015; Nuijens and Stevens, 2012) and also found in ASTER observations. In fact, within the frame of the study included in Appendix A, surface wind speed emerges as the strongest CCF. The study by Nuijens and Stevens (2012) explains the influence of wind speed from a bulk theory concept for a wind-speed regulated and non-precipitating trade wind boundary layer that includes a deepening of the boundary layer with increasing wind speed. The regulating role of wind-speed is challenged by a precipitation-governed ansatz described in Bretherton, Blossey, and Jones (2013) which includes a limited deepening response of the trade boundary layer due to precipitation. Both mechanisms

convey the increase of surface fluxes and turbulence with increasing winds which lead to larger clouds. The study of [ASTER](#) observations confirms larger clouds with increasing wind speed and also shows the correlation of larger clouds with higher cloud tops. The latter speaks against the hypothesis of Bretherton, Blossey, and Jones (2013) and indicates the dominance of the wind-speed driven boundary layer concept by Nuijens and Stevens (2012).

Related to the surface wind speed and its driving force on surface fluxes is another potential control factor, the Bowen ratio. The Bowen ratio is the ratio of the surface sensible heat flux to the latent heat flux. A recent study by Sakradzija and Hohenegger (2017) suggests that the Bowen ratio has a major control on cloud sizes and cloud cover by setting the rate of heat and moisture that is transported upwards into the cloud layer and potentially forms clouds. In agreement with their study, the [ASTER](#) observations indicate larger and deeper clouds and a higher cloud cover with increasing Bowen ratio. Those results suggest the Bowen ratio to be a potential new control factor on trade wind cloud properties which merits further investigation.

Though the trade winds seem to strongly influence trade cumulus cloud properties, their influence on cloud feedback is not necessarily given. As explained in the beginning of this chapter, the influence of a [CCF](#) like the trade winds on cloud feedback does not only depend on the sensitivity of cloud properties to the [CCF](#), but also on the change of the [CCF](#) with warming (see Equ. 2.1). In a recent study, Myers et al. (2021) decomposed cloud feedbacks into these two factors. The authors find a strong influence of LTS on the trade cumulus cloud feedback because both the sensitivity of cloud cover to LTS and the change of LTS with warming are large. SST increases with warming and thereby also significantly impacts the cloud feedback. Surface wind speed, on the other hand, do not significantly change in a warming climate, if at all, they might slightly decrease due to a slowdown of the circulation. The strong cloud-controlling mechanism of surface wind speed found in the study in Appendix A seems to have no significant impact on cloud feedback due to the negligible change in wind speed with warming. Mostly based on stability and SST, the study by Myers et al. (2021) suggests an overall marginally positive feedback of trade cumulus clouds which is heavily overestimated by climate models.

It is worth noting that the study in Appendix A is based on averaged quantities resembling climatological or large-scale mechanisms. Similarly, climate models include large-scale cloud-controlling factors while they do not resolve meso-scale cloud organization which however creates distinct cloud patterns in the trades and may impact cloud feedbacks (Bony et al., 2020). Coming back to Ludlam's quote at the beginning of this chapter, we could think of *cloud patterns* as a subgroup to Ludlam's *forms*, the latter being trade cumulus in our case. From a phenomenological inspection of cloud fields viewed from space, the authors of Stevens et al. (2020) defined four distinct cloud patterns in the trades based solely on their visual

appearance. A later study by Bony et al. (2020) shows that trade cumulus cloud scenes can be grouped into those patterns according to their cloud sizes and cluster tendency. Patterns with larger cloud entities seem to emerge under high LTS and strong surface winds, which is in line with the mechanisms discussed above and stated in the literature (Klein and Hartmann (1993); Wood and Bretherton (2006); Appendix A). Bony et al. (2020) highlight the importance of surface winds as a measure to determine the strength of cloud clustering. Strong winds seem to prevent clouds from clustering which is in agreement with analysis of the same clustering index applied to ASTER observations. With a negligible influence of SST on cloud patterns, it is suggested that in a warming climate higher LTS will promote cloud patterns related to higher cloud cover and thus stronger cloud radiative effects (Bony et al., 2020). On the large-scale and even more so on the meso-scale, the dependence of trade cumulus clouds and their cloud patterns to global warming remains uncertain and is subject to ongoing research with numerical simulations as well as the recent field campaign EUREC⁴A.

CLOUD OBSERVATIONS DURING EUREC⁴A

*Experiment is the only means of knowledge at our disposal.
Everything else is poetry, imagination.*

— Max Planck

The field campaign EUREC⁴A (ElUcidating the RolE of Cloud-Circulation Coupling in ClimAte) was motivated by several studies in the past which show shortcomings in cloud representation in models in the trades and propose key question to improve their understanding on the process level, as well as in climate models (Bony et al., 2015, 2017; Stevens and Bony, 2013; Vial et al., 2016). Emerging out of the WCRP's Grand Challenge on Clouds, Circulation, and Climate Sensitivity, EUREC⁴A was designed to test hypothesized cloud-feedback mechanisms including a better understanding of the cloud-controlling factors discussed in the previous chapter 2 and their influence on clouds at the large- and meso-scale (Bony et al., 2017). Also, the extensive measurements were thought to help constrain the modelling of shallow clouds as well as satellite retrievals of cloud products such as cloud cover and cloud optical properties.

EUREC⁴A took place in January and February 2020 on and east of the Atlantic island Barbados in form of a multifaceted collaboration of many nations and institutions working on a diverse range of key questions related to the interplay between clouds, circulation, and climate sensitivity. As part of this huge community effort I lead a proposal for the acquisition of ASTER images in support of the aircraft, ground- and ship-based measurements. The ASTER instrument was originally designed for land studies and digital elevation models and neither does it record images over ocean on an operational basis, nor are operational cloud products available. The EUREC⁴A ASTER proposal lead to the collection of 419 images on 17 days in the area east of Barbados from 7°N to 18°N and from 41°W to 62°W between January 11 and February 19 2020. Each image corresponds to 9 seconds of observation time and covers an area of about 60 km x 60 km stacked together into the north-to-south oriented swaths displayed in Fig. 3.1.

ASTER is mounted aboard Terra, a polar-orbiting satellite in a Sun-synchronous orbit which crosses the latitude of Barbados and the *circle area* roughly at 14:25 UTC, while the tracks further east at about 43°W are observed by ASTER an hour earlier (see Fig. 3.1). The *circle area* is mentioned here representative for the area of the core aircraft observations including extensive remote sensing instrumentation on board the German research aircraft HALO (Krautstrunk and Giez, 2012; instrumentation as described in Stevens et al., 2019). HALO's remote sensing package includes active

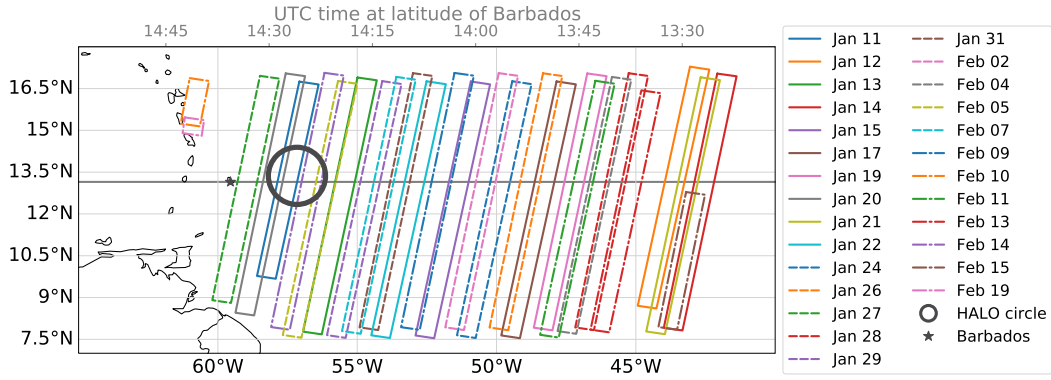


Figure 3.1: **ASTER** dataset during EUREC⁴A with 419 images (60km x 60km) recorded on 17 days between 11 January and 19 February 2020. The High Altitude and Long-range Research Aircraft (**HALO**) research aircraft measured predominantly on the circular path shown in grey on 13 flight days between January 22 and February 15, 2020.

radar and lidar instruments as well as passive imager in the thermal and visual-near infrared range. The latter observes clouds at a resolution comparable to **ASTER**'s 15 m pixel size. The **ASTER** dataset nicely complements the aircraft observations of daytime trade cumulus cloud fields while covering a larger area at similar resolution. Through the **ASTER** proposal, but also through the active participation in ground-based and aircraft observations during the campaign I was able to contribute to the EUREC⁴A overview paper published under Stevens et al. (2021).

3.1 THE EUREC⁴A ASTER DATASET

The **ASTER** images collected during EUREC⁴A are available in form of radiometrically calibrated and geometrically co-registered Level 1B data from National Aeronautics and Space Administration (**NASA**)'s Land Processes Distributed Active Archive Center (LP DAAC). With the aim to make the dataset user-friendly I processed the Level1B data to netCDF files and made them publicly available within the AERIS data archive¹. Additionally included are pixel-based latitude and longitude information, a cloud mask following Werner et al. (2016) and estimated cloud top heights following an infrared-window approach commonly applied to Moderate-resolution Imaging Spectroradiometer (**MODIS**) data (Baum et al., 2012) and described in more detail in Appendix A. The respective python tools designed for processing **ASTER** data are available within the python package *typhon* version 0.8.0, subpackage *cloudmask*². In addition, I split **ASTER** images into tiles such that a full swath on a given day can be easily viewed within the AERIS leaflet

¹ <https://observations.ipsl.fr/aeris/eurec4a-data/SATELLITES/TERRA/ASTER/>

² <https://github.com/atmtools/typhon>

tool³. Data users and cloud-hunters have the possibility to search for meso-scale cloud patterns and zoom in on the rich structures of beautiful trade cumulus clouds.

A time series of cloud cover observed by [ASTER](#) during EUREC⁴A is shown in Fig. 3.2. The cloud cover is based on the mentioned cloud masking scheme by Werner et al. (2016). The algorithm works with thresholds in the visible-near infrared range and splits the measurements into four flags that can be combined into a binary cloud mask with *clear* $\in \{\text{confidently clear, probably clear}\}$ and *cloudy* $\in \{\text{confidently cloudy, probably cloudy}\}$. The campaign average cloud cover based on the binary cloud mask is 0.30 (median 0.17) with higher cloud cover observed in the beginning of the campaign and again towards the end of the campaign (Fig. 3.2 a) and b)).

Interestingly, the cloud size distribution in Fig. 3.2 panel e) shows a scaling behaviour that seems to change twice. The distribution is in good agreement with the analysis and mechanisms stated in chapter 2.1 for sizes above 200 m. Above 200 m larger clouds are also associated with higher cloud tops (panel d)) which is in broad agreement with the results discussed in chapter 2.2. However, the cloud top height retrieval cannot resolve small clouds. The typical cloud base in the trades lies at about 700 m and is rather invariant such that we can expect the scaling of cloud top with cloud size to level out at about 200 m. The change in cloud sizes might be related to the different cloud patterns introduced by Stevens et al. (2020) and investigated further in Bony et al. (2020) and Schulz, Eastman, and Stevens (2021). The smallest clouds may correspond to *sugar*-type clouds while clouds larger than 200 m are more buoyant, grow deeper, and rather correspond to *gravel*-like structures where clouds also start to form clusters.

The [ASTER](#) dataset is planned to be part of a EUREC⁴A satellite data publication that is in preparation. Within that publication we would like to show the diverse range of satellite datasets that have been requested for the campaign period. These will provide new details about trade wind clouds through their high spatial ([ASTER](#)) or temporal (Geostationary Operational Environmental Satellite ([GOES](#))-East) resolutions, as well as information of the cloud top heights (Cloud-Aerosol Lidar with Orthogonal Polarization ([CALIOP](#)), Winker et al., 2009).

3.2 HALO CLOUD COVER OBSERVATIONS

While satellite data typically cover a large area, the advantage of aircraft observations lies in their flexible schedule and in their closer distance to the target object, the clouds, combined with a lower flight speed resulting in high resolution measurements. For example, [HALO](#)'s lidar instrument Water Vapor Lidar Experiment in Space demonstrator ([WALES](#)) (Wirth et al., 2009) retrieves cloud properties at about

³ <https://observations.ipsl.fr/aeris/eurec4a/Leaflet/index.html>

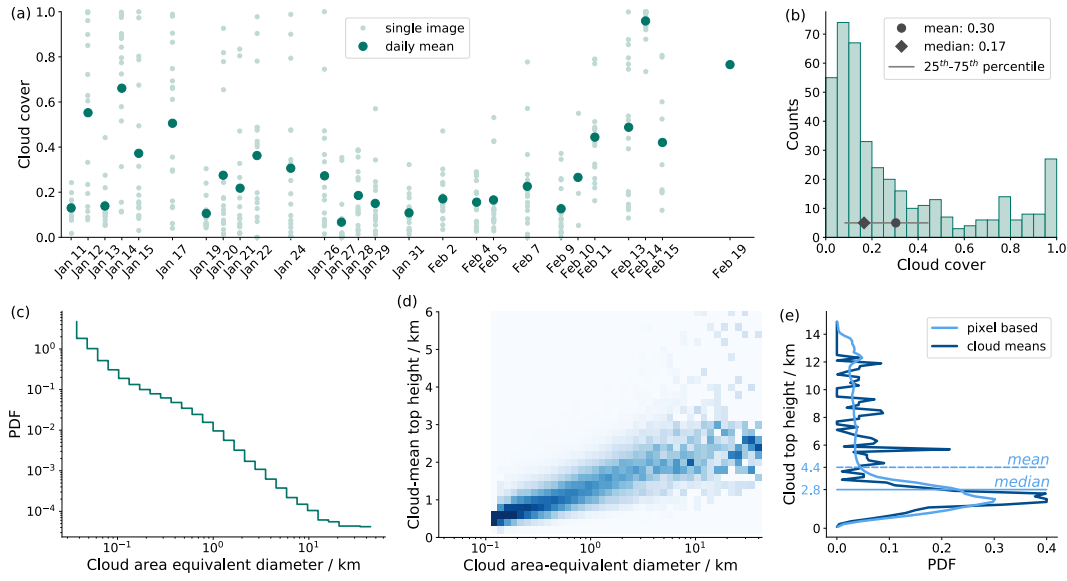


Figure 3.2: Overview on cloud statistics derived from the EUREC⁴A ASTER dataset. Panel (a) shows a time series of cloud cover estimates in January and February 2020 and panel (b) its frequency distribution. Panel (c) shows the distribution of cloud sizes and panel (d) relates those to their cloud-mean top height with all bin counts being normed by the respective sum in individual cloud size bins. Panel (e) shows a frequency distribution of cloud top heights based on pixel values and cloud-means.

40 m horizontal resolution at the typical 200 ms^{-1} aircraft speed while the earlier mentioned CALIOP instrument provides data at 330 m footprint distancing. Also, CALIOP has been shown to struggle detecting low clouds with cloud tops below 1 km altitude (Leahy et al., 2012), while WALES data suggest 29 % of all cloudy measurements to originate from altitudes below 1 km during EUREC⁴A. Within the EUREC⁴A measurement strategy, HALO was tasked to fly at high altitudes of about 10 km on a circular path center at 13.3°N , 57.717°W . HALO carried in total six different sensors designed for cloud observations. Among them are active instruments such as the mentioned lidar and a cloud radar, as well as passive imaging sensors that operate in a range of wavelength bands and at different spatial and temporal resolutions providing a great opportunity to view clouds from different perspectives. The instrument datasets are described in the publication by Konow et al. (2021), to which I was able to contribute with a cloud cover analysis and the development of the so-called "How to EUREC⁴A" book.

For an easy access and convenient usage of HALO's cloud masks as well as further data products related to EUREC⁴A, we, a group of dedicated researchers, started an executable book project that we named "How to EUREC⁴A" ⁴. It consists of code examples and explanatory markdown files that shall guide less experienced users,

⁴ <https://howto.eurec4a.eu>

students and scientists that did not have the fortune to actively participate in the campaign to start their own data analysis. Example scripts show the data access, basic evaluations, as well as convenient data conversions for the respective data products. "How to EUREC⁴A" matured through the contributions from the wider EUREC⁴A community and became part of an effort for a modern data concept where data is accessible via (intake) catalogue structures and can be evaluated "online". This means that example scripts can be run via a **binder** integration such that neither the data nor the scripts have to be downloaded and no programming environment has to be set up. Instead, people can start exploring the data right away.

One chapter of the "How to EUREC⁴A" book shows the evaluation of the HALO cloud mask products⁵. In particular, it includes the Figure 6 from Konow et al. (2021) (with own contributions), which nicely illustrates the variety of measurement principles in two vertical lidar and radar profiles, as well as horizontal imager perspectives in the shortwave and thermal infrared. To make use of the richness of cloud observations, all instrument groups compiled a trinary cloud mask applying thresholds suitable for their instrument and aiming for a best estimate of *cloud free* and *most likely cloudy* areas. Some cloud mask products are based on two thresholds leading to an intermediate *probably cloudy* flag. The instruments disagree on their estimated cloud cover for the full campaign period by a factor of 2.

The subtle differences can be viewed in the cumulative distribution of circle-mean cloud cover estimates shown in Fig. 3.3 and published in Konow et al. (2021), where circle-mean refers to the circle area depicted in Fig. 3.1. The bars in Fig. 3.3 range from the circle-mean minimum to the circle-mean maximum cloud cover frequency expressing the uncertain cases with flag *probably cloudy* by the increasing extent of the bar. A detailed analysis is included in the respective paper, however, I would like to point out a few features. At high cloud cover above 0.6 the instruments agree very well. However, about 90 % of the time cloud cover is estimated to be below 0.6 and about 50 % of the time below 0.2. Here, the instruments largely disagree on the frequency of occurrence depending on their detection principle.

For example, the WALES lidar is able to detect geometrically and optically thin clouds with few condensates leading to generally higher cloud cover estimates. The cloud radar on the other hand is insensitive to small cloud droplets such that low cloud cover situations are most frequent. The passive instruments show varying contributions of *probably cloudy* measurements to the cloud cover indicating the general ability to detect optically thin clouds depending on their respective thresholds and operating wavelengths. The comparison of HALO cloud mask data illustrated the potential of multi-facet measurements in observing clouds while it also indicates (a) that clouds may not exhibit sharp edges and (b) that optically

⁵ <https://howto.eurec4a.eu/cloudmasks.html>

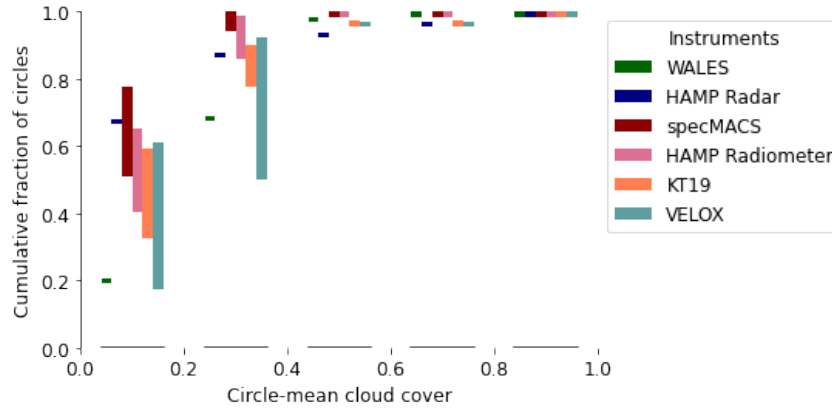


Figure 3.3: Figure from Konow et al. (2021). Cumulative fraction of circle-mean cloud cover estimates. Depending on the instruments named in the legend and some instrument downtimes, the available circle counts range from 64 to 72. The bins on the x-axis have a bin width of 0.2 respectively. The bars span the range defined by the minimum cloud cover based on cloud flag *most likely cloudy* and the maximum cloud cover based on cloud flags *most likely cloudy* and *probably cloudy*.

thin clouds may play a significant role in determining the total cloud cover in the trades. The latter is investigated in detail in the following chapter.

OPTICALLY THIN CLOUDS IN THE TRADES

*Our imagination is struck only by what is great;
but the lover of natural philosophy
should reflect equally on little things.*

— Alexander von Humboldt

The analysis of cloud cover shown in the previous chapter 3.2, as well as previously published studies, suggest that the range of cloud cover estimates from active and passive remote sensing can differ by a factor of 2 even for co-located high resolution data (Konow et al., 2021; Stevens et al., 2019). Despite having a long tradition, estimating cloud cover is subject to inherent measurement differences and the precise definition of cloud boundaries. While active instruments have the advantage of the additional distance-to-object information which facilitates the distinction between background and cloud signal, passive instruments typically use a single threshold to define cloud signals. The large amount of *probably cloudy* measurements from passive sensors in Fig. 3.3 hints to the general ability of those to detect small and optically thin clouds in the trades. Nevertheless, the final estimated cloud cover may largely depend on the chosen cloud-masking thresholds. Is there a way around conventional cloud masking schemes that leads to more comprehensive cloud cover estimates?

In general, passive instruments operating in the visible part of the electromagnetic spectrum detect trade cumulus clouds through their higher reflectivity compared to clear-sky areas with a dark ocean surface. While the radiative effect of clouds is difficult to simulate, the clear-sky signal is well understood in terms of radiative transfer and can be simulated with well-posed approximations. Simulating the clear-sky signal, which would be observed in a scene without clouds, to a given satellite observation provides the possibility to constrain the cloud signal from a clear-sky perspective without any instrument-specific thresholds in cloud masking schemes. Quantifying clouds as a residual to clear-sky has the potential to include weak signals related to optically thin clouds which would otherwise dissolve in the ocean background signal. Based on this new view on clouds, the following questions arise which I will tackle within this chapter:

- **How much of the trade cumulus clouds do we miss in conventional cloud masking schemes?**
- **Do optically thin clouds matter?**

In the following, I will provide a brief overview on a newly developed clear-sky model and the approach taken to translate the simulated clear-sky information to an

actual observation. I apply this new approach for defining a more comprehensive cloud cover to the EUREC⁴A [ASTER](#) dataset described in chapter [3.1](#). The cloud cover estimates in chapter [3.2](#) indicate the general ability of the [WALES](#) lidar to detect optically thin clouds and thus, are included for confirmation from an active sensor. Based on the results, I point out implications that undetected optically thin clouds may have for aerosol-cloud interaction studies and cloud radiative effect estimates. This chapter summarizes the results published within the study included in Appendix [B](#).

4.1 IDENTIFYING OPTICALLY THIN CLOUDS IN ASTER OBSERVATIONS

The clear-sky radiance over ocean can be described by a narrow set of parameters and approximations. Illustratively speaking, the radiation reaching a sensor in space depends on three main components, namely the direct and diffuse sunlight reflected at the surface, as well as the diffuse scattering within the atmosphere (see Fig. [4.1](#)). All three components experience attenuation following Lambert-Beer's law on their way through the atmosphere which depends on the sensor-sun geometry and the scattering material within the atmospheric layer (Stamnes, Thomas, and Stamnes, [2017](#)). The majority of scattering happens at atmospheric aerosols such that the bulk quantity aerosol optical depth ([AOD](#)) is commonly used to approximate the atmospheric scattering and extinction. The third component, the diffuse scattering within the atmosphere in line of sight to the sensor, is treated by including single scattering events. The surface reflection is parametrized with the well-established Cox and Munk model included in a bi-directional reflection function (Cox and Munk, [1954](#)). The scattering within the atmosphere makes use of the Henyey-Greenstein phase function (Henyey and Greenstein, [1941](#)).

The main free parameters of the clear-sky model are the [AOD](#) and a radiance uncertainty that is added to the model output in a post processing step and adds a correction factor to the Cox and Munk parametrization. In the absence of suitable [AOD](#) measurements, an effective [AOD](#) is estimated in an optimization approach. An in depth description of the model can be found in the respective paper in Appendix [B](#) chapter [B.3.1](#) with the explicit written equations. The run-time optimized and vector-based implementation of the simplified clear-sky model¹ is publicly available. Despite numerous approximations, the simplified clear-sky model shows the expected physical behaviour. A sensitivity study with few available clear-sky [ASTER](#) observations results in a good agreement between the probability distributions of simulated and observed pixel reflectances lending confidence in the model's ability to describe the clear-sky signal.

¹ <https://doi.org/10.5281/zenodo.4842675>

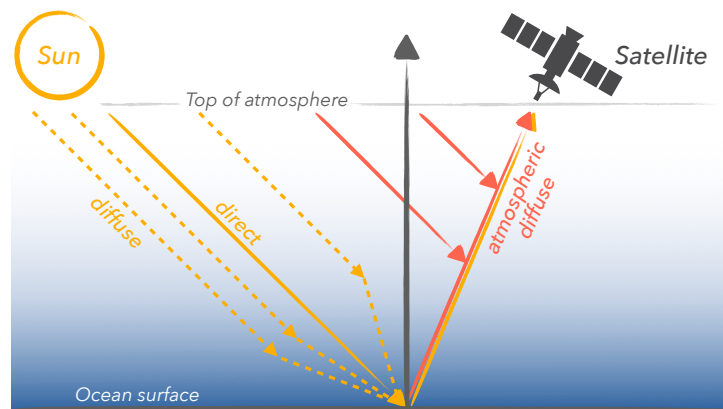


Figure 4.1: Sketch illustrating the main radiance components of the simplified clear-sky model, the direct and diffuse components reflected at the surface (yellow) and the atmospheric diffuse component (red), all being scattered towards a sensor in space.

The gained knowledge from the simulated clear-sky signal can further be translated to the contribution from clear-sky areas within a corresponding all-sky [ASTER](#) observation. The clear-sky model output provides the conditional probability of measuring a reflectance value, given that the observed area would have been cloud-free and given the background conditions of a certain [ASTER](#) observation. An actual [ASTER](#) observation consists of contributions from clear-sky and cloud-related areas. To quantify the clear-sky contribution to this observation, that is, the combined probability of reflectance values, the clear-sky model output needs to be scaled with the clear-sky fraction. The latter is an unknown free parameter that can be estimated from posing a suitable condition. In particular, a conservative approach is followed wherein the clear-sky fraction is maximized within the given physical limits resulting in a minimal contribution by clouds whose effect we aim to quantify. Estimating the clear-sky contribution to the all-sky observation leaves the residual brighter cloud-related areas that are displayed by the light and dark blue areas in the reflectance distribution displayed in Fig. 4.2. Cloud-related areas are partly detected by the [ASTER](#) cloud-masking scheme described in chapter 3.1 and representative for conventional cloud masks. Between the dark ocean surface reflectances and the bright (detected) cloudy reflectances exists a range of cloud-related values of intermediate brightness that I refer to as undetected or optically thin clouds in the following.

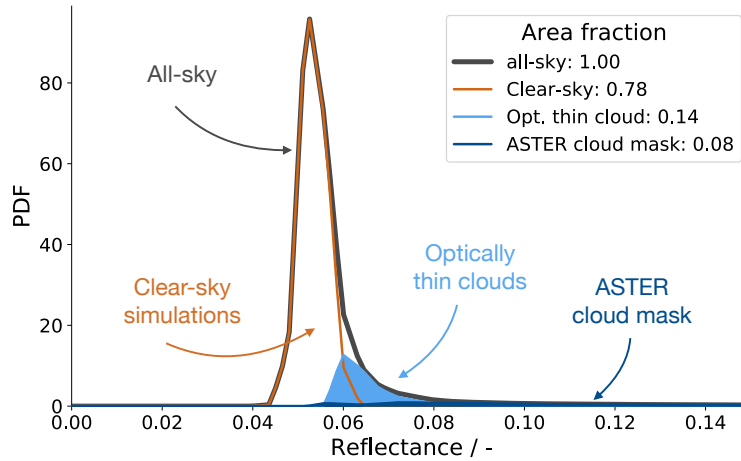


Figure 4.2: Reflectance distribution corresponding to an [ASTER](#) observation recorded on 31 January 2020, 14:08:05 UTC. The information from the simulated clear-sky probability distribution is translated to the all-sky observation. Optically thin clouds (light blue) emerge as a residual when subtracting the combined probability distribution of clear-sky reflectances (orange) and the [ASTER](#) cloud mask reflectances (dark blue) from the all-sky reflectance distribution (dark grey).

4.2 TOTAL CLOUD COVER AND CLOUD REFLECTANCE

Based on the new clear-sky approach, the total cloud cover is estimated to be 0.42 in the reduced EUREC⁴A [ASTER](#) dataset ². 45 % thereof are attributed to optically thin clouds meaning that about half of the total cloud cover is undetected by traditional cloud masking schemes. The amount of optically thin clouds positively correlates with the detected cloud cover up to a total cloud cover of about 0.4 where the scaling saturates. The positive correlation might be a result of anomalously humidified aerosols and cloud fragments surrounding detected clouds combined with a positive correlation of low cloud cover situations and the occurrence of small clouds within respective meso-scale cloud patterns (Bony et al., 2020). On the other hand, situations with total cloud cover above 0.4 often correspond to cloud patterns with larger cloud entities and pronounced clear-sky in between, leaving little space for optically thin clouds (Schulz, Eastman, and Stevens, 2021).

In principle, a brighter surrounding of detected clouds could also result from photons that are reflected at cloud edge or escape the cloud after multiple scattering processes therein. However, lidar measurements such as those by [WALES](#) during EUREC⁴A are less sensitive to such 3D cloud radiative effects and can serve as an independent support for the [ASTER](#)-based results. Based on plane-parallel radiative transfer considerations and including the natural variability in the cloud and ocean background signals, it can be assumed that clouds with optical thickness below

² The methodology builds upon visible clear-sky areas which limits the evaluation of the full [ASTER](#) EUREC⁴A dataset to images with less than 85 % detected cloud cover ([ASTER](#) cloud mask) leaving 395 images for the analysis).

2 do not stand out clearly from the ocean and the [ASTER](#) cloud mask presumably is insensitive to such optically thin clouds. Clouds with optical thickness below 2 are thin enough for a lidar beam to penetrate the cloud such that the backscatter signal can be used to derive a reliable cloud optical thickness value. The EUREC⁴A [WALES](#) dataset measured 0.34 total cloud cover with a 63 % contribution of optically thin clouds. As the fraction of optically thin clouds in [WALES](#) data is even higher compared to the [ASTER](#) analysis, we can assume that scattering of light at cloud edge does not dominate the results and a brighter surrounding of clouds is indeed due to increased reflection from optically thin clouds. Both datasets likewise suggest that large areas of the trades are covered by optically thin clouds leading to a higher total cloud cover than assumed so far from passive satellite observations.

Having established that optically thin clouds significantly contribute to the total cloud cover, it is further interesting to investigate their brightness or average cloud reflectance. Climate models have been shown to exhibit intrinsic biases concerning low clouds, namely the often-called "too few, too bright" low cloud bias where models underestimate cloud cover while overestimating cloud brightness in the trades (Nam et al., 2012). Models also have been found to exhibit negative cloud-cover – cloud-reflectance relationships in the trades in the [CMIP5](#) analysis (Konsta et al., 2016), as well as in the recent [CMIP6](#) runs (personal communication Jean-Louis Dufresne). Observations however show a positive relationship that is also found in high-resolution [ASTER](#) observations for both cases, with and without optically thin clouds. Including optically thin clouds into the total cloud amount does not only enhance cloud cover, but also reduces the average cloud reflectance by 29 %. Thus, the "too few, too bright" bias stating the underestimation of cloud cover and overestimation of cloud reflectance might be even worse than assumed so far. One among many reasons could be the tuning of models based on conventional satellite cloud products that overestimate the cloud reflectance especially in the frequent low cloud cover situations.

4.3 IMPLICATIONS OF OPTICALLY THIN CLOUDS

Undetected optically thin clouds in the trades have the potential to greatly influence the clear-sky signal. Pristine clear-sky observations are crucial for aerosol retrievals, as well as [CRE](#) estimates. The trades have been shown to exhibit a positive cloud feedback due to a less negative [CRE](#) (Zelinka et al., 2020). However, observational constraints for small clouds are challenging to estimate based on coarse satellite data. I therefore estimate possible biases that might arise from clear-sky signals which are contaminated by optically thin clouds.

Mixing the reflectances from optically thin clouds into the clear-sky signal would lead to an overestimation of the clear-sky reflectance and consequently an underestimation of [CRE](#) which is defined as the difference in all-sky minus clear-sky radiative fluxes. In particular, from the [ASTER](#) analysis we estimate a bias of -32 %

that roughly translates to about -6 Wm^{-2} . The magnitude is comparable to the aerosol direct effect in the winter trades highlighting the importance of an improved representation of optically thin clouds in future studies.

Within the context of aerosol-cloud interactions a possible positive correlation between AOD and cloud cover is largely debated (Gryspeerdt, Quaas, and Bellouin, 2016; Loeb and Manalo-Smith, 2005; Quaas et al., 2020). The underlying principle is the so-called cloud lifetime effect where hydrophilic aerosols can serve as cloud condensation nuclei. More aerosols might therefore lead to a higher cloud droplet number concentration and reduced precipitation which increases the cloud lifetime (Albrecht, 1989). However, the positive correlation between optically thin clouds and the detected cloud cover described in the previous chapter 4.2 suggests that part of the proposed sensitivity of cloud cover to AOD might reflect a high bias in clear-sky estimates that is interpreted as high AOD.

Independent of the questionable cloud lifetime effect, aerosols might indeed increase the cloud droplet number concentration and the concurrent cloud brightness in the shortwave spectrum (Twomey effect: Twomey, 1959). Increasing cloud brightness potentially lifts the brightness of optically thin clouds over the detection threshold barrier of conventional cloud masking schemes. Thus, more aerosols and cloud brightening might indirectly lead to a higher detected cloud cover and unrealistically strong relationship between aerosols and cloud cover as it is found in previous studies. The strength of aerosol-cloud interactions is likely overstated from coarse-scale satellite-retrieved aerosol and cloud properties.

SUMMARY AND CONCLUSION

*People often say that I'm curious about too many things at once...
But can you really forbid a [woman or] man from harbouring a desire
to know and embrace everything that surrounds [her or] him?*

— Alexander von Humboldt

Within this thesis I exploit the potential of high-resolution satellite observations for investigating small and optically thin trade wind cumulus clouds. Due to their small horizontal and vertical extent and their frequent low optical thickness, trade wind clouds are partly unresolved in conventional datasets, that are used to study the response of clouds in a warmer climate. A significant spread in climate projections within the trades motivated the intensive study of those clouds and their interplay with the environment in this thesis, as well as within the recent field campaign EUREC⁴A. Here, I come back to the explicit questions that I posed in chapter 2 and 4 of this essay and provide answers to them.

5.1 RESULTS IN A NUTSHELL

What causes the spread in proposed scaling behaviours of trade cumulus cloud sizes? From studying an extensive set of [ASTER](#) images, a robust description of the cloud size distribution is proposed in the form of a double power law. The range of scaling behaviours stated in the literature is rooted in different fitting strategies and too few data samples. In agreement with a homogenized view on published values I can confirm that small clouds with diameters between 0.5 km and 1 km around the break in the scaling behaviour contribute most to the total cloud cover. Even large-eddy simulations with grid sizes at the hectometer scale struggle to represent clouds with sizes below 1.7 km. Climate models without a subgrid scheme for clouds might miss a significant amount of the cloud cover in the trades.

Which cloud-controlling factors and related physical mechanisms known for stratocumulus clouds or suggested from LES studies can be confirmed for trade cumulus clouds? Cloud-controlling factors relate cloud properties and their interplay with the environment in the current climate to the cloud properties that we expect in a warmer climate. Within the trades, the strength of the trade winds shows the strongest control on the clouds. Also, the wind-speed related Bowen ratio emerges as a potential new control factor that should be further investigated. The sea surface temperature and the stability within the lower troposphere show strong controls on the clouds from the [ASTER](#) dataset and, together with their expected







Increased cloud-controlling factor	Lower-tropospheric stability (LTS)	Sea-surface temperature (SST)	Surface wind speed	Bowen ratio
Change in cloud properties  initial state  perturbed state				
Physical mechanism	The trade wind inversion strengthens with increasing LTS, traps moisture, and leads to increased cloud cover	Higher SST increases moisture fluxes. A strong moisture gradient leads to a higher entrainment efficiency at the inversion and thus, to cloud thinning and lower cloud tops	Stronger winds increase the surface fluxes leading to an increased boundary layer depth, which promotes larger and deeper clouds	The Bowen ratio controls cloud base mass flux by setting the thermodynamic efficiency of the moist convective heat cycle
	(Wood and Bretherton, 2006)	(Bretherton and Blossy, 2014)	(Nuijens and Stevens, 2012)	(Sakradzija and Hohenegger, 2017)

Figure 5.1: Table showing the dominating cloud-controlling factors for trade cumulus cloud properties as derived from high-resolution [ASTER](#) observations. The table is a subset of an extended set of factors summarized in the respective table [A.14](#) in Appendix [A](#). A change in cloud properties and in particular cloud sizes and their top heights is sketched with an increase in the respective cloud-controlling factors.

change with warming, are thought to constrain cloud feedbacks in the trades. Based on a detailed view of several cloud properties, certain physical mechanisms relating cloud properties to cloud-controlling factors are favoured while others seem less likely as summarized in Fig. [5.1](#).

While it will be the tasks of the many studies emerging out of EUREC⁴A to further constrain cloud-controlling factors and cloud feedbacks, we already gained new insights on trade wind clouds from studying aircraft and satellite datasets. From comparing various active and passive remote sensing instruments on board of the [HALO](#) aircraft we learned that the lidar instrument is most sensitive to cloud droplets and is able to see optically thin clouds. While this proves common knowledge, new insights are gained for passive imagers and their general ability to detect not only the small, but also the optically thin clouds if suitable thresholds are chosen within their respective cloud masking schemes. The occurrence of optically thin clouds motivated the following questions:

How much of the trade cumulus clouds do we miss in conventional cloud masking schemes? Based on the EUREC⁴A [ASTER](#) dataset, 45 % of the total cloud cover is due to optically thin clouds that are undetected by conventional cloud masking schemes. In terms of their brightness, optically thin clouds reduce the average cloud reflectance by 29 %. While climate models are known to underestimate cloud cover and overestimate cloud brightness, the current results suggest that those biases may be worse than assumed so far and may translate to an uncertainty

in cloud feedbacks.

Do optically thin clouds matter? Yes, optically thin clouds matter. Undetected optically thin clouds can strongly bias the clear-sky measurements and thus, estimates of the radiative effect of clouds as well as our perception of aerosol-cloud interactions. A possible bias in cloud radiative effect is 32 % if optically thin clouds are fully mixed into the clear-sky signal. Within the aerosol-cloud-interaction context, the results on optically thin clouds indicate an overstatement of the impact of aerosols on cloud cover.

5.2 OUTLOOK

This thesis shows that investigating clouds from observations remains challenging. In fact, personally I think that the greatest challenge concerns the term *cloud* itself and how it is biased by our visual perception in the frequency range the human eye is sensitive to. Human observations are at the base of our knowledge on clouds and will remain important for scientists to "get a feel" for clouds and their environment, to develop ideas and concepts. Nevertheless, care should be taken when designing cloud detection algorithms which are typically constructed for a certain purpose leading to differing cloud cover estimates. Hence, they do not necessarily depict the relevant measures describing the influence of clouds on radiation, dynamics, or the climate system as a whole.

In chapter 4, I try to overcome the disadvantages of thresholding tests in conventional cloud masking schemes and constrain the cloud cover from the well-understood clear-sky signal. Although the model developed for this purpose is very specific and simple and therefore not universally applicable, it shows that clear-sky simulations are a presumably less biased way to describe clouds as a residual. The application of full radiative transfer models for simulating clear-sky observations globally should be further explored. Radiative transfer models are commonly used to retrieve aerosol information from cloud-free areas and it seems like a low-hanging fruit to use those existing tools and extract additional information on cloudy areas including the optically thin clouds.

The development of the clear-sky model approach in chapter 4 motivated the description of cloud-free and cloudy areas in terms of probabilities. Instead of a binary decision, every pixel reflectance can be attributed a probability for any defined flag, in the current case *clear*, *undetected optically thin cloud*, or *detected cloud*. Undetected and detected relates to a conventional cloud masking scheme based on thresholding tests. Even when working with thresholding tests, it is possible to exchange binary decisions on the pixel level with the probability of the input field (often more than one) to relate to a cloudy measurement. Exchanging cloud masks with arrays of "cloud probability" would enable a better combination

of cloud estimates from different sensors and retrieval techniques. If needed, such probabilistic cloud maps can be easily converted into a binary cloud mask by applying thresholds in probability state instead of instrument quantities as commonly used in detection algorithms.

One can extend the idea of cloud probabilities further to the physical quantities such as liquid water content or cloud droplet size that the probabilities are ideally based on. This framework might bring us back to the idea of a cloud atlas - an idea pursued by some people within the EUREC⁴A community. In the introduction to this thesis I mentioned the first efforts of constructing a cloud atlas purely based on human-made cloud observations in 1890. Instruments and retrieval techniques available nowadays enable us to go beyond a phenomenological view of clouds and create a cloud atlas that can store clouds' physical quantities within a multidimensional space and have the data readily accessible.

While such a cloud atlas may provide huge possibilities, it also presents the scientific community with challenges. A binary cloud mask is easier to understand and work with compared to extensive datasets with more accurate but also overwhelmingly rich content. It is therefore necessary to simultaneously develop user-friendly tools that not only motivate the usage of the data, but educate scientists on elegant ways of handling the data. One small and first step may be the development of the "How to EUREC⁴A" book described in chapter 3.2. It did not only prove to be a valuable tool during the creation of datasets by various instrument groups, but it also motivated scientists from within as well as outside the EUREC⁴A community to kick-start their own analysis of the data and contribute with their own knowledge. Such a community effort is most efficient in eliminating bugs and keeping a lively discussion of current and future challenges for the scientific field. It was a pleasure to contribute to those ongoing projects.

Part II

APPENDIX

THE DEPENDENCE OF SHALLOW CUMULUS MACROPHYSICAL PROPERTIES ON LARGE-SCALE METEOROLOGY AS OBSERVED IN ASTER IMAGERY

This chapter contains a paper which has been published in the *Journal of Geophysical Research: Atmospheres* as Mieslinger et al. (2019):

Mieslinger, T., Horváth, Á., Buehler, S. A., and Sakradzija, M. (2019). The dependence of shallow cumulus macrophysical properties on large-scale meteorology as observed in ASTER imagery. *Journal of Geophysical Research: Atmospheres*, 124, 11477– 11505. <https://doi.org/10.1029/2019JD030768>

CONTRIBUTIONS Within my PhD, I compiled the main statements of this paper including the detailed study of cloud size distributions and the various relations of cloud properties with cloud-controlling factors, as well as the interpretation of related physical mechanisms in light of the recent literature. I conducted all analysis, prepared figures and wrote the paper with major text contributions by my co-author Á. Horváth and helpful advices by all co-authors.

The dependence of shallow cumulus macrophysical properties on large-scale meteorology as observed in ASTER imagery

Theresa Mieslinger^{1,2}, Ákos Horváth¹, Stefan A. Buehler¹, Mirjana Sakradzija³

¹ *Universität Hamburg, Faculty of Mathematics, Informatics and Natural Sciences, Department of Earth Sciences, Meteorological Institute, Hamburg, Germany*

² *International Max Planck Research School on Earth System Modelling, Hamburg, Germany*

³ *Max Planck Institute for Meteorology, Hamburg, Germany*

KEY POINTS

- We investigate the sensitivity of shallow cumulus cloud fields to large-scale meteorology with high-resolution satellite imagery.
- We identify surface wind speed as the dominant cloud-controlling factor in our dataset.
- We confirm the robust representation of cloud size distributions by a double power-law.

ABSTRACT

This study identifies meteorological variables that control the macrophysical properties of shallow cumulus cloud fields over the tropical ocean. We use 1,158 high-resolution Advanced Spaceborn Thermal Reflection Radiometer (ASTER) images to derive properties of shallow cumuli, such as their size distribution, cloud-top heights, fractal dimensions, and spatial organization, as well as cloud amount. The large-scale meteorology is characterized by the lower-tropospheric stability, subsidence rate, sea surface temperature, total column water vapor, wind speed, wind shear, and Bowen ratio. The surface wind speed emerges as the most powerful control factor. With increasing wind speed the cloud amount and cloud-top heights

show a robust increase accompanied by a marked shift in the cloud size distribution towards larger clouds with smoother shapes. These results lend observational support to the deepening response of a wind-driven marine boundary layer as simulated by large-eddy models. The other control factors cause smaller changes in the cloud field properties. We find a robust increase in cloud amount with increasing stability and decreasing sea surface temperature respectively, which confirms a well-known behavior of marine stratocumulus also for shallow cumulus clouds. Due to the high resolution of cloud images we are able to study the lower end of the cloud size distribution and find a robust double power-law behavior with a scale break at 590 m. We find a variation in the shape of the cloud size distribution with Bowen ratio, qualitatively consistent with modeling results and suggesting the Bowen ratio as a new potential control factor on shallow cumulus clouds.

A.1 INTRODUCTION

We identify large-scale meteorological drivers of shallow cumulus macrophysical properties from an extensive high-resolution observational dataset. Previous literature demonstrates that data limitations impede the investigation of primary control factors on shallow cumulus or trade wind cumulus clouds within the tropical marine boundary layer, while at the same time such clouds play a crucial role in the Earth's radiative balance. Due to their high albedo and ubiquitous nature, they reflect a substantial amount of shortwave radiation and cool the Earth system. These low-level warm clouds have been identified as the main source of divergence in estimates of climate sensitivity, as their representation in global climate models, especially their coupling to the large-scale flow, is still problematic (Bony and Dufresne, 2005; Vial et al., 2018). Accurately modeling the sign and magnitude of low-cloud feedback in a warming climate does therefore require an understanding of how the large-scale meteorological conditions govern the micro- and macrophysical properties of shallow cumulus clouds.

Mean subsiding motion and the resulting enhanced stability largely identify the areas where low-level clouds are prevalent. Well established measures of environmental controls on low-level cloud fields are correspondingly the subsidence rate and the lower-tropospheric stability (LTS), which is the potential temperature difference between 700 hPa and the surface (Klein and Hartmann, 1993; Slingo, 1987). Wood and Bretherton (2006) show that LTS and variations thereof can be used to discriminate between stratocumulus and shallow cumulus cloud fields. Stratocumulus decks favor the cool sea surfaces of eastern boundary currents, which are associated with large LTS, a shallower boundary layer, a strong capping temperature inversion, and stronger subsidence. Shallow cumuli, on the other hand,

tend to form over warm surfaces deeper in the tropics, which are characterized by smaller LTS, a deeper boundary layer, a weaker inversion, and somewhat weaker subsidence. A threshold value of about 18.5 K can generally distinguish between the high-LTS stratocumulus and low-LTS shallow cumulus regimes (Klein and Hartmann, 1993; Medeiros and Stevens, 2011). These two basic cloud regimes are not sharply separated though, but instead are connected through transition regions where stratocumulus begins to break up with shallow cumuli developing underneath (Sandu and Stevens, 2011). To our knowledge there is no study yet that investigates the potential of LTS on controlling different cloud field states within the shallow cumulus cloud regime and that goes beyond the bulk cloudiness.

In addition to LTS, several other factors controlling low clouds were identified in both observational and large-eddy simulation (LES) modeling studies; for a recent review see Klein et al. (2018). For example, subsiding motion and sea surface temperature (SST) often covary such that cold SSTs enhance subsidence and atmospheric stability, both leading to an increase in low-level cloudiness (Qu et al., 2015). Similarly, increased free tropospheric humidity and increased horizontal cold air advection are both positively correlated with low-cloud amount (Myers and Norris, 2016; Norris and Iacobellis, 2005). We refer to the free troposphere as the layer above the planetary boundary or trade wind boundary layer which includes the well-mixed sub-cloud layer and the cloud layer. Concerning the influence of humidity, Stevens et al. (2018) point to the regulating role of water vapor and its distribution in the tropical lower troposphere on cloud patterns. Furthermore, prevailing surface easterly winds are a prominent feature of subtropical regions over ocean, which are often called the trades or trade wind region. A recent study around Barbados revealed a high influence of surface wind speed on cloud cover (Brueck, Nuijens, and Stevens, 2015), while some modeling studies even claim that surface winds are a major control to shallow cumulus cloud fields in the trades (Nuijens et al., 2015; Nuijens and Stevens, 2012).

The properties of shallow cumulus clouds are reduced to cloud amount as the sole measure of tropical low-level cloudiness in most previous studies. The strong emphasis on cloud amount stems from the fact that it is one of the most relevant parameters to radiative flux and thus cloud feedback calculations, which current climate models struggle to properly simulate. Other cloud field properties, such as the size distribution and spatial organization of clouds, have received less attention, although the cloud size distribution in particular is a key parameter used in parameterization schemes to calculate the mass flux and energy transported within individual clouds (Neggers, Jonker, and Siebesma, 2003). Cloud size distributions are commonly described by a power-law and its scaling parameter. The derivation of scaling parameters is handled rather inconsistently in the literature, leading to a wide range of published values. Furthermore, the spatial distribution or spatial clustering of clouds was found to influence the large-scale meteorological field. On the mesoscale, Tobin et al. (2013) and Tobin, Bony, and Roca (2012) observed

clustered cloud fields in drier atmosphere and with reduced cloud amount. The latter heavily affects the outgoing long-wave radiation and the vertical distribution of heating rates and may force large-scale circulation patterns. Whether such behavior extends down to small scale shallow-cumuli is an open question.

Previous literature demonstrates shortcomings in the investigation of the shallow cumulus regime due to coarse resolution and small observational datasets. Past investigations had to rely on airborne observations, land surface-imaging satellite sensors, or ground-based measurements due to the coarse spatial resolution of most meteorological satellite imagers. In fact, there is no high-resolution spaceborne imager dedicated to cloud observations in orbit today. Early studies used 30-60 m resolution Landsat images (Cahalan and Joseph, 1989; Gotoh and Fujii, 1998; Sengupta et al., 1990; Wielicki and Welch, 1986) or aerial photography (Benner and Curry, 1998; Plank, 1969) to estimate the cloud size distribution of shallow cumuli. Although these works clearly demonstrated the potential of high-resolution cloud imagery, they lacked statistical significance for only a handful of scenes were analyzed. The two most recent observational studies, on the other hand, principally relied upon ground-based radar, lidar, and ceilometer measurements at the Barbados Cloud Observatory (BCO), aided by Moderate-Resolution Imaging Spectroradiometer (MODIS) low-level cloud cover estimates derived from 1 km resolution pixel data (Brueck, Nuijens, and Stevens, 2015; Nuijens et al., 2015).

By far the most comprehensive and statistically robust satellite study of shallow cumulus is that of Zhao and Di Girolamo (2007), which analyzed 152 Advanced Spaceborne Thermal Emission Reflection Radiometer (ASTER) scenes collected west from the Caribbean islands during the Rain in Cumulus over the Ocean (RICO) campaign. From the 15 m resolution ASTER images, they derived statistics for the macrophysical properties of shallow cumulus cloud fields, including cloud fraction, cloud size, fractal dimension, cloud top height, and cloud spatial horizontal distribution. However, this study did not find any relationship between the large-scale meteorology and any of the estimated cloud macrophysical properties. The authors hypothesized this was due to the inability of their forecast data to capture the large-scale meteorological conditions during RICO. It might also have been the case that even Zhao and Di Girolamo (2007)'s extended dataset was too small to reveal dependencies on cloud-controlling parameters. Regardless, it bolsters the call made by the latest review of Klein et al. (2018) for further observational studies of shallow cumulus clouds.

The goal of our study is to take advantage of the public availability of the global ASTER data archive, expand upon the work of Zhao and Di Girolamo (2007), and identify the primary control factors of shallow cumulus cloud fields. We analyze 1,158 trade wind cumulus scenes drawn from the western Atlantic and the central and eastern Pacific, which constitute a dataset about an order of magnitude larger than in any earlier work. We investigate the amount, size distribution, fractal dimension, top height, and spatial organization of shallow cumulus clouds as a

function of large-scale meteorology characterized by ERA-Interim reanalysis. The considered cloud-controlling factors include LTS, subsidence rate, total column water vapor (TCWV), SST, surface wind speed, wind shear, and Bowen ratio. The Bowen ratio is the ratio of the surface sensible heat flux to the latent heat flux and has been proposed by a recent LES study of Sakradzija and Hohenegger (2017) to control the distribution of shallow cumulus cloud base mass flux and thus cloud size distribution.

The paper is organized as follows. Section A.2 describes the ASTER images and reanalysis dataset, the cloud masking algorithm, and the derivation of macro-physical cloud field properties. Section A.3 then shows overview statistics of these cloud field properties, including information on the representation of cloud size distributions. Here, we also show that the considerable scatter in previously reported scaling parameters of power-law cloud size distributions is to a large degree the result of inconsistent fitting and data binning strategies. Section A.4 presents the variation in observed cloud field properties with large-scale meteorological parameters with a focus on the dominant control variable surface wind speed. Finally, Section A.5 summarizes our results.

A.2 DATA AND METHODS

A.2.1 ASTER Imagery

ASTER flies aboard Terra, a polar-orbiting satellite in a sun-synchronous orbit with an equator crossing time of 10:30 local solar time. ASTER consists of one nadir and one backward-pointing camera. The nadir camera, whose imagery is used exclusively in this study, has three separate radiometers. The visible and near-infrared (VNIR) sensor covers the range from 0.53 - 0.86 μm in three bands with 15 m spatial resolution. The radiometer in the shortwave infrared (SWIR) range consists of six bands in the range of 1.60 - 2.43 μm at 30 m resolution, and the thermal infrared (TIR) radiometer comprises five bands covering 8.125 - 11.65 μm with 90 m spatial resolution (M. Abrams and Ramachandran, 2002; Yamaguchi et al., 1998). ASTER data are available in 60 x 60 km^2 scenes, each corresponding to 9 seconds of observation time.

The dataset is limited by the opportunistic nature of data acquisition over the ocean. ASTER was designed for land surface studies and thus prioritizes cloud-free and land observations. Nevertheless, it has also acquired a large number of oceanic cloud scenes, often in support of atmospheric field campaigns such as RICO. It should be noted, however, that ASTER's sampling of clouds is rather irregular as a result. Starting in May 2007 the SWIR detector suffered temperature problems,

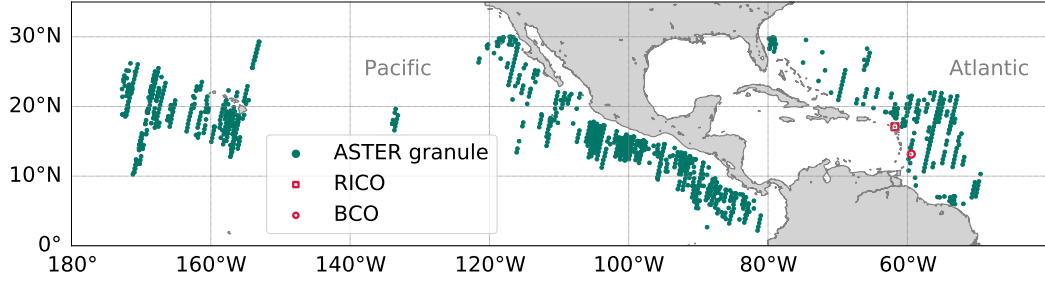


Figure A.1: The geographical location of the ASTER images of shallow cumulus cloud fields comprising our dataset collected between 2000 and 2007. The 1,158 images are depicted by green circles, 325 of which are around Hawaii in the central Pacific, 613 in the eastern Pacific, and 220 in the western Atlantic. The location of the RICO field campaign and that of the Barbados Cloud Observatory (BCO) are indicated in red shapes.

leading to image striping and saturation effects. Therefore, we only consider data from 2000 to mid 2007 as the cloud masking algorithm described in section A.2.2 relies on a SWIR band.

We filter the available images for pure shallow cumulus cloud fields in the tropics. The study area is limited to the northern hemisphere from 0 - 30°N, zonally covering the central and eastern Pacific as well as the western Atlantic. Cloudy scenes dominated by stratocumulus, affected by sun glint, or contaminated by cirrus are eliminated. The latter turned out to be a major constraint, because many shallow cumulus scenes also show high-level cirrus clouds. The presence of cirrus clouds likely indicates additional dynamical influences to the meteorological state that would complicate our analysis. Such scenes are therefore excluded. Thin cirrus is often transparent in the visible bands, but can easily be detected in ASTER's thermal infrared bands from their cold cloud-top temperatures. We find that 47 of the 152 scenes of Zhao and Di Girolamo (2007) have some cirrus contamination, although this did not have a major effect on their results as the authors relied on visually-derived cloud masks based on a visible channel only. Our final dataset, including the 105 cirrus-free scenes from Zhao and Di Girolamo (2007), consists of 1,158 carefully selected and visually checked ASTER scenes of tropical shallow cumulus, the geographic locations of which are plotted in Figure A.1.

A.2.2 ASTER Cloud Mask and Cloud Object Labeling

ASTER does not have operational cloud products, thus a cloud mask has to be derived independently. Previous high-resolution cloud studies were based on visually-derived cloud masks using manually-tuned thresholds, which are unfeasible

for analyzing a large number of images (Benner and Curry, 1998; Cahalan and Joseph, 1989; Zhao and Di Girolamo, 2007).

Therefore, we implement the automated ASTER cloud masking technique of Werner et al. (2016) with the addition of a sun glint filter. This algorithm employs five threshold tests, similar to the MODIS cloud detection scheme, and classifies each 15 m pixel as *clear*, *probably clear*, *probably cloudy*, and *cloudy*. Four tests are based on reflectivity thresholds in the VNIR and SWIR range and are designed to distinguish between bright clouds and the dark ocean. Under strong sun glint or broken cloud conditions, an additional test based on band 14 (11.65 μm) applies to correct warm ocean pixels that are labeled cloudy after the first four tests. In such cases, however, the effective resolution of the cloud mask is noticeably reduced to that of the coarser (90 m resolution) thermal channel. To avoid the degradation of the cloud mask, all images with possible sun glint are excluded from our dataset. First, the glint angle is computed for each pixel from the sensor-sun geometry information stored in L1B file metadata (Yang et al., 2015). Then pixels with a glint angle below a threshold are flagged as potentially sun glint contaminated. From visual inspection we find that a threshold value of 25° efficiently eliminates glint-affected and thus reduced-resolution cloud masks. Finally, the *clear* and *probably clear*, as well as the *cloudy* and *probably cloudy* classes are merged to create a binary (*clear*, *cloudy*) mask, from which all subsequent cloud field properties are derived.

Figure A.2 shows a typical ASTER shallow cumulus scene on the 9th of September 2004 over the Atlantic ocean. Reflectances from band 3 (0.86 μm , nadir) in panel a) exemplify the information content from the visible bands used in reflectivity thresholding tests. Panel b) shows a false-color image of brightness temperatures from ASTER's thermal band 14 (11.65 μm). High and cold cloud tops are clearly visible in yellowish colors. Three further channels contribute information to the final cloud mask shown in panel c). We evaluate the performance of the automated cloud masking algorithm of Werner et al. (2016) against the manually constructed reference cloud masks described in Zhao and Di Girolamo (2007). From a direct comparison of 105 cirrus-free cloud images we find that cloud field properties such as cloud fraction, cloud size distribution, and fractal dimension agree well with the work of Zhao and Di Girolamo (2007), confirming that the automated cloud masking scheme adequately detects marine shallow cumulus clouds.

Based on the binary cloud mask, individual cloud objects are defined with the 4-connectivity rule, which groups neighboring cloudy pixels sharing an edge into the same cloud, but treats cloudy pixels sharing only a vertex as separate clouds. Single-pixel clouds are found to mostly reflect instrument noise and are therefore excluded from further calculations. The total number of clouds in the selected 1,158 ASTER images is 5,171,808.

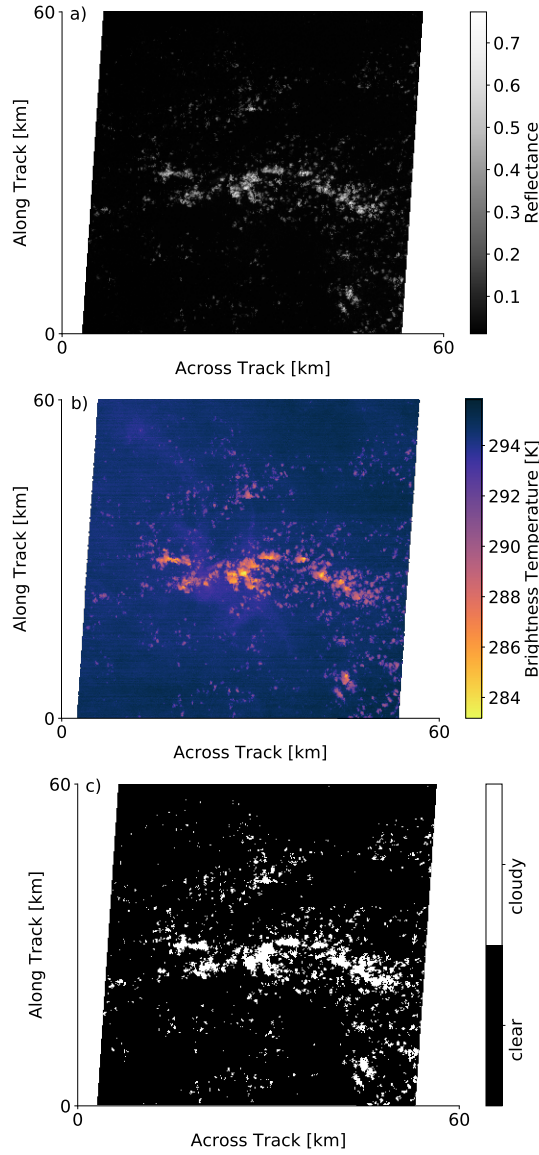


Figure A.2: ASTER scene recorded on the 9th of September 2004 at 14:12:47 UTC showing a) reflectances from the VNIR band 3 ($0.86\ \mu\text{m}$, nadir) in grey-scale, b) a false-color image of brightness temperatures from ASTER's thermal band 14 ($11.65\ \mu\text{m}$), and c) the cloud mask derived following Werner et al. (2016).

A.2.3 Fractal Dimension

The geometric irregularity of shallow cumulus clouds can have important radiative impacts, as it has been found to significantly affect domain-averaged solar fluxes and atmospheric heating rate profiles (Hinkelman et al., 2007). The general com-

plexity of cloud shapes can be characterized by the scaling relationship between cloud perimeter P and cloud area A (Lovejoy, 1982):

$$P \propto A^{\frac{d}{2}} \quad (\text{A.1})$$

where the exponent d is the fractal dimension. The fractal dimension is a statistical descriptor of inherent scaling, which does not uniquely define shapes. However, for regular shapes such as a circle, d is unity, while d would approach the value of two for increasingly fissured clouds with fractal perimeters and equation (A.1) transforms to $P \propto A$ accordingly.

We calculate the cloud area A from the sum of all pixels belonging to the same cloud entity and multiply it by the pixel area defined by the cloud mask resolution ($15 \times 15 \text{ m}^2$). The cloud perimeter P can be defined in different ways, however, different definitions still produce a similar scaling relation (Cahalan and Joseph, 1989). In our study, P was calculated as the summed length of boundary line segments connecting the centers of cloud edge pixels. The fractal dimension d is then approximated from a linear least-squares fit to a doubly logarithmic scatterplot of P versus A . For small clouds the slope is sensitive to the perimeter algorithm and the pixel shape. Because the pixel shape is regular, the derived fractal dimension tends to become smaller when more small clouds are included in the analysis and vice versa. However, we did not detect such artefacts in our analysis at small cloud sizes. In fact, we find the fractal dimension decreasing even when large cloud sizes are more abundant (see section A.4).

A.2.4 Cloud Size Distribution

Shallow cumulus clouds exhibit sizes ranging over several orders of magnitude. The vast majority of clouds are small and the cloud size distribution tails off towards less frequent large clouds. As a result, empirical cloud size data are most commonly assumed to follow a power-law distribution, both in observational and modeling studies. Whether this assumption is justified in a strict mathematical sense or the data are better described by other statistical distributions (log-normal, exponential, stretched exponential) is an important topic in and of itself, which, however, is beyond the scope of this work. For an excellent review on the subject, the reader is referred to Clauset, Shalizi, and Newman (2009). Suffice it to say, one can hardly ever be certain that an observed quantity is truly drawn from a power-law distribution due to the insufficient sampling of the distribution tail, which represents large but rare events. For consistency and comparability with previous studies, we assume a power-law distribution here, but show that the most common method to estimate the scaling parameter, a least-squares linear regression

on data represented in a log-log plot, gives predictably different results depending on histogram binning scheme and the choice of cloud size measure.

If a quantity, such as the size of a cloud D , obeys a power-law, it is drawn from a probability distribution:

$$n(D) \propto D^b \quad (\text{A.2})$$

where the (negative) exponent b is the *slope* or *scaling parameter*. The scaling parameter typically lies in the range of $-3 < b < -2$ for natural phenomena.

Power-laws were extensively used in the literature to characterize cloud size distributions. While early studies on shallow cumulus clouds found an exponential decrease in cloud number with increasing cloud size (Plank, 1969; Wielicki and Welch, 1986), or reported a lognormal behaviour (López, 1977), more recent studies fit power-laws to cloud size distributions (Benner and Curry, 1998; Cahalan and Joseph, 1989; Heus and Seifert, 2013; Koren et al., 2008; Neggers, Jonker, and Siebesma, 2003; Zhao and Di Girolamo, 2007). The scaling parameter is a characteristic measure of cloud size distributions as it indicates the cloud sizes that contribute most to the cloud fraction. For example, a steep slope means the preponderance of small clouds. In the following, we explain in more detail the derivation of the scaling parameter for a power-law and reveal some inconsistencies in the application of power-law fits within the literature with the aim to make the various published numbers comparable.

The scaling parameter can be derived by taking the logarithm of both sides of equation A.2 yielding the linear form

$$\log(n(D)) = \text{const.} + b \cdot \log(D). \quad (\text{A.3})$$

In practice, the probability density function $n(D)$ is estimated by constructing a histogram of the data. Then b is estimated as the slope of the least-squares linear regression between the logarithm of the bin counts $\log n(D)$ and that of the bin center values $\log D$. For cloud size distributions, one can either use a measure of length D , such as cloud area-equivalent diameter or the square root of the area \sqrt{A} , or alternatively the area A . Cloud area-equivalent diameter is a common length scale measure of cloud size, which we also use in this study. It is calculated from the cloud area by assuming a perfectly circular cloud.

The cloud size histogram can be constructed using bins of constant width, what we call *linear binning*, or bins of exponentially increasing width, referred to as

logarithmic binning, where bins have the same width in logarithmic space. Note, however, that switching from D to A as the cloud size measure and switching from linear to logarithmic histogram binning both amount to a change of variable of the probability density function. Applying the well-known change-of-variable technique to transform the probability density function, it can be shown that if D follows a power-law with exponent b as in equation (A.2), then

$$n(\log(D)) \propto D^{b+1}, \quad (\text{A.4})$$

$$n(A) \propto A^{\frac{b-1}{2}}, \quad (\text{A.5})$$

$$n(\log(A)) \propto A^{\frac{b+1}{2}}. \quad (\text{A.6})$$

Using \sqrt{A} instead of D as length measure, on the other hand, yields a power-law with the same exponent b , because $\sqrt{A} \propto D$. We provide an explicit derivation of $n(\log D)$, $n(A)$ and $n(\log(A))$ in A.6.1.

When displaying empirical data on a logarithmic scale it is most appropriate to use bins that are equidistant in logarithmic space. Although many studies in the past used equal linear bin increments, we emphasize that displaying the data in such a way is misleading because the area below the curve does not represent the integral over the probability density as the reader might intuitively assume. Instead, the derivative $dD/d(\log D)$ needs to be applied to $n(D)$ for consistency (see equation A.11). Using logarithmic binning is not only more adequate for the problem, it also allows the full range of cloud sizes to be taken into account for the derivation of the scaling parameter. In comparison, studies using linear bin increments, such as Benner and Curry (1998) and Zhao and Di Girolamo (2007), only included cloud sizes up to 7 km or less to prevent the noisy upper part of the cloud size distribution from having a strong weight in the fitting procedure. From a sensitivity study (not shown) we conclude that the cloud size distribution changes strongly with bin size and fitted range of values when using linear binning, while the shape of the size distribution is more robust for logarithmic binning, confirming our argument in favor of logarithmic binning.

A.2.5 Cloud Spatial Distribution

In Figure A.3 we show example ASTER images for different cloud spatial distributions: a) randomly or regularly distributed clouds and b) a clustered cloud field

with arcs, cloud-free areas, and larger cloud objects. Assuming that in clustered shallow cumulus cloud fields small clouds merge and form larger cloud objects with cloud-free areas in between, the visual classification into unclustered and clustered states can be quantified by a combination of the number of clouds in a given domain and the distances between cloud objects. These two measures are combined differently in the two cluster indices, the Simple Convective Aggregation Index (SCAI) and the organization index I_{org} , which are commonly applied in cloud field studies.

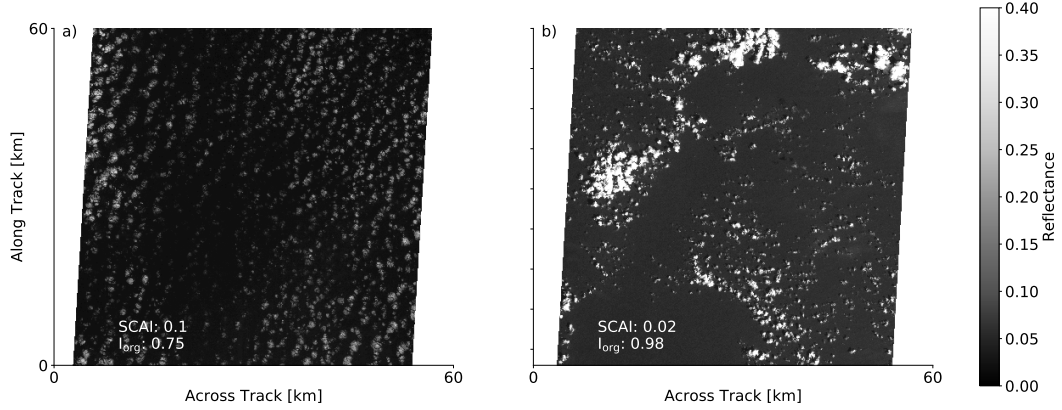


Figure A.3: Example ASTER scenes showing reflectances from the VNIR band 3 ($0.86\ \mu\text{m}$, nadir): a) for an unclustered cloud field and b) for a clustered cloud field. The corresponding SCAI and I_{org} cluster indices are stated.

A.2.5.1 Simple Convective Aggregation Index

The Simple Convective Aggregation Index (SCAI), was originally introduced by Tobin, Bony, and Roca (2012) for the description of deep convective clusters. It is a combination of two parameters, the number of clouds and the average distance between them, both of which are relevant in describing the clustering of points in an ensemble. For example, fewer clouds or shorter distances correspond to a higher degree of aggregation alike. The SCAI is calculated as the product of (i) the total number of clouds N , normalized by the maximum possible number N_{max} within a given domain and (ii) a measure of the distance between the clouds l , normalized by the characteristic length scale of the domain L . That way the aggregation state is normalized by the maximum potential disaggregation.

The value of N_{max} is determined by the domain size, the pixel resolution, and the cloud labeling scheme. With the applied 4-connectivity rule, N_{max} is half the number of pixels in a band 3N ASTER image. The characteristic cloud distance l is the geometric mean of all distances l_i between all possible cloud pairs, while L is set to the length of the diagonal of the $60\text{ km} \times 60\text{ km}$ ASTER domain. The

SCAI index is then calculated for each ASTER scene, expressed in per thousand, according to the following equation:

$$\text{SCAI} = \frac{N}{N_{\max}} \frac{l}{L} \cdot 1000 \quad (\text{A.7})$$

where $l = \sqrt[n]{\prod_{i=1}^n l_i}$ and $n = N \cdot \frac{N-1}{2}$ is the number of cloud pairs.

One consequence of this definition is that SCAI can increase with N and independently also with l . However, these parameters are correlated and cannot vary completely independently in a fixed-size domain. A larger number of clouds in an ASTER image would alone lead to a higher SCAI, but SCAI might remain unchanged or even decrease due to a simultaneously decreasing distance between the clouds. However, Tobin, Bony, and Roca (2012) show that the value of N is dominating the value of SCAI. Similarly, we find N and SCAI highly correlated in our dataset (Pearson correlation coefficient $r = 0.97$). Thus, low SCAI values can be related to aggregated cloud fields and high SCAI values to disaggregated situations.

A caveat to note is that the general magnitude of SCAI strongly depends on domain and pixel size, which makes the intercomparison of values derived from imagery of differing resolutions problematic. For example, the SCAI derived by Tobin et al. (2012) for $10^\circ \times 10^\circ$ domains using 50 km resolution brightness temperature data varies from 0 to 30, while in our ASTER dataset the SCAI range is two orders of magnitude smaller. We therefore focus on relative changes in SCAI in section A.4 without a direct interpretation of its absolute value.

A.2.5.2 Organization Index I_{org}

The second index used in our study is the organization index I_{org} , first introduced by Weger et al. (1992) and revisited by Tompkins and Semie (2017), which classifies a cloud field as regular, random, or clustered based on nearest neighbor (NN) distance statistics. If NN distances are on average smaller than expected from a random distribution, the cloud field is considered clustered, otherwise it is deemed regular. Unlike the SCAI, the I_{org} is unambiguous to interpret due to the way it is constructed and can be compared among different sensors as it always ranges from zero to one. If shallow convection is randomly distributed and hence can be described by a Poisson point process, then the cumulative density function of

nearest neighbor distances (NNCDF) exhibits a Weibull distribution of the following form:

$$\text{NNCDF} = 1 - \exp(-\lambda \pi l_n^2) \quad (\text{A.8})$$

where λ is the average sample number per unit area and l_n is the single nearest neighbor distances. In Figure A.4e the theoretical Poisson NNCDF is plotted against the actual observed NNCDF. The I_{org} is the integral of the resulting curve (brown line). If the observed distribution of clouds is random, the curve will lie on the diagonal and $I_{\text{org}} = 0.5$. When the paired NNCDF curve is above the diagonal and $I_{\text{org}} > 0.5$, the cloud field is clustered. In contrast, when the curve is below the diagonal, the I_{org} is smaller than 0.5 and the cloud field has regular or random organization.

A.2.6 Cloud Top Height

Cloud-top height (CTH) was derived at 90 m resolution from band 14 infrared window brightness temperatures, using the constant lapse rate method implemented in MODIS Collection 6 for marine stratocumulus under low-level inversion (Baum et al., 2012). The CTH is calculated from the difference in the brightness temperatures of cloudy and clear pixels observed at 11 μm and divided by the season- and latitude-dependent apparent lapse rate taken from a lookup table published in Baum et al. (2012). Band 14 at 11 μm is best suited for the retrieval because the water vapor absorption is low. Partial cloud cover can introduce a height bias as the assumed cloud emissivity of $\epsilon = 1$ is a valid approximation only for fully cloudy pixels. To minimize such biases we only derive CTH values for those 90 m pixels that are labeled fully cloudy by the 15 m resolution cloud mask. Similarly, a 90 m pixel was only assumed clear if all its 15 m subpixels were labeled clear.

A.2.7 ERA-Interim Reanalysis and MODIS data

The large-scale meteorology is characterized on a per scene basis mostly by ERA-Interim reanalysis data, at a horizontal resolution of 0.75° or about 80 km (Berrisford et al., 2011; Dee et al., 2011). Meteorological variables from ERA-Interim are available every 6 hours, leading to a maximum time difference of 3 hours relative to the ASTER observations. We use the following single-level parameters: sea surface temperature (SST), surface wind speed at 10 m height, vertical velocity at the 700 hPa pressure level, as well as the Bowen ratio calculated from surface moisture and heat fluxes. The lower-tropospheric stability (LTS) and bulk wind shear in the

boundary layer are derived from potential temperature and wind data between 1000 hPa and 700 hPa.

Scene-average total column water vapor (TCWV) is determined from ERA-Interim data and also from 5 km resolution MODIS-Terra thermal infrared retrievals (Collection 6 MOD05 product), which have perfect spatial and temporal coincidence with the ASTER scene. The thermal infrared retrieval is favored here over the near-infrared retrieval product, because the latter does not provide values for thin and broken clouds (King et al., 2003). TCWV values from ERA-Interim and MODIS retrievals are found to be in very good overall agreement, thus, we only show results for the MODIS retrievals.

A.2.8 Analysis Method

The sensitivity of low clouds to large-scale meteorological fields is usually investigated by multiple linear regression (MLR) between a time series of detrended anomalies of cloud fraction (predictand) and that of selected meteorological parameters (predictors). Applying MLR to our dataset would face various challenges though. First, ASTER's temporal sampling of clouds is highly irregular and episodic, preventing the creation of a continuous time series. Second, while MLR is well-suited to model the variations in a simple quantity such as cloud fraction, its applicability is less obvious when analyzing the subtler properties of the cloud size distribution, such as power-law exponent, scale break size, and spatial organization, which is the main focus of our paper. This is especially so, because the cloud size distribution cannot be accurately determined from a single scene. A number of scenes have to be aggregated to obtain reasonable estimates of distribution parameters, which unavoidably causes some convolution of the underlying meteorological parameters. Third, the minimum required sample size for MLR, which is a strong function of the squared multiple correlation coefficient, the desired accuracy of the prediction model, and the number of predictor variables, can easily exceed the size of our current ASTER dataset (Knofczynski and Mundfrom, 2008).

These limitations led us to adopt a simple approach, which characterizes the average cloud field properties as a function of a single binned meteorological control parameter at a time. The data subsets in each bin are chosen such that they include a minimum amount of images, but not necessarily the same amount. Choosing the subsets strictly such that an equal amount of values is included does not change our results in a qualitative way. This approach cannot account for the interdependency between the various control parameters and hence the derived sensitivities are likely biased. Nevertheless, the dominant effect of a given meteorological parameter can still be teased out, at least in a qualitative sense. As we show in the following, well-established stratocumulus-meteorology relationships, for example the increase

in cloud fraction with increasing LTS and decreasing SST, are also reproduced in our shallow cumulus data, which lends confidence in the results.

A.3 STATISTICAL OVERVIEW OF CLOUD FIELD PROPERTIES

A.3.1 Cloud Fraction, Cloud Top Height, Cloud Spatial Distribution, and Fractal Dimension

Based on the introduced cloud mask, the cloud amount in individual ASTER images ranges from 0 to about 60 % with an average of 8.7 %. The histogram and cumulative histogram of cloud fraction are shown in Figure A.4a. Small values are dominating with a histogram mode between 1.5 - 4.5 % and about 90 % of the images have a cloud fraction less than 20 %. Although not by design, our average cloud fraction agrees very well with the average cloud fraction of 8.6 % from Zhao and Di Girolamo (2007), indicating that the two datasets sample similar scenes of shallow cumuli.

Earlier studies report similarly low cloud fractions, one of the closest being a study by Benner and Curry (1998) that reports an average cloud fraction of 9 %. Observational studies reporting higher cloud fraction for shallow cumulus cloud fields often include cases at the transition to stratocumulus decks which dominate the eastern coasts of the continents or deeper convective clouds in the proximity of the ITCZ (Brueck, Nuijens, and Stevens, 2015; Cahalan and Joseph, 1989). The calculated average cloud fraction is also far lower compared to ground-based measurements at the Barbados Cloud Observatory (BCO), which can be viewed as a reference site for the trades. Nuijens et al. (2014) report an average cloud fraction of 30 % from ceilometer measurements, about two thirds of which are contributed by low-level clouds at the height of the Lifting Condensation Level (LCL). However, the ASTER images in our dataset do not include stratiform cloud layers and large cloud systems, which are present at the BCO at certain times. Therefore, the observed low-cloud fraction from ASTER images is reasonable as only shallow cumulus clouds under suppressed conditions are included. The BCO measurements show that our ASTER scenes are not representative of the climatology of the whole trade wind region, but rather correspond to a conditionally-sampled (e.g. cirrus-free) subset.

Scene-average CTHs are found to be mostly below 3 km with a broad peak in the frequency distribution below the average CTH of 1.3 km (see Figure A.4b). The studies of Zhao and Di Girolamo (2007) and Genkova et al. (2007) derived CTH values from ASTER imagery during the RICO campaign and found a bimodal frequency distribution with a primary peak at 0.9 km and a much smaller secondary

peak at 1.5 km. Compared to such a double peak, we find one broad peak in a similar height level, which might be due to retrieval errors in the different CTH calculations mentioned. In general, several factors add uncertainty to the CTH retrieval. Zhao and Di Girolamo (2007) derive a high bias of about 200 m due to possible water vapor absorption above the cloud tops. On the other hand, Genkova et al. (2007) show that the ASTER infrared-window retrieval exhibits a low height-bias of about 250 m on average compared to the more accurate stereo height retrieval, although the difference might have been caused by inadequate cloud motion correction in the stereo retrievals. In broken low-level cloud scenes, Greenwald et al. (2018) found a 450 m low bias in MODIS Collection 6 CTHs compared to Cloud-Aerosol Lidar with Orthogonal Polarization (CALIOP) layer top heights, which was attributed to the influence of the warm ocean surface on 1 km MODIS brightness temperatures in partly cloudy pixels. This potential warm surface effect, however, is likely to be much smaller in the 90 m ASTER brightness temperatures. Based on the above, we estimate an overall minimum uncertainty of 300 m in our instantaneous pixel-level ASTER CTHs.

Analyzing the clustering indices SCAI and I_{org} , we find that both indices vary in a narrow range, between 0.0 and 0.6 with a mean of 0.1 for SCAI and between 0.7 and 1.0 with a mean of 0.9 for I_{org} (see Figure A.4c and A.4d). Both distributions are skewed towards aggregated or clustered states, SCAI showing a positive skewness and I_{org} showing a negative skewness. The quantitative interpretation of SCAI is generally very difficult. For reference, one-pixel clouds distributed in a checkerboard pattern would correspond to $\text{SCAI} = 0.25$. Therefore, most of the observed cloud fields in ASTER images are more clustered than such a checkerboard pattern. The I_{org} on the other hand is a well-defined measure, which however classifies all cloud fields to be highly clustered. The narrow value range for both indices denotes a possible limited information content. In section 4 we therefore give only conservative interpretations of the changes in SCAI and I_{org} with meteorological variables.

We derive an overall fractal dimension of $d = 1.19$ from the full dataset. The relatively small value implies that trade wind cumuli detected in our ASTER dataset are rather compact and have smoother shapes compared to former studies (see Table A.1). The fractal dimension derived in the present study significantly differs from the percolation theory value of $d = 1.33$. Percolation can be viewed as a purely geometric null model for spatial clustering and also the related statistical properties, such as cloud sizes and their fractal dimension. A deviation from the percolation value indicates important physical or dynamical influences on the area-perimeter relation beyond pure geometric constraints (Peters, Neelin, and Nesbitt, 2009).

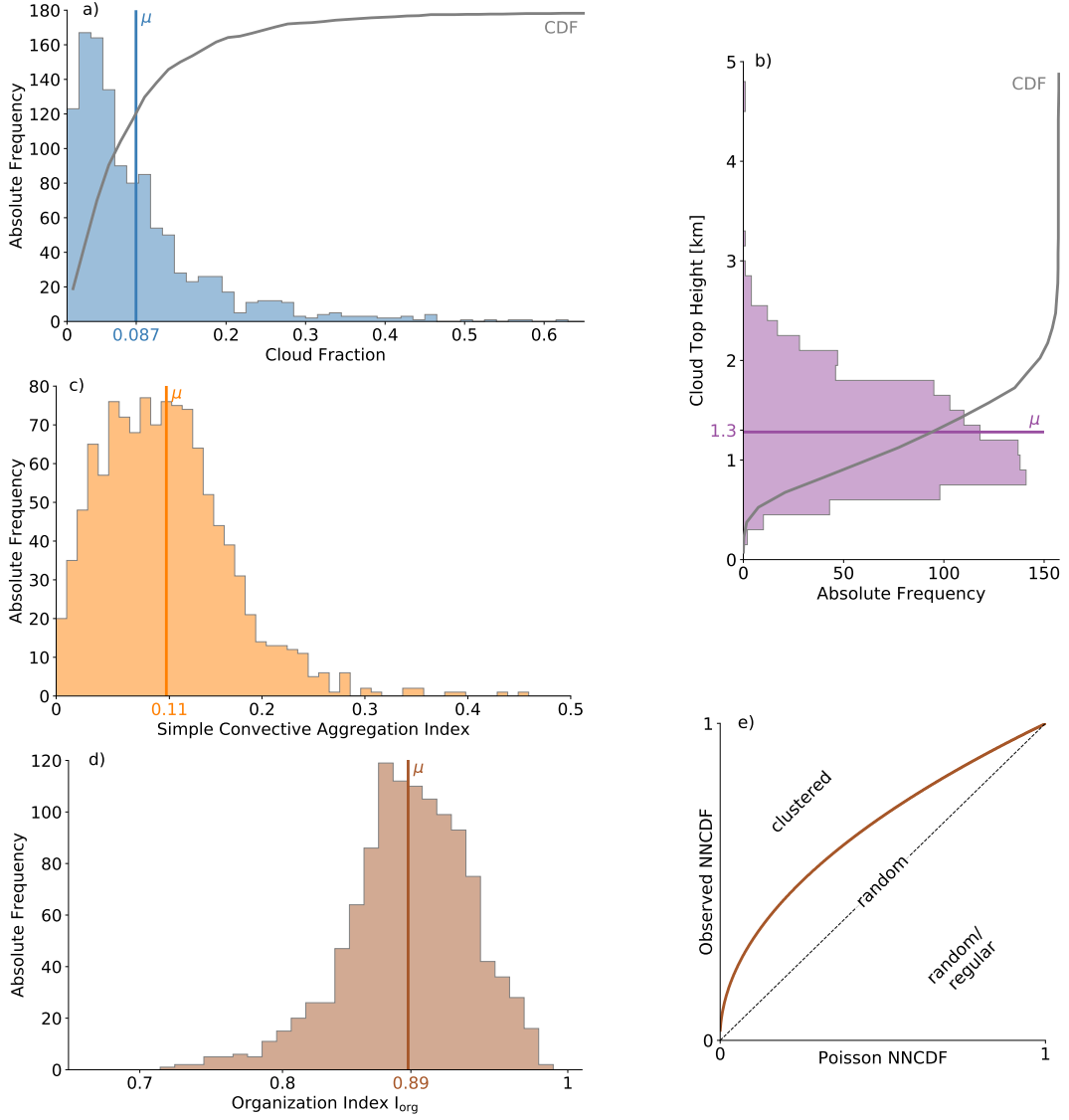


Figure A.4: Macrophysical properties of shallow cumulus cloud fields observed in 1,158 ASTER images. Panel a) shows the frequency of cloud fraction and panel b) the vertical distribution of scene-average cloud-top heights. μ gives the distribution average, while the grey line displays the cumulative density function (CDF). The clustering of clouds is shown in panel c) and d) in terms of the Simple Convective Aggregation Index and organization index I_{org} . The sketch in panel e) illustrates the derivation of I_{org} .

A.3.2 A Critical View of the Power-Law Fitting of Cloud Size Distributions

A.3.2.1 ASTER Cloud Size Distribution

In Figure A.5a the normalized cloud size distribution of all clouds detected in the ASTER dataset is displayed in terms of the cloud area-equivalent diameter in black steps showing $n(\log(D))$ (*logarithmic binning*) and in grey steps showing the deceptive $n(D)$ (*linear binning*). The distribution follows two straight lines, which can be represented by a double power-law with slopes for the small and the large cloud sizes respectively. The threshold cloud size, the so-called scale break size D_c , is defined such that the two least-squares fits result in the smallest combined error, that is the sum of the squared residuals of both fits. In the present study, a separation at $D_c = 590$ m in the size distribution is found with the corresponding slopes of $b_{\log,1} = -0.68$ for $D < D_c$ and $b_{\log,2} = -2.12$ for $D > D_c$. For consistency with previous literature, we also derive the scaling parameter for a single power-law, leading to $b_{\log} = -1.55$. For clarity, we explicitly label the scaling parameter as b_{\log} , which is equivalent to $b_{\log} = b_{\ln} + 1$ according to equation A.4.

Figure A.5b shows the cloud area A distribution for logarithmic (black) and linear binning (grey). In the linear case a fit is only performed up to $A = 38 \text{ km}^2$, which corresponds to $D = 7 \text{ km}$. The steps and linear regression fit for $n(\log(A))$ mimic the fit for $n(\log(D))$ as there is a factor 2 difference between the exponents, but the displayed range of A also covers double the orders of magnitude compared to the range of D values.

A.3.2.2 On the Scale Break Size

We find a robust scale break in the cloud size distribution at $D_c = 590$ m, similar to many past studies on shallow cumulus clouds that also apply a double power-law. However, a physical interpretation of the scale break is by no means trivial and potential mechanisms controlling the scale break have been widely discussed. Peters, Neelin, and Nesbitt (2009) find that cluster properties, such as the size distribution, change with column water vapor in mesoscale convective systems. The authors hypothesize that former studies find different functional forms of the size distribution because they mix several atmospheric states characterized by differing water vapor contents. Based on percolation theory they show that for certain column water vapor values the size distribution exhibits a scale-free behavior without a break. A close match of the observed distribution slope with that from percolation theory would imply that the observed cloud fields are rich in scales. However, if simple percolation were the dominating factor, it would also imply that little could be learned from statistical parameters describing cloud fields, because such parameters are mainly the result of geometric constraints rather than

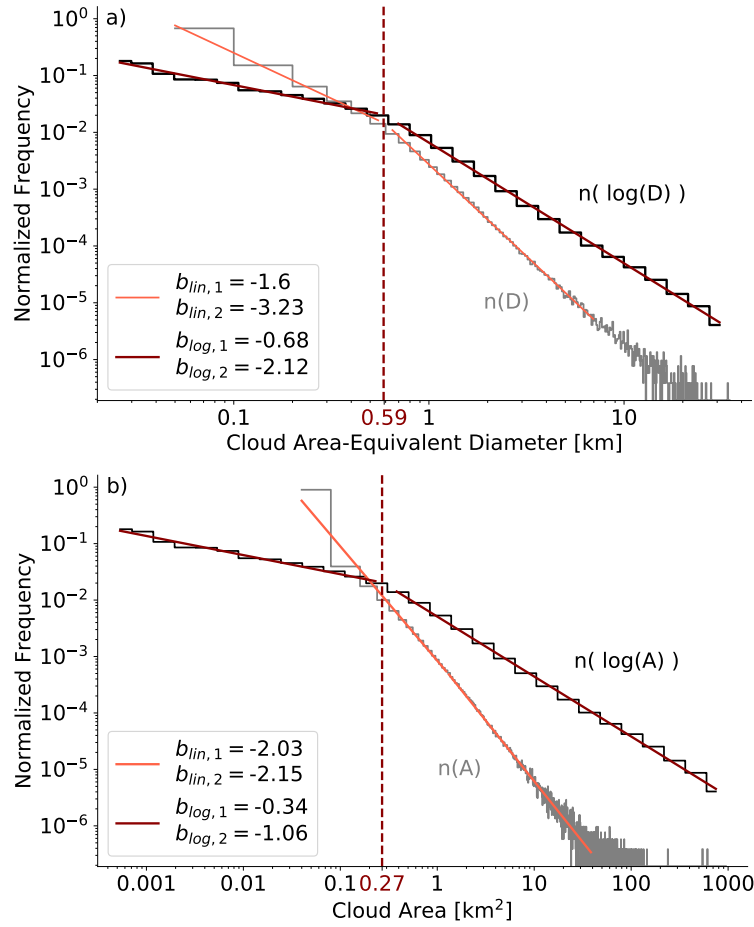


Figure A.5: Cloud size distribution of clouds detected in 1,158 ASTER images. The upper panel shows the distribution of cloud area-equivalent diameter (D), the lower panel the corresponding cloud area (A) covering the same range of cloud sizes. Grey steps and light red lines depict the size distribution and double power-law fit using *linear binning* with equally sized 100 m bins for (D) and 7854 m² bins for cloud area (A) with the scaling parameters b_{lin} . The black steps and the dark red lines show the data and the double power-law fit with scaling parameters b_{log} for *logarithmic binning*. In that latter case, the frequency given on the y-axis is $n(\log(D))$ and $n(\log(A))$ correspondingly. The scale break size D_c (dark red dashed line) is located where the double power-law fit results in a minimum combined least-squares error in the logarithmic case. Note that the area under the curve is only meaningful for the logarithmic case.

any physical processes. A scale-free behavior would be in contrast to many studies arguing for the existence of a scale break size. Stevens (2005) even claims the scale break to be a controlling parameter of the size distribution of shallow cumulus clouds.

An argument supporting the scale break theory states that the natural horizontal scale of eddies within the boundary layer is directly linked to the vertical one.

Plank (1969) finds a cloud width to height aspect ratio of about unity, meaning that one would expect clouds to exhibit a typical horizontal size of about the depth of the boundary layer, 500 - 700 m, which is close to the scale break size found in Figure A.5 and within the range of values stated in the literature (see Table A.1). In line with that, Cahalan and Joseph (1989) relate the scale break to the largest possible cluster size depicted by a single peak in reflectivity at cloud top compared to multiple peaks indicating single cells being aggregated to clusters of cells with various reflectivity peaks resulting in a different scaling behavior of larger clouds. On the other hand, there is also criticism of the various existing scale break theories. Heus and Seifert (2013) show that poor sampling of large clouds in modeling studies produces a change in the slope of the size distribution. In sum, the existence of a true scale break is still a matter of ongoing research, but our results show a scale break size that is close to the depth of the boundary layer.

A.3.2.3 *On the Large Variation of Published Scaling Parameters*

The different fitting procedures mentioned above can contribute to the inconsistency among published scaling parameters. In Table A.1 we summarize scaling parameters of cloud size distributions from past observational and modeling studies and compare them to our results. Beyond listing the original values, we also attempt a first-order harmonization of the scaling parameters. Based on the choice of cloud size measure and binning scheme and using equations A.2, A.4, A.5, and A.6, the published exponents were converted to the equivalent exponent b_{lin} of a common reference corresponding to a power-law in D and linear binning (see section A.2.4). For example, we used logarithmic binning of D in our study, therefore, the slope resulting from a least-squares linear regression b_{log} can be converted to b_{lin} by subtracting 1. These first-order corrections lead to better consistency among the scaling factors. Note, however, that there might be additional hard-to-estimate and hence uncorrected biases between published slopes which arise from differences in sample size, bin width, or lower/upper cutoffs applied to the data. In a first attempt to harmonize the values we assigned reported scaling parameters to either b or b_1 and/or b_2 depending on the range of cloud sizes used for the derivation and the assumption of a single or double power-law. For example, Neggers, Jonker, and Siebesma (2003) only derive one scaling parameter b_1 up to a cut off at the scale break size D_c and argue that no clear behavior can be found for larger cloud sizes. We believe that different scaling parameters in the literature are partly a result of differing fitting strategies and most likely also of too small datasets. We note that in some previous studies, scaling parameters derived by different fitting strategies were directly and thus erroneously compared.

Besides the inconsistency in fitting strategies, the identification of a power-law distribution of cloud sizes by a straight-line behavior in a log-log plot can also be questioned. Clauset, Shalizi, and Newman (2009) states that “such straight-line

behavior is a necessary but by no means sufficient condition for true power-law behavior" from a statistical point of view. The most important shortfalls are the poor representation of the distribution tail and the sensitivity of slope estimates to the choice of the bin width. As an alternative, Clauset, Shalizi, and Newman (2009) proposed a potentially more accurate maximum likelihood estimator (MLE), which is calculated solely from the observed cloud diameter without binning. For the ASTER data we derived two exponents with the MLE method. For small clouds with $D < D_c$ we find $b_{MLE,1} = 1.9$ and for large clouds with $D > D_c$ we calculate $b_{MLE,2} = 3.1$. Both MLE scaling parameters are close to the corresponding values derived by linear regression on logarithmic binned cloud area-equivalent diameters D , confirming that the latter method also results in reasonable values for our dataset. Based on the above, we use the double power-law with its scaling parameters and the scale break size to characterize cloud size distributions in the following analysis.

Study	data type	No. of scenes (sh.cu.)	Scaling parameter			Scale break D_c [km]	Fractal dimension		Cloud Fraction	
			n(x)	b	b ₁		b ₂	d ₁		d ₂
Cahalan and Joseph (1989)	o	< 17	logD	-	-1.6 (-0.6)	-3.3 (-2.3)	0.5	1.34	1.55	0.55
Sengupta et al. (1990)	o	10	D	-	-1.39 to -2.35	~ -2 – -4	~ 1	1.20 – 1.27	1.5 – 1.73	-
Benner and Curry (1998)	o	17	D	-	-1.98	-3.06	0.9	1.23	1.37	0.0925
Zhao and Di Girolamo (2007)	o	152	D	-2.85	-1.88	-3.18	0.6	1.28	-	0.086
Koren et al. (2008)	o	5	logA	-3.6 (-1.3)	-	-	-	-	-	0.1 – 0.25
Peters, Neelin, and Nesbitt (2009)	t/o	-	A	-3.12 (-2.06)	-	-	-	-	-	-
Neggers, Jonker, and Siebesma (2003)	m	1 ^a	logD	-	-1.70 (-0.7)	-	0.7 ^a	-	-	0.14 ^a
Heus and Seifert (2013)	m	1	D	-	-	-2.2	0.4	-	-	0.138
Dawe and Austin (2012)	m	1	D	-	-1.88	-	1	-	-	-
Jiang et al. (2008)	m	1	D	-	-1.9 ^b	-	0.8	-	-	-
This study	o	1,158	logD	-2.55	-1.68	-3.12	0.59	1.19	-	0.087

^a LES results of BOMEX case only.

^b cloud sizes range from 0.3 km to 0.8 km.

Table A.1: Review of cloud size distributions (scaling parameters, scale break size), fractal dimensions and cloud fractions of shallow cumulus cloud fields (sh.cu.) from different observational (o) and modeling (m) studies and from percolation theory (t). The scaling parameters b, b₁, and b₂ refer to the slope of a single power-law and the slopes of a double power-law respectively, all according to equation (A.2). If slopes for n(logD), n(A) or n(logA) are reported in a given study, those numbers are converted to b following equations (A.4), (A.5) or (A.6) and the original value is given in parenthesis. Fractal dimensions according to equation (A.1) are given, either assuming a double power-law with the fractal dimensions d₁ below and d₂ above the scale break D_c or a single power-law with the fractal dimension d₁.

A.4 RELATIONS OF CLOUD FIELD PROPERTIES TO LARGE-SCALE METEOROLOGICAL PARAMETERS

A.4.1 Lower-Tropospheric Stability and Subsidence

During the dry winter season the trades are dominated by subsiding air masses and shallow cumulus, while deeper clouds are found during summer months under weak rising motion (Brueck, Nuijens, and Stevens, 2015). The sampled ASTER images cover a large variety of conditions ranging from weak rising to moderate subsiding motion. The subsidence strength is positively correlated with the lower-tropospheric stability (LTS) (Brueck, Nuijens, and Stevens, 2015; Myers and Norris, 2013), which is the potential temperature difference between 700 hPa and the surface. LTS is a well-established thermodynamic control on tropical low clouds, which has been used in the parameterization of marine stratiform cloud cover in general circulation models (GCMs; Rasch and Kristjansson (1998) and Slingo (1987)). The LTS is essentially a bulk measure of the strength of the capping inversion. A stronger inversion, that is higher LTS, reduces entrainment drying and warming, permitting a moister marine boundary layer and greater cloud cover (Myers and Norris, 2013; Wood and Bretherton, 2006). In Figure A.6 we show variations in cloud field properties with increasing LTS. The vast majority of our scenes have a moderate $LTS < 18.5$ K, which was the threshold value used by Medeiros and Stevens (2011) to discriminate between shallow cumulus and stratocumulus in GCM simulations.

The cloud fraction increases from 5 % to 15 % with increasing stability. However, the rate of increase is only 3 %/K, which is smaller than the sensitivities observed for stratocumulus. Klein and Hartmann (1993) derived a cloud fraction increase with LTS of 6 %/K, Myers and Norris (2013) estimated a cloud fraction sensitivity to the LTS related Estimated Inversion Strength (EIS) of 3.5 - 5.8 %/K, and Qu et al. (2015) found EIS slopes in the range 1.7 - 3.5 %/K. Consistent with LTS, cloud fraction also increases with increasing subsidence, where subsidence is expressed by the pressure vertical velocity at 700 hPa (Figure A.7). However, the signal is much weaker compared to LTS. Subsidence seems to set the general conditions for the development of trade wind cumuli, but cloud field properties remain fairly constant for subsidence rates smaller than 0.1 Pa/s, which agrees with findings of Eitzen, Xu, and Wong (2011) for marine stratocumulus.

In contrast to the increase in cloud fraction, cloud-top height stays fairly constant with increasing subsidence and stability. However, the change in cloud cover partly results from the change in cloud size distribution. We observe a change to steeper

(more negative) b_1 slopes, considerably less steep b_2 slopes, accompanied by a slight increase in the scale break size from 0.55 km to 0.70 km. All parameters indicate a relative shift of the cloud size distribution towards more frequent large clouds, which is accompanied by an overall increase in the total number of clouds detected. We hypothesize that in situations of strong subsidence and high LTS clouds spread laterally at a strong inversion layer. Therefore, individual projected cloud areas, as well as the overall cloud fraction increase. Our results are in line with observations at the BCO, where LTS was identified to control low-cloud amount (Brueck, Nuijens, and Stevens, 2015).

The fractal dimension shows only a marginal decrease meaning that cloud shapes do not change significantly. In general, the fractal dimension tends to approach smaller values (smoother shapes), whenever the scaling parameters of the cloud size distribution indicate larger clouds in our dataset. However, dependencies of fractal dimension on certain meteorological parameters are usually small. The last panel in Figure A.6 provides insight into the change in the spatial clustering of observed cloud fields. Both applied indices, SCAI and I_{org} , show a decrease in spatial aggregation with increasing stability. Note that disaggregated states correspond to high SCAI and low I_{org} values. High LTS, often related to strong subsidence, seems to inhibit clouds from organizing into clusters or arcs, which can frequently be seen over tropical oceans. However, we note that both indices have major shortcomings as discussed in section A.2.5 and results should not be overinterpreted.

Myers and Norris (2013) argue that the climatological positive correlation between subsidence and marine boundary layer cloudiness is not the result of a direct physical mechanism, but rather arises because enhanced subsidence is usually associated with larger LTS (stronger temperature inversion), which promotes greater cloudiness. They point out that enhanced subsidence alone actually leads to reduced cloud fraction by lowering the top of the boundary layer. The independent effect of enhanced subsidence and the associated effect arising from its covariation with LTS are therefore opposite, which can lead to partial cancellation. This might explain the insensitivity of cloud properties to subsidence in our bin analysis, which cannot separate out these two opposing mechanisms. The increase in shallow cumulus cloud fraction observed for the strongest subsidence rates then indicates the dominance of LTS over subsidence as a predictor of cloudiness, similar to findings for stratocumulus cloud fields.

A.4.2 Sea Surface Temperature and Moisture

Sea surface temperature (SST) is an important driver in the break up of marine stratocumulus to shallow cumulus clouds in the tropics. Past studies agree on a decrease in cloud fraction with increasing SST (Klein and Hartmann, 1993; Qu et al., 2015; Stein et al., 2017), although they disagree on the underlying mechanism. A possible physical mechanism explaining the robust negative correlation is the increase in surface moisture fluxes with increasing SST and a deepening of the trade wind boundary layer. The deepening response may result in increased entrainment of warm and dry free tropospheric air into the cloud layer which reduces cloudiness (Rieck, Nuijens, and Stevens, 2012). A second idea is that SST increase enhances the humidity contrast between the surface and the free troposphere, leading to increased mixing of drier free tropospheric air into the boundary layer and reduced cloud fraction (Dussen et al., 2015). A third proposed explanation is that a warmer SST increases the efficiency of entrainment (larger buoyancy flux per unit cloud depth), requiring thinner and smaller clouds to maintain a constant cloud-top entrainment rate (Bretherton and Blossey, 2014). Finally, it has also been argued that the decrease of stratocumulus amount with SST may simply be due to a negative correlation between LTS and SST (Eitzen, Xu, and Wong, 2011; Kubar et al., 2012).

All stated mechanisms are strongly coupled to the lower tropospheric moisture motivating its separate consideration in our study. We note that moisture influences shallow clouds in many different ways. Surface moisture fluxes introduce moisture to the well-mixed subcloud layer, which builds a reservoir of moisture that potentially is transferred into the cloud layer and forms clouds. On the other hand, advected cold air can decrease the lower tropospheric moisture in the trade wind region. Similarly, entrainment of warm and dry free-tropospheric air at the top of the cloud layer can decrease the moisture content in the cloud layer. The relative importance of these mechanisms is the subject of ongoing research. MODIS-Terra provides estimates of the total column water vapor (TCWV), which are concurrent with ASTER observations and are therefore used in the present study. Changes in TCWV are largely determined by water vapor located between the top of the well-mixed subcloud layer and the height of the triple-point isotherm (Stevens et al., 2018). An increase especially in water vapor above cloud tops can increase the absorption of outgoing longwave radiation and thus change the temperature profile, cloud top subsidence and cloud top entrainment rates, all leading to a change in cloud field properties (Myers and Norris, 2013).

Figures A.8 and A.9 show shallow cumulus cloud field properties as a function of SST and TCWV. From ASTER observations we can confirm the decrease of cloud

fraction with increasing SST as well as with increasing TCWV, a feature that all mentioned mechanisms have in common. The decrease between the coldest and warmest SST bin and the decrease from the driest to the moistest bin are both about 10 %, which is approximately the same magnitude as the overall cloud fraction increase with LTS (see Figure A.6). The rate of decrease in shallow cumulus fraction with SST is 1 - 2 %/K, which is smaller than the SST sensitivities previously observed in stratocumulus. The reported SST sensitivities are amongst others -5 %/K in Klein and Hartmann (1993), -3.4 %/K in Eitzen, Xu, and Wong (2011), -6.5 %/K in Kubar et al. (2012), and -1.3 %/K to -3.7 %/K in Qu et al. (2015). Similar to LTS relations, we attribute the cloud fraction changes with SST and TCWV to relative changes in the frequency of certain cloud sizes and to the overall decrease in the total number of clouds. With higher SST and TCWV the scaling parameters and the scale break size indicate a reduced amount of large clouds and only a slight increase in the amount of small clouds. The fractal dimension shows a small overall increase with SST, in line with the general finding that smaller clouds tend to be more irregular in our dataset. In addition, the cluster indices show a change in the spatial distribution towards stronger clustering of clouds with increasing SST and TCWV. Reasons for and implications from this relation, however, are subjects of ongoing investigations.

Neglecting the coldest SST bin, cloud-top heights decrease as SST and TCWV increase, showing especially a strong decrease of about 400 m from the driest to the moistest bin. A decrease in cloud top heights seems inconsistent with the surface-flux desiccation mechanism present in the simulations of Rieck, Nuijens, and Stevens (2012), whereby increased moisture fluxes produce fewer but deeper cumulus clouds that carry more liquid water and have higher tops. The observed lowering of cumulus tops with SST, however, appears consistent with the entrainment liquid-flux adjustment feedback described in Bretherton and Blossey (2014). According to their model simulations, surface fluxes and turbulence intensify with increasing SST. However, stronger turbulence induces a stronger mixing of dry free tropospheric air into the cloud layer at the trade wind inversion layer. The dry and warm air leads to cloud thinning and lower cloud tops, which we can observe in the ASTER dataset.

A.4.3 Surface Easterly Trade Winds

The tropical ocean in the trade wind region provides the moisture supply for the shallow cumulus cloud layer. The trade winds themselves regulate the moisture transport from the surface upwards by surface fluxes of heat, moisture, and momentum and thereby have a controlling role on the development and characteristics of

shallow cumulus cloud fields. In an early observational study by Klein (1997), wind speed and surface wind stress were found to positively correlate with low-cloud amount in the tropical eastern Pacific. Similarly, Brueck, Nuijens, and Stevens (2015) showed that wind speed has the best correlation with MODIS monthly-mean low-cloud amount in the North Atlantic trades.

The physical and dynamical mechanisms involved in the coupling between the trades typical surface easterly winds and the macrophysical properties of shallow cumulus cloud fields have been subject to several observational and modeling studies. Using ground-based radar data from the RICO field campaign, Nuijens, Stevens, and Siebesma (2009) observed that periods of stronger shallow cumulus precipitation are characterized by deeper and moister layers and stronger easterlies, concluding that a more humid environment promotes deeper clouds and the humidity itself is regulated by wind speed. In addition, stronger surface winds frequently occur in combination with horizontal cold air advection, which increases the upward buoyancy flux and promotes more clouds by destabilizing the surface-atmosphere interface (Klein, 1997; Norris and Iacobellis, 2005). Simulations of an idealized non-precipitating shallow cumulus case by Nuijens and Stevens (2012) showed considerable deepening of the cloud layer at higher wind speeds. Applying concepts from bulk theory, the deepening is a necessary response to allow the surface buoyancy flux to remain constant without further moistening the sub-cloud layer in its adjustment to a new equilibrium. In the simulation, the cloud layer deepens, enabling deeper and larger clouds to form. Wind speed is positively correlated with wind shear and enhanced wind shear might further enhance the projected cloud cover as deeper and larger clouds get tilted with height (Brueck, Nuijens, and Stevens, 2015; Neggers, Jonker, and Siebesma, 2003).

While Nuijens and Stevens (2012) promote a wind speed-regulated and deepening trade wind boundary layer, the LES study by Bretherton, Blossey, and Jones (2013) similarly finds larger clouds with increasing wind speed, but a limited variation of boundary layer depth. In the precipitation-permitting study of Bretherton, Blossey, and Jones (2013), higher wind speed leads to increased surface-driven turbulence, increased latent heat flux and thus more cloud. This study illustrates the so-called “precipitation governor” mechanism, which limits inversion height changes. As cumulus clouds become deep enough they precipitate more efficiently, which reduces the supply of liquid water to the inversion layer and prevents a significant deepening of the cloud layer.

From analyzing ASTER images we do find the strongest and most systematic variation in cloud field properties with wind speed. Figure A.10 shows a strong increase in cloud fraction by about 15 % from low to high wind speed situations. Similarly, the cloud top heights increase on average by 400 m indicating deeper

clouds as the cloud base height over the ocean is fairly constant. Deeper clouds coincide with a higher frequency of large clouds which is obvious from the opposing changes of the double power-law scaling parameters b_1 and b_2 . The scale break size D_c increases with increasing wind speed from 440 m to about 1300 m, similarly implying a shift in the size distribution towards larger clouds. Visually the change in the shape of the distribution becomes even clearer in Figure A.11 where the distribution is shown for the lowest, middle, and highest wind speed bin. Taking the actual cloud area instead of the commonly used cloud area-equivalent diameter results in the same qualitative change in the cloud size distribution (not shown here) confirming the robustness of our findings to the different definitions for cloud size.

Increasing cloud sizes and the deepening of the cloud layer is consistent with the non-precipitating shallow cumulus simulations of Nuijens and Stevens (2012) and thus confirms a primarily wind speed-regulated boundary layer. Shallow cumulus precipitation unfortunately cannot be diagnosed from passive satellite measurements and even current space-borne radars would miss a large portion of the light rains encountered in these clouds, but ground-based radar data show that shallow precipitation is indeed ubiquitous (Nuijens, Stevens, and Siebesma, 2009). Nevertheless, the observed CTH increase implies that the precipitation governor mechanism of Bretherton, Blossey, and Jones (2013) seems too weak to prevent the cloud layer deepening response in our dataset.

The fractal dimension d in Figure A.10c decreases with wind speed, indicating a transition from ragged shapes to more compact and smooth cloud shapes (d close to 1). In a calm environment, enhanced entrainment of dry air at cloud edges might lead to ragged cloud edges. This idea is supported by a parameterization of moist convection in a rising plume model by Neggers (2015), where the entrainment is assumed to decrease with increasing plume size. We hypothesize that stronger winds introduce an anisotropy in cloud growth, inhibiting it upwind and promoting it downwind. As a result, individual clouds may be elongated in the wind direction or tilted out of the vertical, as wind shear also tends to increase with wind speed. It is therefore not difficult to imagine how the structure imposed on the flow by stronger winds could result in smoother cloud shapes with smaller fractal dimensions.

According to the last panel in Figure A.10, wind speed influences not only cloud shapes, but also the spatial distribution of clouds. The increase in SCAI as well as the decrease in I_{org} with increasing wind speed means that cloud fields are less aggregated in high wind speed cases. One can easily imagine that strong winds inhibit organized convection, although the exact mechanisms are unclear at this stage. We studied the change in SCAI in more detail as it is governed by

two variables, the total number of clouds in an image and the average distance between all clouds (see equation A.7). We found that the increase in SCAI with increasing wind speed in low wind speed situations is due to an increase in the total number of clouds. We hypothesize that the increase in wind speed goes along with an increase in moisture being mixed upwards which provides the basis for new cumulus clouds to develop. On the other hand, the increase in SCAI in high wind speed situations results from a strong increase in the average distance between the clouds, which clearly dominates the calculated SCAI values as the number of clouds decreases simultaneously. Taking into account that clouds also tend to be larger in the case of high surface winds, we propose that larger clouds suppress convection in close proximity, leading to higher average distances between clouds in a fixed domain.

The variation of cloud field properties with wind speed might include wind shear effects too, as wind speed and wind shear are positively correlated (Brueck, Nuijens, and Stevens, 2015). We define a scene-average wind shear as the absolute value of the wind vector difference between 700 hPa and 1000 hPa. Although it covaries with wind speed, shear itself induces little systematic variation in cloud properties, as most cloud field properties simply fluctuate around their mean values (see Figure A.12). Only cloud fraction exhibits a 4 % increase at the highest wind shear values above 9 m/s, most likely due to the tilting of cumulus towers (Neggers, Jonker, and Siebesma, 2003). The observed minor changes are consistent with the observational study by Brueck, Nuijens, and Stevens (2015) and the modeling study by Nuijens et al. (2015), both claiming that wind shear plays a minor role in regulating cloud fields in the trade wind region.

In conclusion, our results support the hypothesis of a deepening response of the trade wind boundary layer to increasing surface wind speed. Clouds are found to be deeper and horizontally larger leading to an increase in cloud fraction. This result is in agreement with studies by Nuijens and Stevens (2012) and Brueck, Nuijens, and Stevens (2015) where wind speed is found to be the major control factor on low-level cloudiness in observational data at the BCO. Both studies provide a physical explanation for the observed changes by linking higher wind speeds to enhanced evaporation over the ocean that alters the surface fluxes. Surface sensible and latent fluxes are governed by wind speed and the difference in temperature and moisture between the surface and cloud base. An increase in wind speed therefore results in an enhanced moisture and mass flux into the cloud layer, jointly leading to a change in cloud field properties.

A.4.4 Bowen Ratio

The influence of wind speed-driven surface fluxes on shallow convection is subject to a recent LES study from Sakradzija and Hohenegger (2017), which investigates parameters that influence the distribution of cloud-base mass flux under time-invariant profiles of subsidence, horizontal advection, background wind and a fixed SST. They concluded that the Bowen ratio (B), the ratio of the surface sensible heat flux to the latent heat flux, controls the shape of the cloud-base mass flux distribution by setting the thermodynamic efficiency of the moist convective heat cycle. While the surface wind speed is correlated with both of the surface fluxes, with a Pearson correlation coefficient for latent heat flux $r_l = 0.7$ and for sensible heat flux $r_s = 0.4$, it is uncorrelated with the corresponding Bowen ratio, $r_B = 0.1$, which thus can be viewed independently. Sakradzija and Hohenegger (2017) found that cloud area is distributed similarly to cloud-base mass flux with the distribution slopes systematically changing as B increased from a baseline value of 0.03 to 0.24 and to 0.33.

Motivated by this study, we show variations in ASTER cloud field properties, in particular the cloud size distribution, with Bowen ratio in Figure A.13. We derive B from ERA-Interim surface fluxes and find a narrow distribution of B around the average value of 0.08. Furthermore, about 2 % of the values are negative, which, however, are of minor importance as they are not covered by the LES runs. According to Sakradzija and Hohenegger (2017), typical values for B over the Atlantic ocean during the RICO campaign were about 0.05. In Figure A.13, such a low value for B corresponds to low cloud fractions around 7 %, cloud-top heights of about 1.2 km and rather aggregated cloud fields. With increasing B the cloud fraction and cloud-top height increase and the scaling parameters and scale break size indicate a higher frequency of large clouds. Higher cloud tops and the changes in the cloud size distribution are in qualitative agreement with the LES results, where cloud-base mass flux distribution shifts towards higher values with B . The distribution of cloud-base areas simulated by Sakradzija and Hohenegger (2017) had a scale break around 10^5 m^2 , which compares reasonably well with the scale break size of $2.7 \cdot 10^5 \text{ m}^2$ observed in our dataset (see Figure A.5b). The fractal dimension on the other hand does not show any systematic behavior.

In LES, ocean surface winds set the rate of heat and moisture that is transported upwards into the cloud layer potentially forming clouds. Based on the preceeding analysis of wind speed influence on ASTER cloud field properties and the theoretical concept of shallow moist convection by Sakradzija and Hohenegger (2017), we conclude that wind speed indeed has a major control, possibly through altering the ratio of the surface fluxes. The fact that the influence of surface wind speed

and not that of B shows the strongest changes in cloud field properties might be the result of the insufficient accuracy of ERA-Interim reanalysis data for this study. The small range of B values might be a further limiting factor.

A.4.5 Schematic Summary of Observed Correlations

In Figure A.14 we summarize the observed effects of cloud-controlling factors on shallow cumulus clouds. In particular, we illustrate how shallow cumuli change in size, cloud top height, and how the cloud fraction evolves. The sketched change of a cloud corresponds to the average change with increasing value of a given large-scale meteorological parameter. For every parameter we hypothesize the dominant mechanism and provide the most relevant literature. We emphasize again, that surface wind speed shows the strongest signal of all cloud-controlling factors in our study, followed by lower-tropospheric stability, Bowen ratio, sea surface temperature and total column water vapor. The subsidence rate and wind shear, in contrast, do not show significant influences on cloud field properties.

A.5 SUMMARY AND CONCLUSIONS

We investigated the influence of large-scale meteorological fields on shallow cumulus cloud fields as observed in 1,158 high-resolution satellite images from ASTER which were collected over the tropical Atlantic and Pacific oceans between 2000 and 2007. The high spatial resolution of the ASTER sensors facilitates the investigation of clouds on scales smaller than 1 km. We characterize cloud fields observed in ASTER imagery by their macrophysical properties and go beyond most prior studies in covering not only cloud fraction, but also cloud-top height, cloud size distribution, fractal dimension, and horizontal cloud distribution or spatial clustering. We investigate the variation of these cloud properties with meteorological parameters from ERA-Interim, specifically, subsidence rate, lower-tropospheric stability (LTS), sea surface temperature (SST), total column water vapor (TCWV), surface wind speed, wind shear, and the Bowen ratio.

From 1,158 cloud images an average cloud fraction of 8.7% is calculated, with 90% of the individual scenes having a cloud fraction below 20%. The distribution of scene-average CTHs exhibits a single peak just below the average CTH of 1.3 km. The ensemble of clouds is characterized by the cloud size distribution and the fractal dimension. Estimating the power-law scaling parameter of cloud size distributions

from linear fits to histograms in a log-log plot gives predictably different results, depending on the cloud size measure (equivalent diameter or area) and binning scheme (linear or logarithmic) used. We show that the distribution of shallow cumulus clouds can be well described by a double power-law with the scaling parameters of $b_1 = 1.68$ for small cloud sizes and $b_2 = 3.12$ representing the large cloud sizes. A characteristic scale break at about 0.6 km is found in agreement with previous studies reporting values ranging from 0.5 km to about 1 km. We argue that the large range of scaling parameters stated in the literature is partly due to different fitting strategies and in some cases due to insufficiently small data samples. The derived fractal dimension of $d = 1.19$ means that the sampled clouds are rather compact and exhibit smoother shapes compared to previous studies. The analysis of the cloud spatial distribution reveals that shallow cumulus clouds appear almost exclusively in the form of clustered cloud fields. The aggregation index SCAI exhibits a skewed distribution indicating a higher occurrence of clustered cloud fields and the organization index I_{org} strongly confirms the overall tendency towards clustered cloud fields with a narrow distribution around the average value of $I_{\text{org}} = 0.89$.

Based on the variation of cloud field properties we evaluated the role of large-scale meteorological parameters in controlling shallow clouds. Large-scale subsidence is one of the key features in the trade wind region, which provides the general conditions for the development of shallow cumulus cloud fields. Nevertheless, we find only weak relationships between cloud field properties and the subsidence rate. It is found that shallow cumulus amount shows the same overall dependencies on control factors as the more often studied marine stratocumulus amount. Specifically, shallow cumulus fraction steadily increases with increasing LTS, increasing surface wind speed, decreasing SST, decreasing TCWV, and increasing Bowen ratio. Clouds tend to be slightly larger in very stable situations and under moderate subsiding motion, leading to an increase in cloud fraction. Analyzing variations in shallow cumulus cloud field properties with SST and TCWV proved known behavior from LES studies, such as reduced cloud cover, a higher frequency of small clouds and a higher cluster tendency with increasing SST and TCWV. Shallow cumulus cloud fields seem to respond to meteorology in a similar way as stratocumulus, although the absolute sensitivities to control factors are smaller.

Prominent trade winds, however, emerge as the most powerful control factor, as all cloud macrophysical properties show the strongest and most systematic variation with change in the strength of surface wind speed. Our observations are consistent with the hypothesis from modeling studies that surface wind speed drives the surface fluxes and therefore the moisture and momentum transport into the cloud layer, leading to a deepening of the trade wind boundary layer. Strong winds produce large clouds with smooth and compact cloud shapes and

also higher cloud cover. We hypothesize that smoother cloud shapes might arise from strong winds coupled with increased shear imposing an anisotropy on cloud growth, inhibiting it upwind and promoting it downwind, resulting in more regular elongated shapes and thereby explaining the observed decrease in fractal dimension. Cloud-top height also increases with wind speed by a significant amount, lending observational support to the deepening response present in an LES study of a non-precipitating trade cumulus case by Nuijens and Stevens (2012). In situations of low surface wind speed we observe a tendency towards clustered cloud fields, while strong winds seem to inhibit cloud fields from organizing into clusters or arcs. Although wind speed and wind shear are correlated, we cannot find any significant variation in cloud field properties with the bulk wind shear and conclude that wind shear is of minor importance in regulating shallow cumulus clouds in the trade wind boundary layer.

In addition, we investigated the relationships between cloud field properties and the Bowen ratio, which is related to wind speed through the surface fluxes. The Bowen ratio is a potential new control factor proposed by a recent LES study of Sakradzija and Hohenegger (2017) to control the shape of the cloud area distribution by setting the thermodynamic efficiency of the moist convective heat cycle. The change in the cloud size distribution slopes, the shift toward larger clouds and larger cloud fractions, and the increase in cloud-top height observed in our dataset with increasing Bowen ratio all qualitatively agree with the LES simulations, suggesting that the effect of this parameter on trade-wind cloudiness merits further investigation.

This study lends observational support to some of the proposed control mechanisms of shallow cumulus clouds. However, we explicitly note that relationships do not imply any physical or dynamical causality, but merely support ideas on possible mechanisms and give room for new hypothesis. Neither surface wind speed, nor the subsidence of air masses or further large-scale meteorological variables stand out alone as the main driver of the observed cloud fields. The covariance of these parameters is a further complicating factor and needs to be studied in more detail. Understanding control parameters more accurately can improve convective parametrization schemes in general circulation and large-eddy models and eventually reduce some uncertainty in climate projections.

A.6 APPENDIX

A.6.1 Dependence of scaling parameters on cloud size measure and binning method

Cloud size distributions are often assumed to follow a power-law, but past studies estimated scaling parameters in different ways, which can lead to confusion. In the following, we explicitly derive the mathematical relations between the scaling parameters resulting from different binning methods and different cloud size measures.

We assume that the cloud size density $n(D)$ of the cloud area-equivalent diameter D follows a power-law:

$$n(D) = c \cdot D^b \quad (\text{A.9})$$

The total number of clouds N is the integral over the cloud size density $N = \int_0^\infty n(D) dD$ and accordingly $n(D) = dN/dD$ and $n(\log(D)) = dN/d\log(D)$.

Independent of the exact definition of the cloud size measure, the integral $\int_0^\infty n(D) dD$ is a conserved quantity. Therefore, we can relate $n(\log(D))$, $n(A)$ and $n(\log(A))$ to $n(D)$:

$$\int_0^\infty n(D) dD = \int_0^\infty n(x) dx \quad (\text{A.10})$$

For $x = \log(D)$ and $\frac{dx}{dD} = \frac{1}{D \cdot \ln(10)}$:

$$\begin{aligned} n(\log(D)) &= n(D) \cdot D \cdot \ln(10) \\ &= c \cdot \ln(10) \cdot D \cdot D^b \\ &= c' \cdot D^{b+1} \end{aligned} \quad (\text{A.11})$$

For $x = A = \frac{\pi}{4} \cdot D^2$ and $\frac{dx}{dD} = \frac{\pi}{2} \cdot D$:

$$\begin{aligned}
 n(D) &= n(A) \cdot \frac{dA}{dD} \\
 &= n(A) \cdot \frac{\pi}{2} \cdot D \\
 n(A) &= n(D) \cdot \frac{2}{\pi} \cdot D^{-1} \\
 &= c \cdot \frac{2}{\pi} \cdot D^{b-1} \\
 &= c'' \cdot A^{\frac{b-1}{2}}
 \end{aligned} \tag{A.12}$$

for $x = \log(A) = \log(\frac{\pi}{4} D^2)$ and

$$\begin{aligned}
 \frac{dx}{dD} &= \frac{1}{\frac{\pi}{4} D^2 \cdot \ln(10)} \cdot \frac{\pi}{2} D \\
 &= \frac{2}{\ln(10)} D^{-1}
 \end{aligned} \tag{A.13}$$

$$\begin{aligned}
 n(\log(A)) &= n(D) \cdot \frac{\ln(10)}{2} D \\
 &= c \cdot \frac{\ln(10)}{2} \cdot D^{b+1} \\
 &= c''' \cdot A^{\frac{b+1}{2}}
 \end{aligned} \tag{A.14}$$

ACKNOWLEDGEMENTS The study was supported by the International Max Planck Research School on Earth System Modelling (IMPRS-ESM), Hamburg, and the Universität Hamburg. The contribution of Stefan A. Buehler was supported through the Cluster of Excellence CliSAP (EXC177), Universität Hamburg, funded by the German Science Foundation (DFG) (contract O1LK1502B), and the work of Ákos Horváth was supported by the BMBF project HD(CP)² (contract O1LK1505D). We would like to thank Chris Bretherton, Matthias Brueck and Cathy Hohenegger for useful discussions on the structure and prevailing dynamical processes in the trade wind boundary layer. Theresa Mieslinger would like to thank Lukas Klufft and Oliver Lemke for their IT support. The authors declare no financial conflicts of interests.

The ASTER L1B and the MODIS data products were retrieved from the online Data Pool, courtesy of the NASA Land Processes Distributed Active Archive

Center (LP DAAC), USGS/Earth Resources Observation and Science (EROS) Center, Sioux Falls, South Dakota, https://lpdaac.usgs.gov/data_access/data_pool. We acknowledge ECMWF and the Copernicus Climate Change Service for providing access to the ERA-Interim dataset through their public data portal. The Python functions implemented for calculating cloud field statistics are freely available within the python package *typhon*, subpackage *cloudmask* (<http://doi.org/10.5281/zenodo.1300319>).

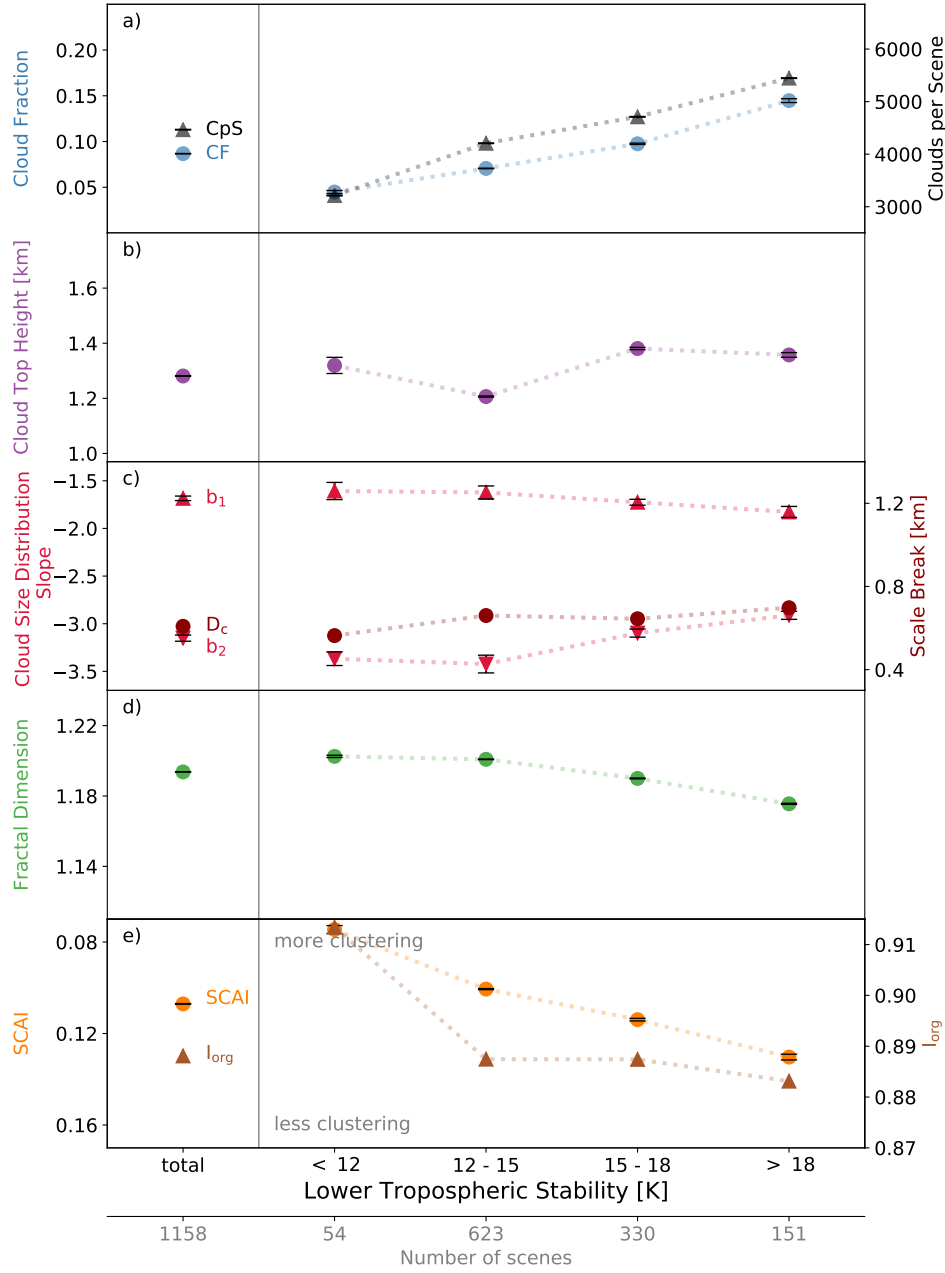


Figure A.6: Cloud field properties as a function of lower-tropospheric stability (LTS). The properties derived from 1,158 ASTER images are sorted according to the scene-average LTS calculated from ERA-Interim reanalysis temperatures. a) shows cloud fraction and b) the cloud top height. In c) the size distribution of cloud area-equivalent diameters is represented by the scaling parameters b_1 and b_2 of a double power-law fit with the scale break size D_c . The fractal dimension d is plotted in d), while the spatial distribution of clouds is quantified by the cluster indices SCAI (note: y-axis reversed) and I_{org} in e). Error bars display the standard error in the mean for average values and the error in the slope for the scaling parameters and fractal dimension.

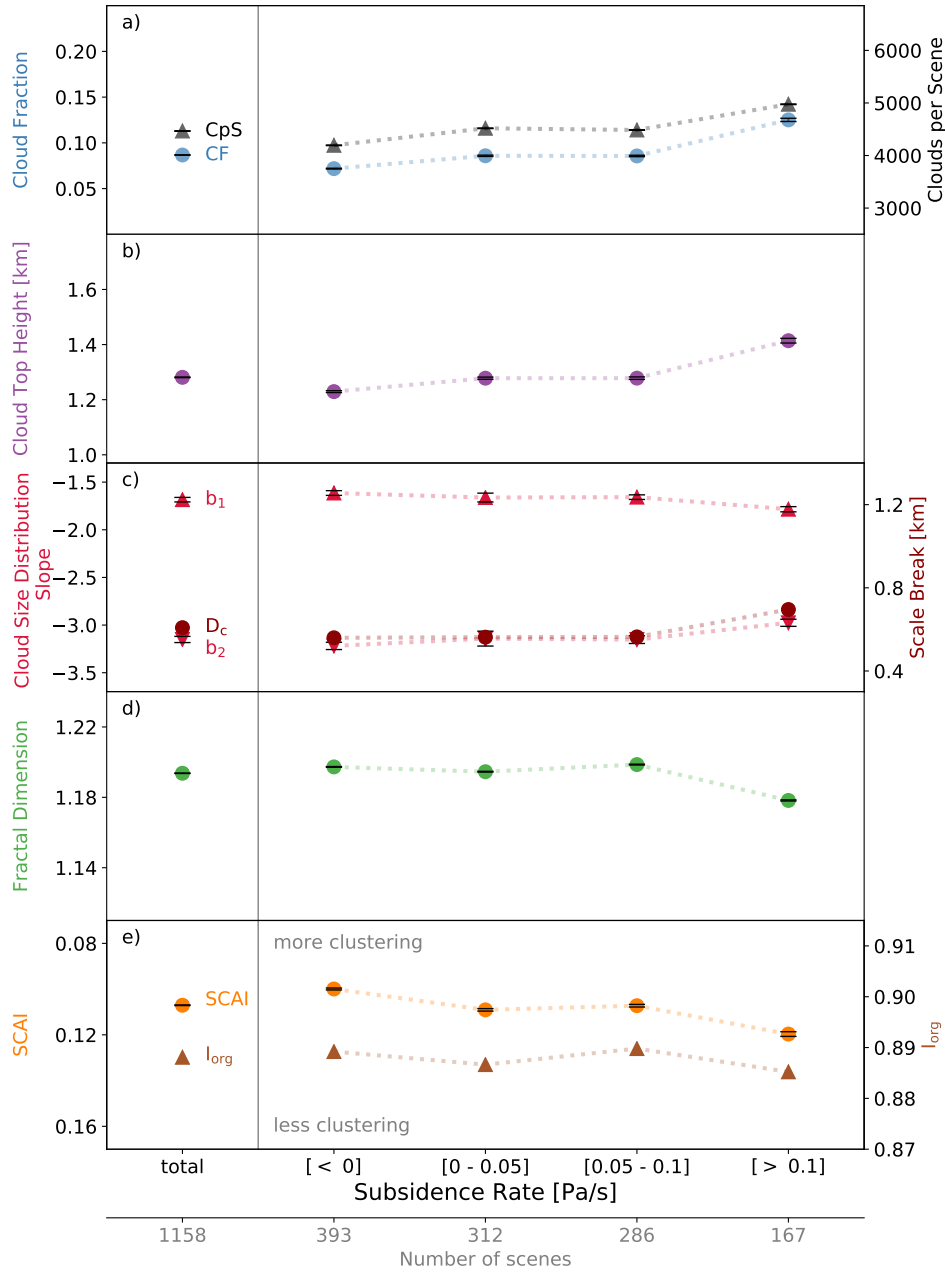


Figure A.7: Same as Figure A.6, but for subsidence rate at the 700 hPa pressure level.

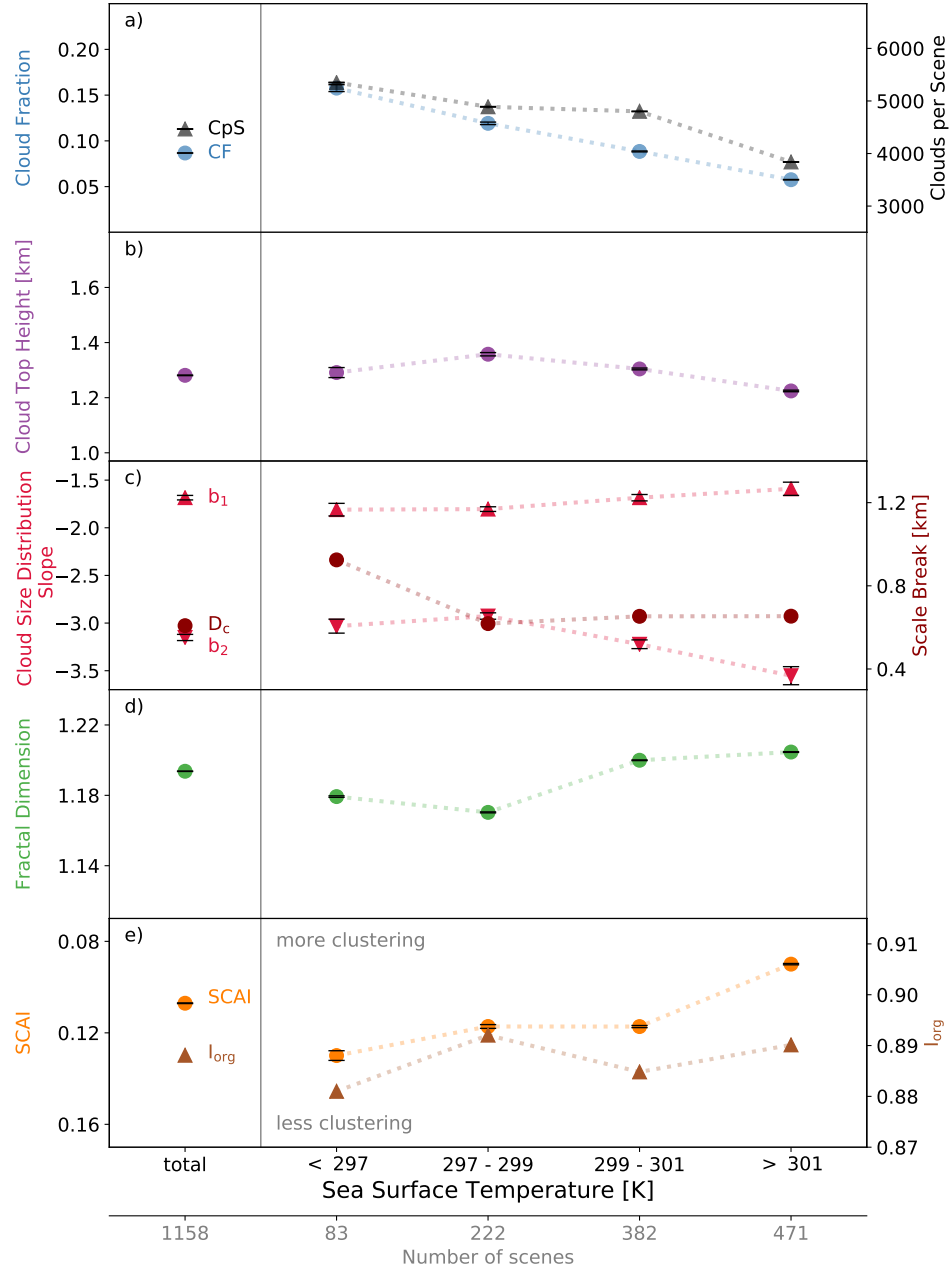


Figure A.8: Same as Figure A.6, but for sea surface temperature (SST).

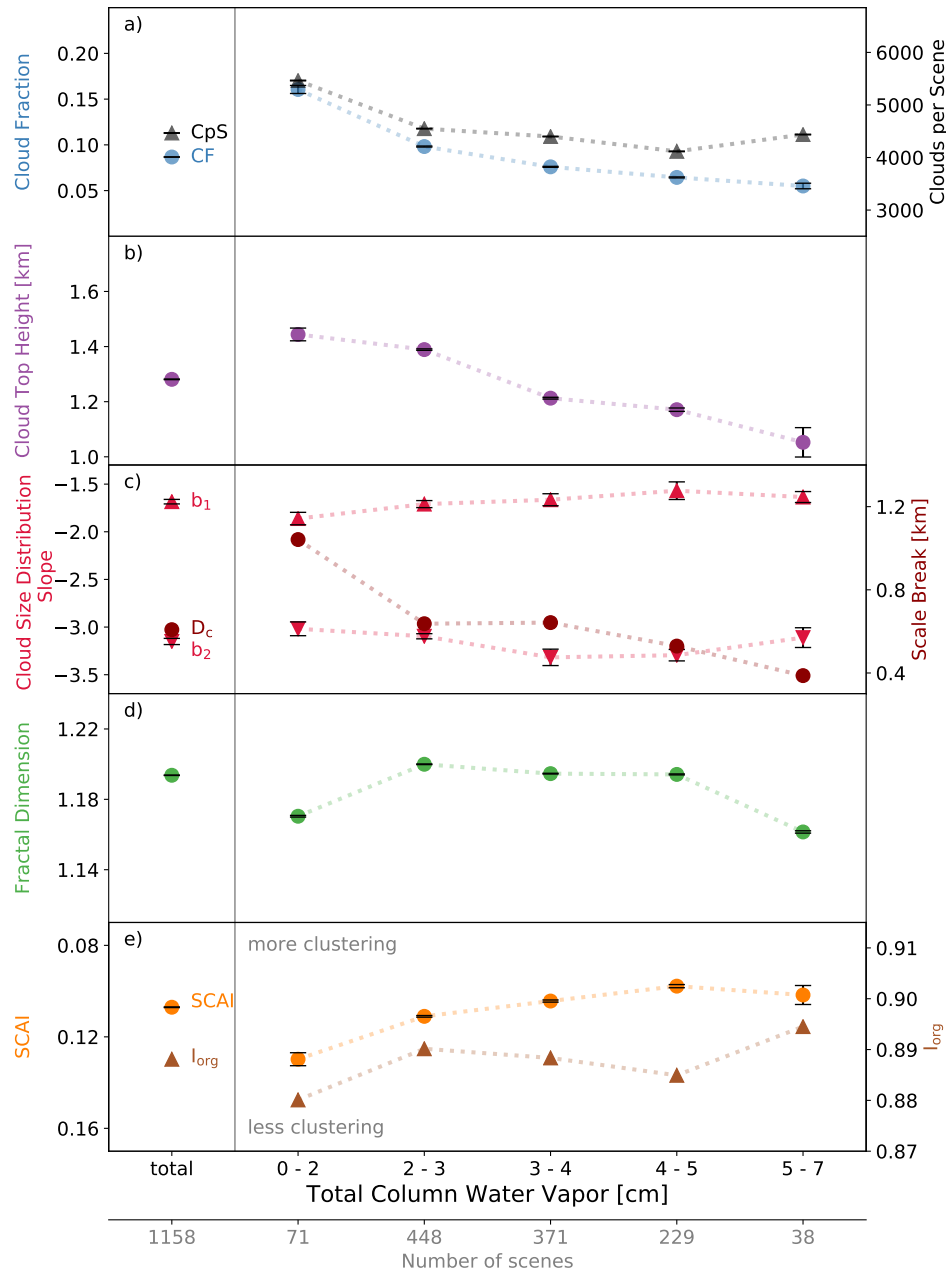


Figure A.9: Same as Figure A.6, but for total column water vapor (TCWV).

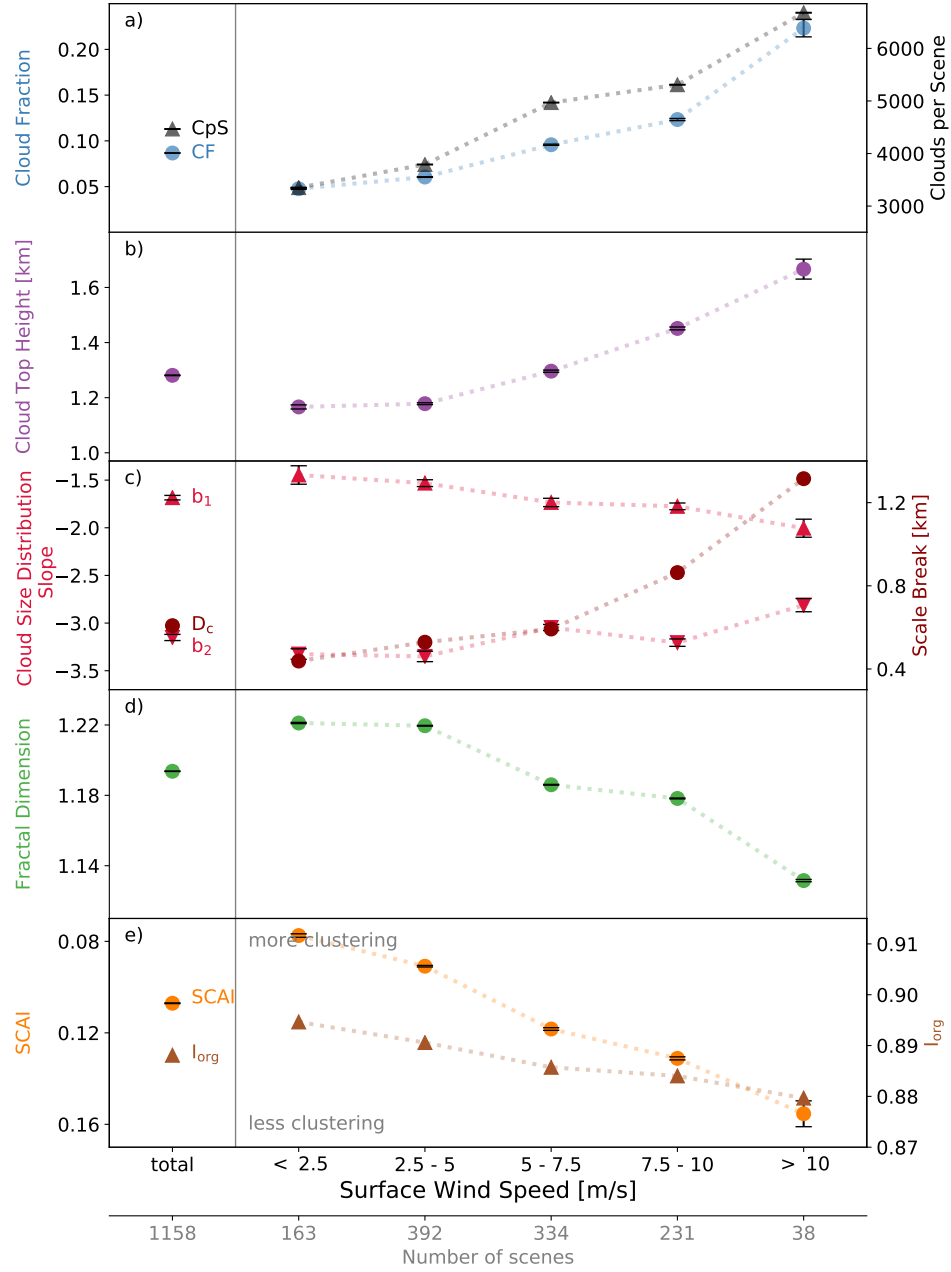


Figure A.10: Same as Figure A.6, but for surface wind speed.

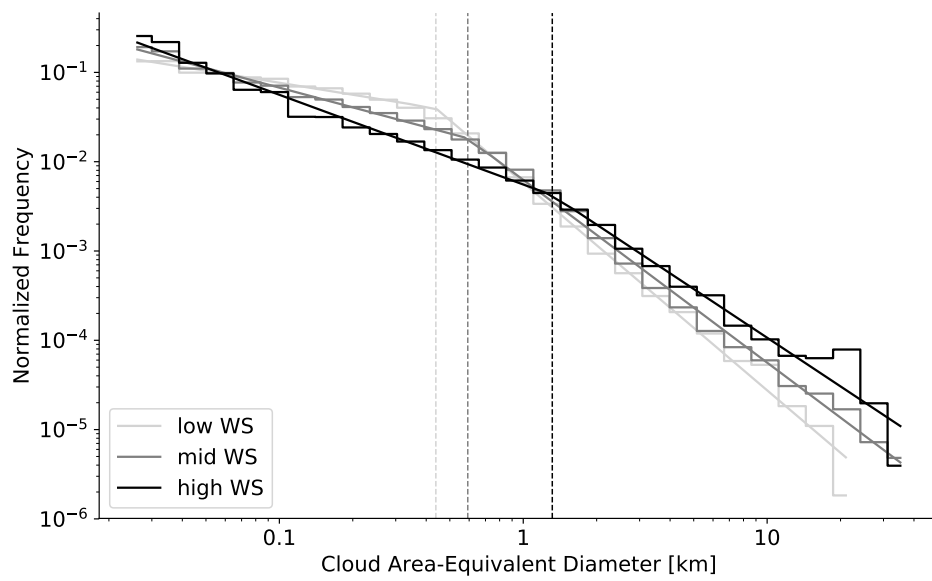


Figure A.11: Cloud size distributions under low ($< 2.5 \text{ ms}^{-1}$), mid ($5 - 7.5 \text{ ms}^{-1}$) and high ($> 10 \text{ ms}^{-1}$) wind speed cases. Steps display the size distributions, solid lines the double power-laws from linear regression, and the dashed lines depict the corresponding scale breaks.

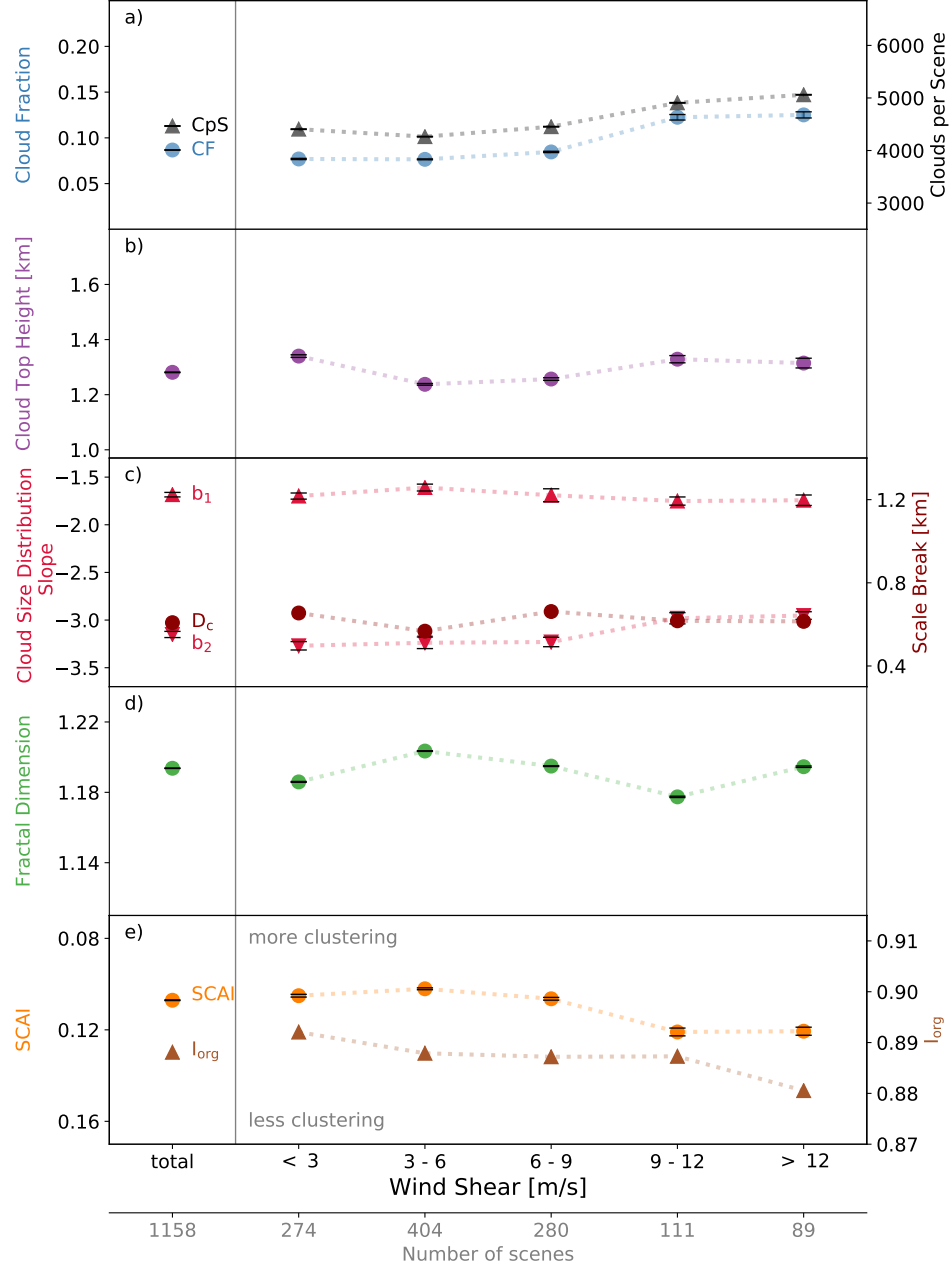


Figure A.12: Same as Figure A.6, but for wind shear.

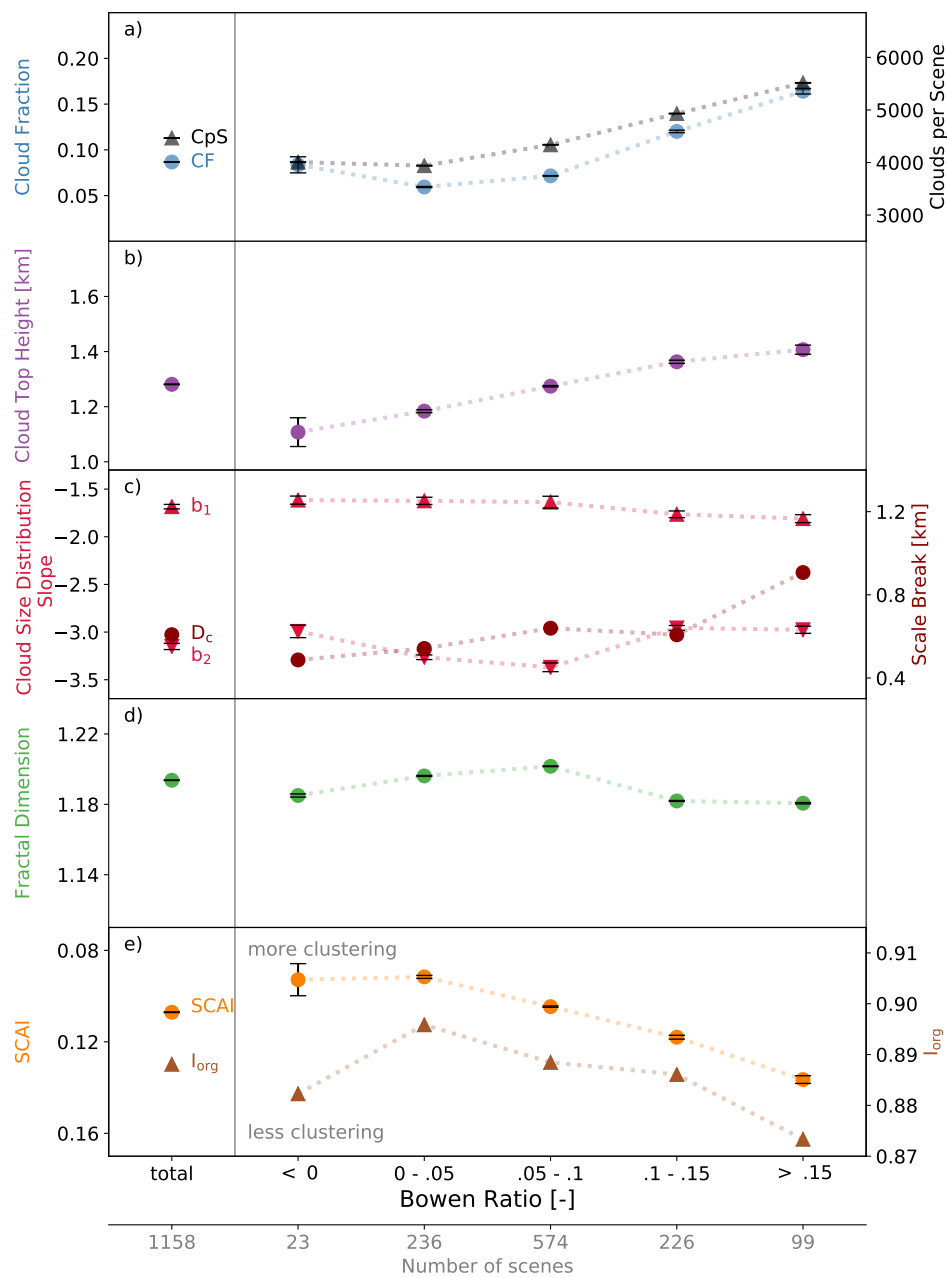


Figure A.13: Same as Figure A.6, but for Bowen ratio.

ASTER Observations													Suggested Mechanisms						
Cloud Size and Top Height		Cloud Fraction		Lower Tropospheric Stability (LTS)		Subsidence Rate		Sea Surface Temperature (SST)		Total Column Water Vapor (TCWV)		Surface Wind Speed				Wind Shear		Bowen Ratio	
<div>Initial State</div> <div>Perturbed State</div>		<div>↑ Increase</div> <div>↓ Decrease</div>																	
Increased meteorological parameter (cloud-controlling factor)				Lower Tropospheric Stability (LTS)		Subsidence Rate		Sea Surface Temperature (SST)		Total Column Water Vapor (TCWV)		Surface Wind Speed		Wind Shear		Bowen Ratio			
				Boundary layer inversion strengthens with LTS and traps moisture, leading to greater cloud fraction.		Subsidence limits cloud growth, but opposing LTS signal (increasing cloud fraction) overcompensates for the reduction in cloud fraction.		Higher SST increases surface moisture fluxes. A strong moisture gradient leads to an increased entrainment efficiency at the boundary layer inversion and to cloud thinning and lower cloud tops (entrainment liquid-flux adjustment feedback).		Increase in surface fluxes of heat, moisture, and momentum with wind speed deepens the boundary layer, enabling larger and deeper clouds.		Wind shear tilts especially the deeper clouds and increases projected cloud fraction.		The Bowen ratio controls cloud base mass flux by setting the thermodynamic efficiency of the moist convective heat cycle.					
References (only the most relevant one)		Wood and Bretherton (2006)		Myers and Norris (2013)		Bretherton and Blossey (2014), Rieck et al. (2012)		Nuijens and Stevens (2012)		Neggers et al. (2003)		Sakradzija and Hohenegger (2017)							

Figure A.14: Schematic summary of correlations between cloud field properties - cloud size, cloud top height, and cloud fraction - and large-scale meteorological parameters as observed in ASTER images. The arrows indicate the change in cloud properties with a change in the meteorological parameter from an initial (light blue) to an increased value (dark blue). Possible mechanisms are introduced in the corresponding references.

OPTICALLY THIN CLOUDS IN THE TRADES

This chapter contains a paper which is under review in *Atmospheric Chemistry and Physics* and was submitted as Mieslinger et al. (2021):

Mieslinger, T., Stevens, B., Kölling, T., Brath, M., Wirth, M., and Buehler, S. A.: Optically thin clouds in the trades, *Atmos. Chem. Phys. Discuss.* [preprint], <https://doi.org/10.5194/acp-2021-453>, in review, 2021.

CONTRIBUTIONS Together with B. Stevens I conceptualized the study and together with T. Kölling and M. Brath I developed the core of the methodology. M. Wirth generated the lidar dataset that we use in addition to the core data from the high-resolution satellite imager ASTER. S. Buehler and B. Stevens supervised the study. I conducted the analysis, and prepared the manuscript with contributions from all co-authors.

Optically thin clouds in the trades

Theresa Mieslinger^{1,2}, Bjorn Stevens³, Tobias Kölling³, Manfred Brath¹, Martin Wirth⁴, Stefan A. Buehler¹

¹ *Universität Hamburg, Faculty of Mathematics, Informatics and Natural Sciences, Department of Earth Sciences, Meteorological Institute, Hamburg, Germany*

² *International Max Planck Research School on Earth System Modelling, Hamburg, Germany*

³ *Max Planck Institute for Meteorology, Hamburg, Germany*

⁴ *Institut für Physik der Atmosphäre, Deutsches Zentrum für Luft- und Raumfahrt e.V., Wessling, Germany*

ABSTRACT

We develop a new method to describe the total cloud cover including optically thin clouds in trade wind cumulus cloud fields. Climate models as well as Large Eddy Simulations commonly underestimate the cloud cover, while estimates from observations largely disagree on the cloud cover in the trades. Currently, trade wind clouds contribute significantly to the uncertainty in climate sensitivity estimates derived from model perturbation studies. To simulate clouds well and especially how they change in a future climate we have to know how cloudy it is.

In this study we develop a method to quantify the cloud cover from a clear-sky perspective. Using well-known radiative transfer relations we retrieve the clear-sky contribution in high-resolution satellite observations of trade cumulus cloud fields during EUREC⁴A. Knowing the clear-sky part, we can investigate the remaining cloud-related contributions consisting of areas detected by common cloud masking algorithms and those undetected areas related to optically thin clouds. We find that the cloud-mask cloud cover underestimates the total cloud cover by a factor of 2. Lidar measurements on board the HALO aircraft support our findings by showing a high abundance of optically thin clouds during EUREC⁴A. Mixing the undetected optically thin clouds into the clear-sky signal can cause an underestimation of the cloud radiative effect of up to -32%. We further discuss possible artificial correlations in aerosol-cloud cover interaction studies that might arise from undetected optically thin clouds. Our analysis suggests that the known

underestimation of trade wind cloud cover and simultaneous overestimation of cloud brightness in models is even higher than assumed so far.

B.1 INTRODUCTION

Earth's trade wind regions combine a dry atmosphere and a high abundance of shallow clouds – whose tops are often not much higher than the long-wave emission height – to efficiently cool the planet. How much clouds in the trades cool the climate is quantified by their cloud radiative effect, which in a first approximation depends on the cloud cover and the average cloud reflectance. Changes in the cloud radiative effect with warming pace cloud feedbacks, which in the trades have been shown to contribute significantly to uncertainties in estimates of the global climate sensitivity (Bony and Dufresne, 2005; Vial et al., 2016), part of the well known difficulty climate models have in representing clouds and cloud changes with fidelity.

Especially in low-cloud regions such as the trades, climate models underestimate the cloud cover while overestimating its average reflectance, a problem often called the "too few, too bright" low-cloud problem (Klein et al., 2013; Nam et al., 2012). Large eddy simulation studies also show an underestimation of trade wind cumulus cloud cover and a limited representation of small clouds (Nuijens et al., 2015), while the scaling behaviour of trade cumulus clouds suggests a high abundance and significant contribution of small clouds to the total cloud cover (Mieslinger 2019; Benner and Curry, 1998; Cahalan and Joseph, 1989; Plank, 1969; Wielicki and Welch, 1986; Zhao and Di Girolamo, 2007). Studies on the "twilight" zone even suggest that clouds may extend further into the cloud-free area than assumed so far (Koren et al., 2008). To simulate the change in clouds with future temperature or aerosol perturbations, we first need to know how cloudy it is.

Estimating the cloud cover is a well-known issue in the sense that it decisively depends on the instrument used and the purpose of respective datasets. All-sky observations by trained humans might have been the first systematic cloud-cover measurements. Such measurements are synonymous with efforts to predict the weather and led to the first International Cloud Atlas as early as 1896. However, such observations are subject to unknown or hard to quantify uncertainties due to the training of the observer and further biases originating from overlapping cloud layers and undetected upper clouds, or the higher frequency of fair weather synoptic reports (Warren, Hahn, and London, 1985). Passive remote sensing opened the way to more objective quantification of cloud cover from ground, from aircraft

since the beginning of the 20th century, and also from space starting in the 1970s. Active remote sensing added additional approaches to investigate clouds from ground, aircraft, and from space. Those various instruments dedicated to observe clouds have in common the dependence of a best estimate of cloud cover on (a) the data resolution in space and / or time, (b) suitable thresholds defined in the physical quantity closest to the instrument raw data, (c) the wavelength used and the resulting sensitivity of the measurement to clouds. Even for collocated measurements with very high spatial (tens of meters) and temporal resolution, Fig. 5 in Stevens et al. (2019) and more recently Konow et al. (2021) nicely show that the range of cloud cover estimates from active and passive remote sensing can differ by a factor of 2.

In this study we present a different view on clouds by quantifying the clear-sky area. The clear-sky signal is well understood in radiative transfer relations and can be simulated with well-posed approximations. The main advantage of estimating cloudiness as the complement to clear-sky is that we overcome the problem of diverse and instrument-specific hard-coded thresholds in cloud masking algorithms. We apply the clear-sky approach to high-resolution satellite imagery from the Advanced Spaceborne Thermal Emission and Reflection Radiometer (ASTER) recorded during the field campaign EUREC⁴A in Jan-Feb 2020. EUREC⁴A was dedicated to the investigation of trade wind cumulus clouds and their interaction with the large-scale environment (Bony et al., 2017; Stevens et al., 2021). The high resolution of the ASTER data provides the possibility to include clouds of sizes at the deca- to hectometer scale and, equally important, increases the probability to observe clear-sky pixels free of any cloud structures. With the clear-sky approach we can detect enhanced reflectances from anomalously humidified aerosols and optically thin cloud areas that are undetected by traditional cloud-masking algorithms. We show the contribution of optically thin cloud areas to the total cloud area and use Lidar measurements on board the HALO research aircraft to support our findings.

The remainder of this article is organized as follows. Section B.2 describes the high-resolution ASTER satellite dataset, the WALES Lidar cloud product, and surface wind speed data based on ERA5 reanalysis. In Section B.3 we show the clear-sky model setup, and how we identify optically thin clouds in ASTER observations. Results on the contribution of optically thin clouds to the total cloud cover during EUREC⁴A are shown in Section B.4, followed by a discussion of implications of our results in Section B.5.

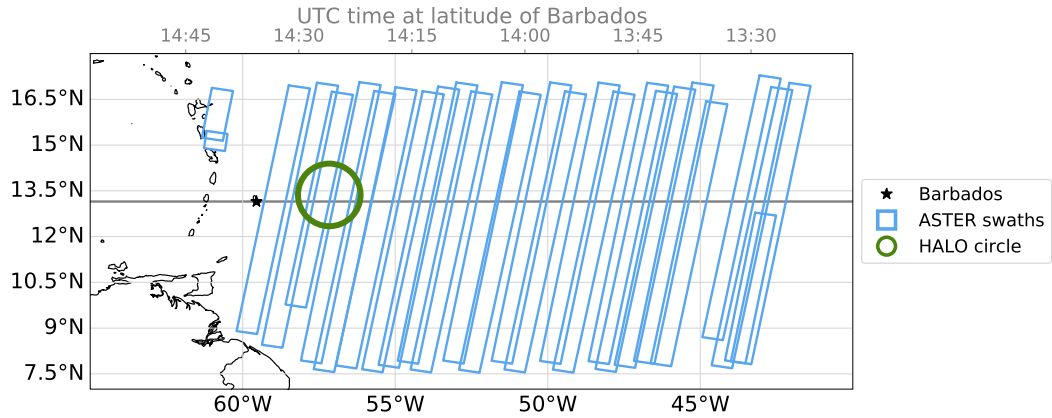


Figure B.1: ASTER dataset during EUREC⁴A with 419 images (60km x 60km) recorded on 17 days between 11 January and 19 February 2020. WALES lidar measurements are available from HALO's research flights predominantly on the circular path shown in green from 13 flight days between January 22 and February 15 2020.

B.2 OBSERVATIONS

Within this study we exploit the potential of the high spatial resolution passive remote sensing instrument ASTER (Advanced Spaceborne Thermal Emission and Reflection Radiometer; Yamaguchi et al. (1998)) that recorded images of cloud fields east of Barbados in support of the EUREC⁴A campaign. We extend the information on the typical cloud fields observed during EUREC⁴A with airborne high spectral resolution lidar measurements to support our analysis of clouds from an active sensor with a high sensitivity to small and optically thin clouds.

B.2.1 The ASTER dataset for EUREC⁴A

ASTER is mounted aboard Terra, a polar-orbiting satellite in a Sun-synchronous orbit with an equator crossing time of 10:30 local solar time. Terra crosses the latitude of Barbados and the HALO flight circle area roughly at 14:25 UTC, while the tracks further east at about 43°W are observed by ASTER an hour earlier. Fig. B.1 shows the measurements taken in the area east of Barbados from 7°N to 18°N and from 41°W to 62°W between January 11 and February 19 2020. The data from the observed swaths are segmented in the form of 60×60 km² images, each corresponding to 9 s of observation time.

ASTER's visible and near-infrared (VNIR) radiometer pointing nadir has three bands in the range of 0.53 - 0.86 μm . The radiometrically calibrated and geometrically co-registered Level 1B data provide top of atmosphere monodirectional radiances at 15 m pixel resolution at the sub satellite point. We use the band 3 radiance centered at 0.807 μm in the present study to define the total cloud cover. We further draw comparisons to the ASTER cloud mask which is based on several bands in the VNIR. The cloud mask works with thresholding tests and is representative for traditional passive remote sensing cloud masking schemes. In detail, we distinguish between *confidently clear*, *probably clear*, *probably cloudy*, and *confidently cloudy* pixels following the method described in Werner et al. (2016) for the VNIR bands. Within this study we combine the flags *probably cloudy* and *confidently cloudy* if we refer to cloudy regions according to the ASTER cloud mask. We omit thresholding tests including the broken short-wave infrared detector as well as ASTER's thermal band 14 (11.65 μm , 90 m pixel resolution). The latter would detect cirrus contaminated areas at the expense of a lower resolution.

In our analysis we work with reflectances instead of radiances with the aim to reduce the influence of varying solar zenith angles θ_0 within the overpasses and slightly varying extraterrestrial solar irradiance E_0 . The reflectance R is calculated from the radiance L as

$$R = \frac{\pi L}{\cos(\theta_0) E_0} \quad (\text{B.1})$$

B.2.2 WALES airborne lidar measurements

The WALES lidar instrument (Water Vapor Lidar Experiment in Space demonstrator; Wirth et al. (2009)) is part of the remote sensing package on board the HALO research aircraft during EUREC4A (Stevens et al., 2019). The high spectral resolution lidar measurements from the auxiliary channels of the instrument at 532 nm are well suited to investigate the small and optically thin clouds due to the high instrument sensitivity to small particles ranging from aerosols to cloud droplets. The advantage of WALES compared to space borne active instruments such as the Cloud-Aerosol Lidar with Orthogonal Polarization (CALIOP) simply lies in the closer distance and thus a higher sensitivity to low clouds and the much higher horizontal sampling due to the lower aircraft speed (0.2 km/s versus 7 km/s). The resulting horizontal spatial resolution of the WALES cloud product is about 40 m during EUREC4A, which is slightly larger but commensurate with that of ASTER. CALIOP has been shown to struggle detecting small clouds with cloud tops below

1 km (Leahy et al., 2012), while we find 29 % of clouds detected by WALES during EUREC⁴A to have cloud tops below 1 km.

Within the present study we use the cloud mask and cloud optical depth product described in Konow et al. (2021). In the dataset, a cloud is defined where the backscatter ratio exceeds 10. This threshold is lower compared to the studies by Gutleben et al. (2019) and Jacob et al. (2020) where the value was chosen to make the detection limit comparable to CALIOP. The lower value used in the present study nicely separates the highest possible signals originating from marine aerosol and any cloud related signal that might include anomalously humidified aerosols and the smallest cloud droplets. WALES uses the High Spectral Resolution Lidar technique (HSRL; Esselborn et al. (2008)) to distinguish molecular from particle backscatter at 532 nm, which allows for the direct measurement of the (two way) atmospheric transmission. The latter is proportional to the range (r) and atmospheric density corrected lidar signal $R_M(r)$. To a first approximation the optical thickness is given by

$$\tau = -\frac{1}{2} \cdot \ln \left(\frac{R_M(r)}{R_M(0)} \right). \quad (\text{B.2})$$

The complete algorithm adds several corrections and is described in detail in Esselborn et al. (2008).

B.2.3 Surface wind speed estimates

For the methodology described in Sec. B.3 we need surface wind speed estimates at 10 m height for a given ASTER pixel. The fifth generation European Centre for Medium-Range Weather Forecasts reanalysis (ERA5) provides hourly wind speed estimates on a global grid at 10 m height (2D surface product) which would fit our needs, but showed a significant underestimation compared to collocated dropsonde measurements during EUREC⁴A (JOANNE dropsonde dataset: George et al. (under review)). The underestimation is in agreement with a study by Belmonte Rivas and Stoffelen (2019) which find a low bias in ERA5 surface winds in the trades. Nevertheless, wind speed estimates from the ERA5 profile product (hourly, 0.25° grid; Hersbach et al. (2020)) agree remarkably well with dropsonde measurements.

Thus, we use ERA5 wind speeds at the lowest pressure level 1000 hPa which corresponds to about 135 m above sea level on average based on the dropsonde dataset. We derive a correction that translates from 1000hPa to 10m based on a comparison of ERA5 wind speed at 1000hPa and the 10m wind speed from

dropsonde measurements (Pearson correlation coefficient 0.88). A least squares fit provides us with the coefficients to estimate the 10 m wind speed by

$$ws = 0.92 \cdot ws_{\text{ERA5},1000\text{hPa}} + 0.40. \quad (\text{B.3})$$

This wind speed is an average value representative for a 0.25° grid cell. We therefore use measurements at the Barbados Cloud Observatory (BCO) to estimate the variance in wind speed within 0.25° compared to the 15 m ASTER grid. The BCO is located at the easternmost point of the island of Barbados and has been shown to take measurements representative of an undisturbed marine trade wind boundary layer (Stevens et al., 2016). We use the standard surface wind speed measurements from a Vaisala WXT-520 to derive an estimate of the surface wind variance within 0.25° (27.12 km at 13°N) which translates to about 80 minutes sampling period. We add a Gaussian perturbation according to the estimated wind variance of $1.63 \text{ m}^2 \text{ s}^{-2}$ to the average wind speed within our further analysis. The campaign average wind speed corresponding to the ASTER image locations is 9.02 ms^{-1} .

B.3 METHODOLOGY

The ASTER cloud mask provides us with a good perception of the certainly clear and certainly cloudy areas, while we are less confident in between. We approach the intermediate range from the clear-sky by simulating the expected probability distributions of clear-sky reflectances for a given ASTER image. Knowing the theoretical clear-sky contribution to an all-sky ASTER image we can then investigate the cloud-related contributions that are undetected by the cloud mask and which we attribute to optically thin clouds.

We start with a brief overview on the clear-sky retrieval setup and the necessary input information on surface wind speed and aerosol optical depth, before we show our approach for transferring the clear-sky information to the ASTER observations and defining areas of optically thin clouds.

B.3.1 A simplified clear-sky model (SCSM)

The clear-sky radiance over ocean in the visible range depends on a narrow set of parameters and can be estimated by simplified 1D radiative transfer calculations.

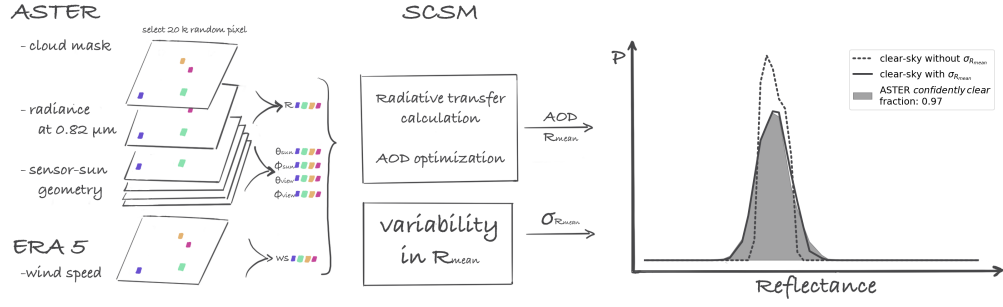


Figure B.2: Sketch illustrating the clear-sky retrieval workflow. ASTER and ERA5 input data is used to run radiative transfer simulations with integrated AOD optimization. A Gaussian perturbation is added to the output average pixel reflectance R_{mean} to account for ocean surface variability and measurement noise. The figure on the right shows the processing steps that lead to the simulated clear-sky reflectance distribution for a single ASTER image observed 2020-01-24 14:02:02 UTC.

In appendix B.7.1 we describe the full set of equations and approximations made in calculating the clear-sky signal with our simplified clear-sky model (SCSM). We generally assume a single-layer atmosphere with constant air density and calculate the extinction of solar radiance from the top of atmosphere to the ground and back to the sensor in space. How the light is reflected at the surface into the view direction of the sensor is characterized by the bi-directional reflection function which depends on the surface wind speed and the generated ocean wave slope distribution. Here, we use the wind speed estimates described in chapter B.2.3 as input to the Cox and Munk parameterization to derive an average reflectance for a given surface condition.

We further need to know the aerosol optical depth (AOD) to estimate the extinction of direct and diffuse light on its path through the atmospheric column. Although the aerosol load does not vary much within a $60 \times 60 \text{ km}^2$ ASTER image, the availability of aerosol information from measurements even for an image-average AOD is very limited. Therefore, we estimate an effective AOD in an optimization approach by including information from the ASTER dataset. We assume that the pixels labeled *confidently clear* in the ASTER cloud mask are a good first guess for clear-sky and shall serve as a reference for finding a suitable effective AOD such that the simulated clear-sky values are in close agreement with the selected ASTER pixel values.

In Fig. B.2 we illustrate the clear-sky retrieval workflow. In detail, we randomly select 20000 pixel from those defined *confidently clear* by the ASTER cloud mask

(see Sect. B.2.1) for a given ASTER image. Simulating 20000 samples ensures a proper representation of the clear-sky distribution at a manageable computational cost. For those input pixel locations we run the clear-sky model with the corresponding sensor-sun geometries, surface wind speed estimates, and a first guess on the AOD. We further optimize this image AOD value iteratively by minimizing the summed squared difference between simulated and observed reflectances. Here, we make use of scipy’s implementation of the limited-memory Broyden–Fletcher–Goldfarb–Shanno algorithm (LM-BFGS) with bounds (scipy version 1.5.2). From all evaluated ASTER images we find a campaign average effective AOD of $0.076 (\pm 0.051)$.

From comparing simulated clear-sky reflectance distributions to the observed ones for fully clear-sky ASTER observations we find two things. First, the distributions agree very well in terms of their expected value. Second, the simulated distributions are more narrow compared to the observed ones as the Cox and Munk parametrization returns average pixel reflectances R_{mean} . We therefore introduce a variability in brightness in a post processing step. We calculate a kernel density estimate with normal kernels characterized by a standard deviation $\sigma_{R_{\text{mean}}}$ that is placed on each of the simulated reflectance values (Parzen, 1962; Rosenblatt, 1956). We derive a suitable value for $\sigma_{R_{\text{mean}}}$ from comparing simulated clear-sky reflectance distributions and corresponding ASTER images that have at minimum 97% *confidently clear* pixels in the ASTER cloud mask. From 22 cases we calculate the average $\sigma_{R_{\text{mean}}} = 0.0026$ from a least-squares optimization using again the LM-BFGS algorithm. We use a constant value for $\sigma_{R_{\text{mean}}}$ for the whole dataset due to the lack of several clear-sky observations for various sensor-sun geometries. However, the ASTER dataset is confined to a narrow set of sensor-sun geometries and outside of possible sun glint observations such that we assume that a constant value is sufficient for our application.

B.3.2 Identifying optically thin clouds in all-sky observations

The output from our SCSM model provides us with a distribution of clear-sky reflectances $p(R|F_{\text{CLEAR}}, B)$, which is the probability distribution of reflectance values R given that they originate from clear-sky area with the flag $F = F_{\text{CLEAR}}$ and additional background conditions B . The background conditions include the sensor-sun geometry, wind speed, and AOD and are covered by the SCSM by handling each image individually. In the following we evaluate the probabilities on an image basis and therefore omit the implicit condition on B in the notation. Further, we use standard notation whereby “|” means “given that” for conditional probabilities and “,” means “and” and symbolizes combined (or joint) probabilities.

For example, the SCSM output is a conditional probability as the SCSM framework does not include any information on the general clear-sky fraction within one image.

In the following, we split the observed reflectance distribution of an ASTER image into the categories or flag values $F \in \{F_{\text{CLEAR}}, F_{\text{OTC}}, F_{\text{CLOUD}}\}$. The ascending order of the flag values indicates the associated expected increase in reflectance. The darkest observed pixels originate from clear-sky ocean observations. Small cloud fragments and humidified aerosols slightly enhance the reflectance, though they are often undetected by cloud masking scheme. We characterize them as optically thin clouds OTC. The flag CLOUD refers to the cloudy pixels detected by the ASTER cloud masking scheme (see Sec. B.2.1). We know the CLOUD part of an distribution $p(R, F_{\text{CLOUD}})$ from the observation and we can infer the CLEAR contribution from the SCSM output. The all-sky reflectance distribution $p(R)$ is build up by the arithmetic sum of combined probability distributions of R and the flag values F , that is:

$$\begin{aligned} p(R) &= \sum_{F_n} p(R, F_n) \\ &= p(R, F_{\text{CLEAR}}) + p(R, F_{\text{OTC}}) + p(R, F_{\text{CLOUD}}) \end{aligned} \quad (\text{B.4})$$

Each combined probability can be represented by the product of the corresponding conditional probability and the probability of the flag value, i.e. for clear-sky

$$p(R, F_{\text{CLEAR}}) = p(R|F_{\text{CLEAR}}) \cdot p(F_{\text{CLEAR}}). \quad (\text{B.5})$$

The probability of clear-sky $p(F_{\text{CLEAR}})$ is the true clear-sky fraction in an observed image and challenging to estimate. Note that the true clear-sky fraction is independent of the ASTER cloud mask. If we would know the clear-sky fraction $p(F_{\text{CLEAR}})$, equations Eq. B.5 and Eq. B.4 together fully describe the observed reflectance distribution $p(R)$. In the following we describe our approach for estimating the unknown clear-sky fraction.

The first constraint is given by the fact that any probability must be within the range $[0, 1]$, thus we can formulate for our case:

$$p(F_{\text{CLEAR}}|R'') + p(F_{\text{CLOUD}}|R'') \leq 1 \quad \forall R'' \in R \quad (\text{B.6})$$

We can approach the estimation of the clear-sky fraction $p(F_{\text{CLEAR}})$ from a conservative side by deriving the maximum possible $p(F_{\text{CLEAR}})$ such that Eq. B.6 still

holds. Thinking visually, we scale the simulated clear-sky distribution up until it touches the all-sky distribution $p(R)$. At the reflectance $R = R'$ (of unknown value) where the PDFs touch, we are certain that the non-cloudy classified reflectances are actually due to clear-sky:

$$\exists R' \text{ such that } p(F_{\text{CLEAR}}|R') = 1 - p(F_{\text{CLOUD}}|R') \quad (\text{B.7})$$

We can solve Eq. B.7 and Eq. B.6 for $p(F_{\text{CLEAR}})$ (for details see appendix B.7.2). While being mathematically concise, the described method faces a problem. It relies on the exact count of measurements in only a single reflectance bin R' and thus is especially susceptible to measurement and model uncertainties. We tackle this problem by extending and relaxing the condition stated in Eq. B.7. We modify this first condition from a single value to an extended range of reflectance values. As Eq. B.7 would be overdetermined for more than one reflectance value in the presence of measurement and model uncertainties, we demand that the equation approximates the value $1 - p(F_{\text{CLOUD}}|R')$ for reflectivity values measured and known to be caused by clear-sky.

In particular, we do this by a weighted linear regression, minimizing the term:

$$\int |p(F_{\text{CLEAR}}|R) - (1 - p(F_{\text{CLOUD}}|R))| \cdot w^2 dR \quad (\text{B.8})$$

with $p(F_{\text{CLEAR}})$ as the only free variable. The regression weight $w = p(R)p(R|F_{\text{CLEAR}})$ is chosen to only consider measured reflectances $p(R)$ that overlap with the range of simulated clear-sky reflectances $p(R|F_{\text{CLEAR}})$. The product of both guarantees a close agreement around the peaks of measured and simulated PDF.

The resulting estimate of $p(F_{\text{CLEAR}})$ is more robust in the presence of small measurement or model errors, but a direct consequence of this approximate matching is that Eq. B.6 does not necessarily hold for all R'' anymore. As illustrated in Fig. B.3 using dotted and dashed lines, we correct this by clipping the resulting probabilities to the allowed range. As this clipping effectively modifies the simulated reflectance distribution and thus is potentially dangerous, we need to ensure that this method indeed only compensates for small measurement uncertainties (i.e. in the order of a single digital sensor count). We can do this by comparing the expected value of the clear sky reflectance $p(R|F_{\text{CLEAR}})$ before and after clipping. On average, this difference is 0.15 % and even in the worst (maximum) case, the clipping causes a shift of 0.0018 in reflectance units, which is well below one digital sensor count of about 0.004 reflectance units. Based on this analysis, we use the more stable regression and clipping method in stead of a direct application of Eq. B.7.

Further, the SCSM does not include cloud shadows on the ocean surface which introduce a signal at very low reflectances in the observed distribution. Conceptu-

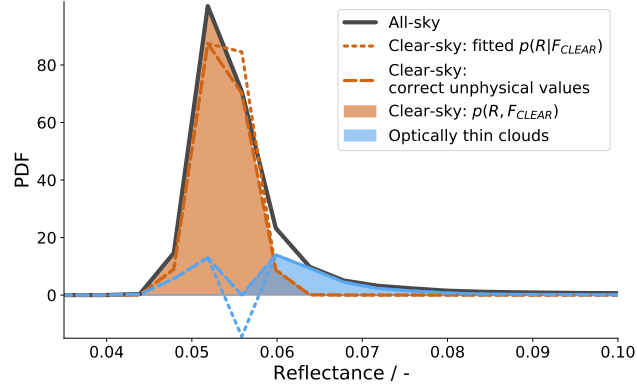


Figure B.3: Visualization of the approach for estimating the clear-sky fraction $p(F_{\text{CLEAR}})$ by optimization. The orange dotted and dashed lines show the processing steps leading to the filled orange clear-sky PDF. The blue lines are the respective residuals related to optically thin clouds and resulting from the all-sky (grey) minus the CLEAR (orange) and minus the CLOUD PDF (dark blue; not visible).

ally we add the low reflectance values originating from such shadowed areas to the clear-sky reflectance distribution $p(R, F_{\text{CLEAR}})$.

In Fig. B.4 we show combined probability distributions per flag for an ASTER observation on the 31st of January east of Barbados. The inset figure shows the reflectance image that we translate into the distribution using the method described above.

B.3.3 Robustness of optically thin cloud estimation

Our target variables are the fraction and expected reflectance of optically thin clouds. The retrieval of clear-sky and subsequent optically thin clouds in ASTER images depends on visible clear-sky areas which limits the evaluation of the full ASTER EUREC⁴A dataset to images with less than 85 % detected cloud cover in the cloud masking algorithm (395 images).

Within the retrieval we have two main free parameters which can introduce uncertainty in our target values, the surface wind speed estimate and the assumed variability $\sigma_{R_{\text{mean}}}$ of simulated average pixel reflectances R_{mean} . We first have a look at the added variability. From a comparison of 22 manually checked clear-sky reflectance distributions (> 97 % *confidently clear* pixels) to the simulated distributions we derived an average variance of 0.0026 (± 0.0007). We apply the methodology described in this section for the average value, as well as for a 20 %

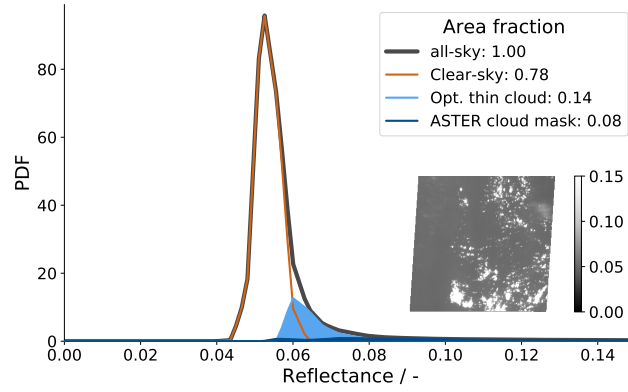


Figure B.4: Reflectance distribution corresponding to the ASTER observation shown in the inset figure recorded on 31 January 2020, 14:08:05 UTC south-east of the HALO circle area at 11.37°N , 53.86°W . The clear-sky contribution is retrieved with the method (1) described in section B.3.2 and displayed by the orange curve, while pixel reflectances identified cloudy from the ASTER cloud masking algorithm are shown in dark blue. We attribute light blue contribution to the distribution to optically thin clouds.

lower (0.0020) and 20 % higher value (0.0031). Similarly, we add an artificial bias of $\pm 20\%$ to the surface wind speed estimates and investigate the change in our target values. The average wind speed in our dataset is 9.02 ms^{-1} ($\pm 2.38 \text{ ms}^{-1}$). The resulting deviations in our target values, the fraction $p(\text{OTC})$ and expected reflectance $E(R|\text{OTC})$ of optically thin clouds, that result from a bias in $\sigma_{R_{\text{mean}}}$ and / or the surface wind speed are stated in Tab. B.1 and Tab. B.2.

The fraction of optically thin clouds $p(\text{OTC})$ changes only slightly with a change in wind speed showing an overestimation for a negative wind speed bias meaning that a small part of the clear-sky distribution is wrongly attributed to optically thin clouds. For a positive wind speed bias the opposite is the case. The low uncertainties (3.1 % and -2.5 %) are a result of the retrieval setup including the optimization of AOD which can partly compensate a bias in wind speed. Changing the variability of simulated average pixel reflectances $\sigma_{R_{\text{mean}}}$ can narrow (negative bias in $\sigma_{R_{\text{mean}}}$) and broaden (positive bias in $\sigma_{R_{\text{mean}}}$) the clear-sky distribution and thus lead to strong over- or underestimation of $p(\text{OTC})$ as high as $\sim 10\%$. Combining the highest retrieval uncertainties from the two free parameters, the wind speed and the variability $\sigma_{R_{\text{mean}}}$, we can get a deviation in the estimated fraction of optically thin clouds of ± 0.026 ($\pm 14.2\%$).

The expected reflectance of optically thin clouds $E(R|\text{OTC})$ shows a smaller sensitivity to changes in the wind conditions and $\sigma_{R_{\text{mean}}}$ compared to the fraction of optically thin clouds discussed above. An underestimation in wind speed leads to a

Table B.1: Deviations of the fraction of optically thin clouds $\Delta p(\text{OTC})$ for the two main free parameters to the clear-sky retrieval, the surface wind speed and the variability $\sigma_{R_{\text{mean}}}$. The two numbers in each cell state the absolute / relative difference to the reference case with no wind speed bias and $\sigma_{R_{\text{mean}}} = 0.0026$ respectively.

		wind speed bias		
		-1.8 ms ⁻¹	0 ms ⁻¹	1.8 ms ⁻¹
$\sigma_{R_{\text{mean}}}$	0.0020	0.026 / 14.2%	0.018 / 10.1%	0.012 / 6.3%
	0.0026	0.006 / 3.1%	0 / 0%	-0.005 / -2.5%
	0.0031	-0.012 / -6.4%	-0.019 / -10.0%	-0.022 / -11.9%

Table B.2: Deviations of the expected reflectance of optically thin clouds $\Delta E(R|\text{OTC})$ for the two main free parameters to the clear-sky retrieval, the surface wind speed and the variability $\sigma_{R_{\text{mean}}}$. The two numbers in each cell state the absolute / relative difference to the reference case with no wind speed bias and $\sigma_{R_{\text{mean}}} = 0.0026$ respectively.

		wind speed bias		
		-1.8 ms ⁻¹	0 ms ⁻¹	1.8 ms ⁻¹
$\sigma_{R_{\text{mean}}}$	0.0020	-0.0043 / -4.4%	-0.0031 / -3.1%	-0.0017 / -1.8%
	0.0026	-0.0011 / -1.1%	0 / 0%	0.0014 / 1.4%
	0.0031	0.0024 / 2.5%	0.0038 / 3.9%	0.0049 / 5.0%

marginal underestimation in the expected reflectance as lower clear-sky reflectances are wrongly attributed to optically thin clouds. In the case of an overestimation in wind speed, the clear-sky reflectance distribution extends to higher reflectance values which are missing in the estimated $E(R|\text{OTC})$ and thus leads to a high bias in $E(R|\text{OTC})$. A more narrow (negative bias in $\sigma_{R_{\text{mean}}}$) or broader (positive bias in $\sigma_{R_{\text{mean}}}$) clear-sky distribution can decrease or increase the expected reflectance of optically thin clouds up to $\pm 4\%$. However, the combined deviation due to possible biases in wind speed and $\sigma_{R_{\text{mean}}}$ are still within the range of ± 0.0049 ($\pm 5.0\%$).

B.4 RESULTS

We investigate 395 ASTER images for the signal from optically thin clouds (OTC) that are undetected by the ASTER cloud mask but can be identified with the method described in Sect. B.3. We first visualize pixels in an image that we attribute to the total cloud cover including OTC pixels and those detected in the ASTER cloud mask. We then define a close match of OTC reflectances in ASTER images and the signal of OTC detectable in WALES lidar data. WALES measurements provide an independent view of the results of the cloud cover by OTC from a different instrument technology and complement our analysis based on ASTER images. Finally, we show the significant contribution of optically thin clouds to the total cloud cover.

B.4.1 Visualizing optically thin clouds in an ASTER image

To visualize the OTC area in an image we can define a threshold in reflectance similar to common cloud masking algorithms. We construct a total cloud cover mask that includes pixels with a probability of that pixel reflectance to be cloudy $p(F_{\text{TOTAL_CLOUD}} | R = R_{\text{pixel}}) \geq 0.9$ with $F_{\text{TOTAL_CLOUD}} = F_{\text{OTC}} \vee F_{\text{CLOUD}}$. In the particular ASTER image shown partially in Fig. B.5 all reflectance values greater than 0.049 satisfy that condition. The cloud mask derived with the cloud masking algorithm by including several ASTER bands is shown in blue in panel a) while the total cloud cover mask is shown by the contours in red in panel b). The background reflectance image in panel b) is adjusted in its reflectance range with the aim to enhance the range reflectances related to OTC.

The figure visualizes how OTC is often classified in pixels surrounding detected clouds. Detraining clouds and anomalously humidified aerosols likely cause enhanced reflectances close to thicker clouds. Possible scattering of light at the sides of thicker clouds might additionally enhance the brightness of their surrounding areas. Such surrounding halos of optically thin clouds lead to (threshold dependent) smoother cloud edges, an interesting result in the context of cloud boundaries and related fractal dimensions. Also, cloud structures tend to be more connected in the total cloud cover mask leading to larger cloud objects with smooth reflectance transitions to the clear-sky ocean background. While there are numerous studies on cloud shapes we rather focus on a statistical estimate of area coverage and the contribution of OTC to the total cloud cover in the remainder of this work.

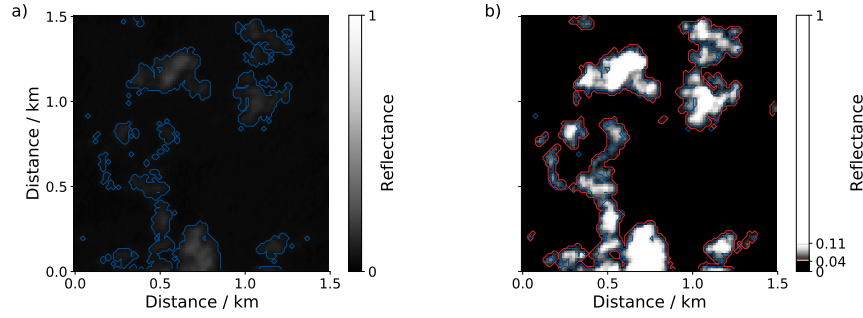


Figure B.5: Visualization of the area corresponding to optically thin clouds. Shown are reflectances at $0.807 \mu\text{m}$ for a $1.5 \times 1.5 \text{ km}^2$ selection of an ASTER image recorded on 5 February 2020, 14:25:15 UTC. (a) shows the full physical range of reflectance values ranging from 0 to 1 with overlaid blue contours outlining the ASTER cloud mask. (b) is similar to (a) but with the color scale limited to the 10th and 90th percentile of reflectances attributed to total cloud cover including optically thin clouds. The red contours correspond to $p(F_{\text{TOTAL_CLOUD}}|R = R_{\text{pixel}}) \geq 0.9$.

B.4.2 The OTC equivalence in Lidar data

In Fig. B.5 optically thin clouds are barely visible in the reflectance field in panel a) suggesting that those clouds have a very low cloud optical thickness. Due to non-linearities in the physical and radiative properties of small cumulus clouds and the large influence of 3D radiative effects, plane-parallel retrieval of microphysical properties do not work reliably and we cannot derive cloud optical thickness from ASTER measurements directly (Davies, 1978; Kölling, 2020; Loeb, Várnai, and Davies, 1997; Marshak et al., 2006; Stevens et al., 2019; Várnai and Marshak, 2003). However, we use the theoretical relationships that plane-parallel retrievals are based on to estimate an effective cloud optical thickness that could be detected by ASTER against the ocean surface background following the two-stream approximation by Lacis and Hansen (1974):

$$A = \frac{\sqrt{3}(1-g)\tau}{2 + \sqrt{3}(1-g)\tau} \approx \frac{\tau}{\tau + 7.7} \quad (\text{B.9})$$

with the cloud albedo A , cloud optical thickness τ and the asymmetry parameter $g = 0.85$. In Fig. B.6 we show the relationship stated in Equ. B.9 of a plane-parallel cloud (black line) and add uncertainties from cloud 3D effects and the background ocean signal.

The average ocean reflectance during EUREC⁴A was 0.04 including single cases as high as 0.07. Due to additional variability in the ocean wave reflection we expect that clouds with an albedo below 0.1 and corresponding cloud optical thickness

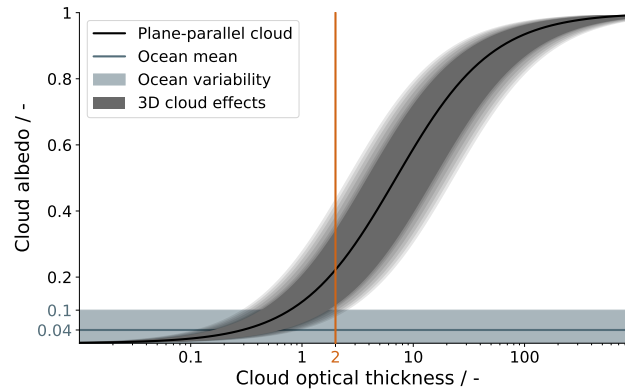


Figure B.6: Plane-parallel relationship between cloud albedo and cloud optical thickness following Lacis and Hansen (1974). The ocean reflectance is estimated from the ASTER observations during EUREC4A, while the uncertainty due to 3D radiative effects is a rough estimate from the literature.

below 1 to dissolve in the ocean signal. For clouds with cloud optical thickness larger than 1, 3D effects such as brightening and shadowing as well as photon loss through the cloud sides become relevant and can easily cause a factor of 2 error in the reflectance (Marshak et al., 2006; Stevens et al., 2019). We therefore assume that due to natural variability in the background ocean signal and the cloud signal, clouds with optical thickness below 2 do not stand out clearly from the ocean and the ASTER cloud mask presumably is insensitive to such optically thin clouds.

Clouds with an optical thickness below 2 are thin enough for a lidar beam to penetrate through the cloud and provide a reliable estimate of the cloud optical thickness. We can therefore make use of WALES lidar measurements for supporting information on the abundance of optically thin clouds.

Fig. B.7 shows the distribution of cloud optical thickness measurements from WALES for days with local research flights. The peak at low cloud optical thickness values corresponds to optically thin clouds that the lidar beam manages to penetrate. A cloud with optical thickness of about 2.5 reduces the lidar signal below the cloud to more than one hundredth and the method to derive the optical thickness still works. At night the range of retrieved optical thickness increases to about 3.5 due to a better signal to noise ratio above clouds without scattered sun light. In thicker clouds the signal vanishes in the system noise. We aggregate all measurements from optically opaque and thick clouds in one bin as we have no information on the actual cloud optical thickness.

In WALES measurements we associate optically thin clouds to have an optical thickness below 2. The campaign average cloud optical thickness of OTC is 0.75, the

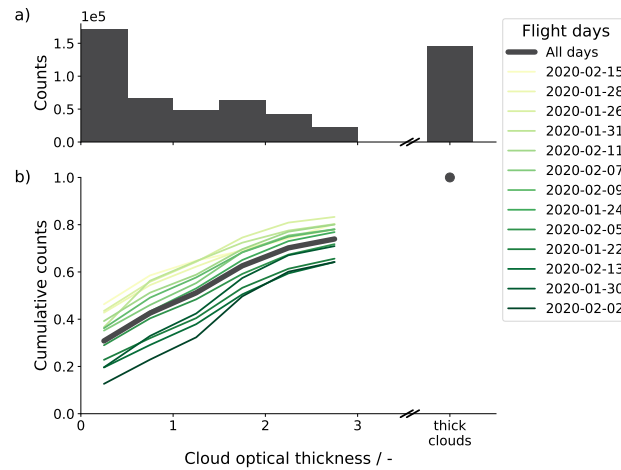


Figure B.7: Cloud optical thickness distribution from WALES lidar measurements for all days with local research flights during EUREC⁴A resulting in 92 hours of data. Panel a) shows the frequency distribution of all days, while panel b) additionally shows the cumulative distributions for individual days. The days are sorted by their increasing average cloud optical thickness that we associate with optically thin clouds (yellow to dark green). The split x-axis visualizes the limited information on thick clouds that are optically opaque to the lidar.

median is 0.52. Optically thin clouds have on average a cloud top height at 1.5 km altitude (median 1.2 km). We further use the WALES measurements to derive a fractional cloud cover in time for optically thin clouds and compare the results to the optically thin cloud cover from ASTER in the following section.

B.4.3 The contribution of OTC to the total cloud cover

From analysing 395 ASTER images during EUREC⁴A we find an average total cloud cover of 42 %, combined of 24 % from detected clouds and 19 % from optically thin clouds (see Tab. B.3). Based on the clear-sky retrieval uncertainties derived in Sec. B.3.3 we estimate the uncertainty in ASTER optically thin cloud cover to be within the range of ± 2.6 %. In Table B.3 we state the respective numbers derived from WALES measurements. We explicitly note that a direct comparison is not reasonable as the two instruments and approaches show optically thin cloud areas from two different perspectives. However, what we can say is that WALES lidar measurements indicate a high fractional coverage by optically thin clouds, similar to what we find from ASTER images.

Table B.3: Cloud cover estimates during EUREC⁴A from 395 ASTER satellite observations ($60 \times 60 \text{ km}^2$) at 15 m resolution on 17 days and from WALES lidar measurements recoded within 13 research flights (days) at about 40 m resolution in January and February 2020.

	Optically thin cloud cover / %	Total cloud cover / %
ASTER (mean)	19	42
ASTER (median)	19	36
WALES (mean)	21	34

In Sec. B.4.1 we mentioned the possible influence of scattering at cloud edges which can illuminate areas surrounding thicker clouds. Such 3D effects would influence our results based on ASTER data and lead to an overestimation of OTC related cloud cover. As WALES is less affected by the 3D scattering at cloud edges but shows a higher fraction of optically thin clouds relative to ASTER, the ASTER analysis does not seem to be unduly influenced by 3D radiative effects.

Our results based on ASTER and WALES measurements are lower compared to an analysis of optically thin marine clouds from CALIOP measurements by Leahy et al. (2012). From two years of nighttime measurements the authors attribute 45 % of total cloud cover to optically thin clouds between 60°S and 60°N , while in the trades the fraction of optically thin clouds is as high as 84 %. From WALES measurements we derived an OTC fraction of 63 % for cloudy profiles with cloud optical thickness < 2 . If we include clouds with cloud optical thickness up to about 3 as it is done in the study by Leahy et al. (2012), the OTC fraction in WALES data increases to 74 %. Estimates based on CALIOP data are likely to overestimate the OTC fraction due to the lower sensor resolution of 90 m footprints every 335 m. The authors in Leahy et al. (2012) derive a possible overestimation of OTC fraction of up to 25 % in the trades due to partially cloudy CALIOP footprints, which supports our findings in the current study of a lower, but still significant contribution of optically thin clouds to the total cloud cover.

We further notice that the area covered by optically thin clouds increases with detected cloud cover for low total cloud cover as shown in Fig. B.8 and similarly stated in Leahy et al. (2012). The positive correlation up to 0.4 total cloud cover might be due to a combination of two features. First, optically thin cloud areas are often found surrounding detected clouds (see also Fig. B.5). This idea is supported in a study by Koren et al. (2007), which find enhanced reflectances in solar irradiance

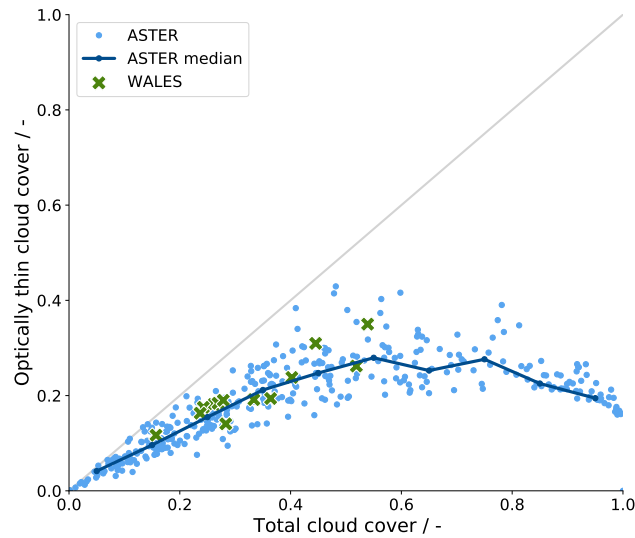


Figure B.8: Change in optically thin cloud cover with total cloud cover. The blue markers correspond to values derived from 395 ASTER images ($60 \times 60 \text{ m}^2$) with the dark blue line following along the median values. The green markers correspond to daily-averaged cloud cover estimates from WALES lidar measurements. The grey diagonal line shows the maximum possible contribution of optically thin clouds to the total cloud cover.

measurements before and after an identified cloud originating from humidified aerosols and/or unresolved cloud fragments.

The second ingredient to the proposed positive correlation is the cloud field structure. Trade wind cumulus cloud fields at low cloud cover typically correspond to *sugar* or *gravel* type structures as described by Stevens et al. (2020), consisting of many small clouds with enough space in between that can be partly filled with undetected optically thin clouds. More clouds and more cloud boundary therefore leads to more optically thin cloud area up to a point where this relationship saturates at about 0.4 total cloud cover. The saturation might be due to larger clouds or cloud structures being surrounded by pronounced clear-sky regions. A recent study by Schulz, Eastman, and Stevens (2021) identifies the so-called *flower* and *fish* cloud patterns of having characteristic clear-sky areas between clouds. By constraint, the positive correlation turns negative above 0.7 total cloud cover as the clear-sky, OTC, and detected cloud cover always add up to 1 and high cloud-mask cloud cover situations leave little space for optically thin clouds.

We conclude that optically thin clouds cover large parts of the trades leading to a higher total cloud cover than assumed so far from passive satellite observations.

B.4.4 The cloud reflectance - cloud cover relationship in ASTER observations

Current climate models typically have a narrow range of cloud optical thickness that might affect model perturbation experiments due to the non-linearity of cloud optical thickness and its albedo. Especially in low-cloud regions such as the trades, climate models underestimate the cloud cover while overestimating its average reflectance, a problem often called the "too few, too bright" low-cloud problem (Klein et al., 2013; Nam et al., 2012). While observations show a positive correlation of cloud cover and cloud reflectance, models show a reverse sign (Konsta et al., 2016).

We investigate the cloud cover - cloud reflectance relationship in Fig. B.9 and Fig. B.10. Fig. B.9 panel a) shows in blue curves the change in all-sky reflectance distribution with increasing cloud cover as defined by the ASTER cloud mask, while the red lines show similarly the change with increasing total cloud cover. We show two representative cloud cover ranges, a low range from 0.1 to 0.3 and a high range from 0.5 to 0.7. With increasing cloud cover, the reflectance distributions shift to higher values meaning that the overall image is brighter. As expected, the total cloud cover reflectance distributions peak at lower reflectances compared to their cloud-mask counterparts meaning that the total cloud cover area is less bright on average.

Panel b) shows an interesting new facet to the difference in total and cloud-mask cloudy areas. The distributions show how the total cloud reflectance relative to the total cloud area in the image depends on cloud cover. The comparison of low and high cloud cover cases reveals that clouds are brighter with increasing cloud cover, which is in agreement with our perception of larger, deeper, and brighter clouds being present in high cloud cover situations. The change in cloud brightness with cloud cover is less pronounced if the total cloud cover is considered (including optically thin clouds) compared to the cloud-mask only case.

We further investigate the expected cloud reflectances in relation to derived cloud cover values for all 395 ASTER images in Fig. B.10. Both, cloud mask and total cloud cover, exhibit positive correlations with respective cloud reflectance values in agreement with findings in Konsta et al. (2016). We here derive a campaign average cloud reflectance from total cloud cover of 0.15, with contributions from cloud-mask clouds (avg: 0.21) and optically thin clouds (avg: 0.10), which agrees quite well with an average trade wind cumulus cloud reflectance of 0.15 derived from a combination of POLDER (Polarization and Directionality of the Earth's Reflectances) and CALIOP measurements in the study by Konsta et al. (2016). Based on the clear-sky retrieval uncertainty stated in Sec. B.3.3, the uncertainty

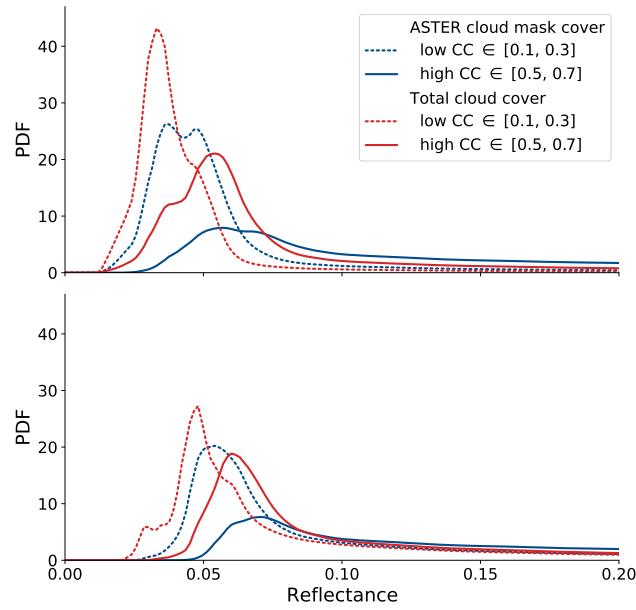


Figure B.9: Combined probability density functions (PDF)s of a) all-sky reflectances from ASTER $p(R|CC)$, binned according to the total (red) and cloud mask (blue) cloud cover (CC). We define two representative cloud cover ranges, low CC (0.1 to 0.3) and high CC (0.5 to 0.7). Panel b) shows the conditional probability of total cloud reflectances $p(R|F_{TOTAL}, CC)$, given that they are within the range of low or high CC. Compared to a), the distributions in panel b) do not include the clear-sky contributions at low reflectances.

in expected reflectance of optically thin clouds is as low as 0.005 and does not influence our results and conclusions drawn here.

The positive correlation in Fig. B.10 for total cloud cover agrees well with the corresponding Fig. 6a in Konsta et al. (2016). As mentioned before, climate models show a reverse sign of this correlation together with a general underestimation of cloud cover and simultaneous overestimation of cloud reflectance. Next to the model intrinsic mechanisms leading to too few, but too bright clouds, biases might be partially due to tuning the model based on traditional cloud masks that overestimate the cloud reflectance especially in the frequent low cloud cover situations.

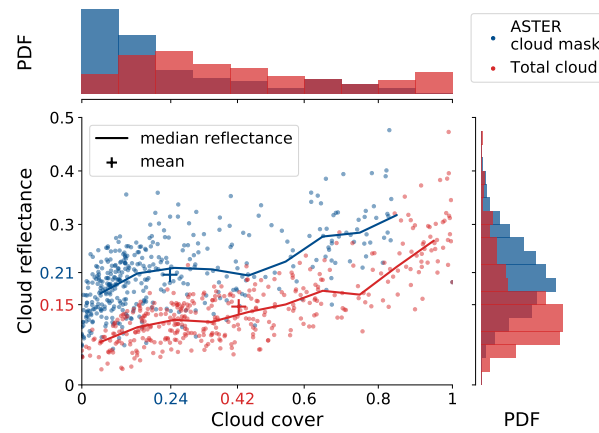


Figure B.10: Expected cloud reflectance corresponding to the ASTER cloud mask (blue) and the derived total cloud cover (red) from 395 ASTER images. The median cloud reflectances are given by the lines and the dataset averages are visualized by the “+” marker and the respectively colored tick labels. The frequency distributions of cloud cover and cloud reflectance are shown in the panels on the top and right respectively.

B.5 DISCUSSION

Most passive satellite imagers operate at resolutions in the order of hectometer to kilometer range and derive cloud products at 1 km scale or coarser. Undetected optically thin clouds, as well as small clouds detected at the ASTER 15 m scale, are unresolved and lead to partially cloudy pixel measurements. Several studies in the past have investigated the resolution effect in trade cumulus cloud cover estimated from passive satellite imagers. Zhao and Di Girolamo (2006) find a three- to fivefold overestimation of cloud cover in MODIS and MISR images respectively compared to ASTER observations during the RICO campaign. For the same dataset, a study by Dey, Di Girolamo, and Zhao (2008) suggests a fourfold overestimation of cloud cover if the ASTER cloud mask is degraded from 15 m to 1 km while cloud detection thresholds are kept constant. However, degrading the resolution can also lead to an underestimation of cloud cover estimates in cloud masking schemes if the resulting pixel radiances fall below fixed radiance thresholds. In an early study by Wielicki and Parker (1992) the authors estimate that roughly one third of the cloud cover detected in 30 m Landsat images showing cumulus clouds would not be detected by certain cloud masking schemes, which is in line with our study results.

An underestimation of cloud cover due to undetected optically thin clouds and an overestimation due to an reduced spatial resolution have compensating tendencies. However, one effect that does not cancel out in typical passive satellite cloud products is the influence of optically thin clouds in partially cloudy pixels that are classified to be clear. Pure clear-sky observations are crucial for aerosol retrievals, as well as cloud radiative effect (CRE) estimates. With decreasing sensor resolution the probability for clear-sky observations decreases as well. We therefore investigate implications that undetected optically thin clouds can have on CRE estimates, as well as our inferences on cloud-aerosol interactions in the trades, despite their low cloud albedo.

B.5.1 Implication for CRE estimates

In temperature perturbation studies, cloud feedback defines how clouds adjust to a perturbation in surface temperature and whether this change amplifies or dampens the initial temperature perturbation. As such, it is tied to the cloud radiative effect (CRE), the difference in all-sky and clear-sky radiative flux at the top of the atmosphere, in the initial as well as in the perturbed climate.

$$\text{CRE} = F_{\text{ALL}} - F_{\text{CLEAR}} \quad (\text{B.10})$$

In the trades, climate models show a less negative CRE in response to warming, indicative of a positive cloud feedback (Zelinka et al., 2020). Observational constraints based on satellite data at coarse resolution might be insensitive to sub-pixel scale clouds and consequently lack a robust clear-sky signal. From our analysis we can estimate an upper bound on the error in CRE that might arise from a clear-sky signal that is contaminated by undetected optically thin clouds.

If we assume that the pixel reflectances corresponding to optically thin clouds from the present analysis are fully mixed into the clear-sky signal, we would overestimate the clear-sky reflectance and consequently underestimate the CRE. We derive a relative bias ΔCRE per image from the differences in all-sky L_{ALL} , clear-sky L_{CLEAR} , and "contaminated" clear-sky $L_{\text{CLEAR+OTC}}$ expected radiance values:

$$\Delta\text{CRE} = \frac{\text{CRE}_{\text{CLEAR+OTC}} - \text{CRE}_{\text{CLEAR}}}{\text{CRE}_{\text{CLEAR}}} \quad (\text{B.11})$$

$$= \frac{L_{\text{ALL}} - L_{\text{CLEAR+OTC}}}{L_{\text{ALL}} - L_{\text{CLEAR}}} - 1 \quad (\text{B.12})$$

Note that we use here the simulated clear-sky L_{CLEAR} radiances as those do not contain the low radiances from cloud shadows on the ocean surface which would cause a slight underestimation of the clear-sky radiance.

In principle, a mono-directional radiance L can be converted to a radiative flux F as it is done by Clouds and the Earth's Radiant Energy System (CERES) radiative flux products by the following equation (Loeb et al., 2003; Su et al., 2015):

$$F = \frac{\pi L(\theta_s, \theta_v, \Phi)}{f(\theta_s, \theta_v, \Phi)} \quad (\text{B.13})$$

with the sun θ_s and sensor view θ_v zenith angles, the azimuthal difference Φ and the anisotropic factor f . The anisotropic factor is challenging to estimate and no suitable values are available for ASTER observations. However, if we assume isotropic scattering of cumulus cloud fields ($f = 1$) we can translate the CRE bias into an effective radiative flux at $0.807 \mu\text{m}$.

The mean CRE bias from the ASTER dataset is as high as -32 % which roughly translates to about -6 Wm^{-2} . The order of magnitude of the potential CRE bias from optically thin clouds is comparable to the magnitude of the aerosol direct effect that has been estimated to be about 5 Wm^{-2} for the winter trades in Loeb and Manalo-Smith (2005) highlighting the importance of an improved representation of optically thin clouds in future studies.

B.5.2 Optically thin clouds in the aerosol-cloud interaction context

First, we would like to point out the difference between optically thin clouds and aerosols. The marine boundary layer is a humid layer with the constant presence of humidified sea-salt and ammonium sulfate aerosols. The mixing within the boundary layer will bring the aerosols almost always into an environment above 80 % relative humidity such that sea-salt and ammonium sulfate deliquesce, while the humidity is almost everywhere above 60 % making it impossible for the aerosols to effloresce (humidity as shown by the JOANNE dropsonde dataset, George et al. (under review)). Thus, humidified aerosols are omnipresent and part of the clear-sky signal. As both, ASTER and WALES data suggest a total cloud cover well below 100 % (insensitive to the exact cloud threshold in WALES) we are confident that the described signal of optically thin clouds can only be due to anomalously humidified aerosols and cloud droplets.

Aerosol-cloud interaction studies are a topic in itself and we will not go into great detail, but rather want to show where optically thin clouds might need to be

considered in these studies. One largely debated issue is the positive correlation of AOD and cloud cover as an indirect aerosol effect. The underlying principle is that hydrophilic aerosols can serve as cloud condensation nuclei and increase the cloud droplet number concentration. More aerosols might therefore reduce the precipitation formation rate and increase the cloud liquid water content and cloud lifetime (Albrecht, 1989). Whether this so-called cloud lifetime effect actually leads to increased cloud cover is largely debated (Gryspeerd, Quaas, and Bellouin, 2016; Kaufman et al., 2005; Loeb and Manalo-Smith, 2005; Stevens and Feingold, 2009).

While modeling studies suggest negligible or equally small enhancing or decreasing influences of aerosols on the cloud cover (Quaas et al., 2008; Seifert et al., 2015; Xue and Feingold, 2006), observational studies mostly rely on coarse satellite observations and show deficiencies in the accuracy in aerosol and cloud retrievals as discussed in Quaas et al. (2020). The positive correlation in optically thin cloud cover and detected clouds in the current study suggests that part of the proposed sensitivity of cloud cover to AOD might reflect a high bias in clear-sky estimates that is interpreted as high AOD. In agreement with our perception, an observational study by Gryspeerd, Quaas, and Bellouin (2016) estimates meteorological covariances to account for 80 % of the often proposed AOD-cloud cover relationship with the additional note on shallow cumulus regions having a very weak relationship.

Independent of the cloud-lifetime effect, a positive perturbation in aerosols increases the cloud droplet number concentration and thus the cloud brightness, which is commonly referred to as the Twomey effect (Quaas et al., 2020; Twomey, 1959). Increasing the brightness also increases the probability of undetected and optically thin clouds identified in the current study to cross the detection threshold of common cloud masking schemes. We therefore speculate that the Twomey effect indirectly leads to positive AOD-cloud cover relationships found in previous studies. It might be interesting to investigate the AOD-cloud cover relationship based on a more comprehensive definition of total cloud cover including optically thin clouds.

B.6 CONCLUSIONS

Climate models as well as Large Eddy Simulations commonly underestimate the cloud cover, while estimates from observations largely disagree on the cloud cover in the trades. We use a new method to estimate the total cloud cover from the clear-sky perspective by simulating the clear-sky contribution to an observed all-sky reflectance distribution with a simplified radiative transfer model. The present

study shows the high abundance of optically thin clouds in the trade wind region that are undetected by common cloud-masking schemes.

We analyzed 395 ASTER satellite images recorded in support of the EUREC⁴A field campaign in January and February 2020 and find that about half of the total cloud cover is due to undetected optically thin clouds. A comparison to independent WALES lidar measurements supports our findings.

We find that pixels attributed to optically thin clouds are often found surrounding brighter cloud objects that can be detected in cloud-masking schemes. Accounting for optically thin clouds significantly ($29\pm 2\%$) reduces the average cloud reflectance as optically thin clouds are systematically less reflective than clouds detected in cloud masking schemes. Our analysis suggests that the known underestimation of trade wind cloud cover and simultaneous overestimation of cloud brightness in models is even higher than assumed so far.

We identify two implications from our study. First, if mixed into the clear-sky signal, the enhanced radiance from optically thin cloud areas leads to a high bias in clear-sky estimates over ocean and hence a low bias up to -32 % in the estimated cloud radiative effect of trade wind cumulus cloud fields.

And second, the positive correlation in optically thin cloud cover and detected clouds for low cloud cover suggests that part of the sensitivity of cloud cover to AOD found in aerosol-cloud interaction studies might reflect a high bias in clear-sky estimates that is interpreted as high AOD. In addition, increasing cloud brightness with higher AOD likely increases the probability of undetected and optically thin clouds identified in the current study to cross the detection threshold of common cloud masking schemes. These effects could contribute to an unrealistically strong relationship between satellite retrieved values of AOD and cloud cover, and would suggest that not accounting for optically thin clouds could overstate the strength of aerosol cloud interactions.

CODE AND DATA AVAILABILITY In addition to the publicly available ASTER L1B data from NASA we provide processed data for the ASTER images recorded during EUREC⁴A and displayed in Fig. B.1. NetCDF files containing physical quantities from bands in the VNIR and thermal range, latitude and longitude information, a cloud mask, and cloud top height estimates are available on the AERIS data server (<https://observations.ipsl.fr/aeris/eurec4a-data/SATELLITES/TERRA/ASTER/>). ASTER image tiles were calculated and are stored on AERIS (<https://observations.ipsl.fr/aeris/eurec4a/Leaflet/index.html>) providing a user-friendly browsing experience with the possibility to zoom in on the rich structures of beautiful trade

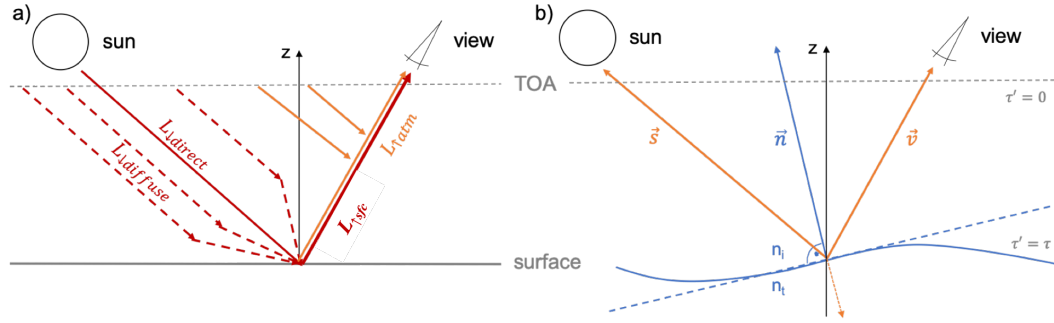


Figure B.11: Sketches of the simple clear-sky model. a) illustrated the main radiance components, while b) shows the geometry setup based on the vectors \vec{s} pointing into the sun, \vec{v} pointing to the sensor, and the wave facet normal \vec{n} .

cumulus cloud fields. The cloud information from WALES is published on AERIS <https://doi.org/10.25326/216> and further described in Konow et al. (2021).

Code for processing the original ASTER L1B data is available in the Python package *typhon* version 0.8.0, subpackage *cloudmask* (<https://github.com/atmtools/typhon>). The basic code for the clear-sky radiative transfer simulations is available at <https://doi.org/10.5281/zenodo.4842675>. The main data resulting from the applied methodology and forming the basis for all interpretations is available at <https://doi.org/10.5281/zenodo.4844482>.

B.7 APPENDIX

B.7.1 Components and equations to the simple clear-sky model (SCSM)

Knowing the extraterrestrial irradiance E_0 emitted by the sun and entering the atmosphere, the radiative transfer equation describes the radiance at any location (x, y, z) and for any direction defined by a zenith angle θ and an azimuthal angle ϕ . In a clear-sky atmosphere with small solar and viewing zenith angles we can use 1D plane-parallel radiative transfer to estimate the radiance observable at the top of atmosphere (TOA).

The clear-sky radiance L reaching a sensor in space is a combination of three main components that we illustrate in Fig. B.11 a): (1) the direct sun ray reflected at the ocean surface $L_{\downarrow \text{direct}}$ and (2) the hemispheric diffuse radiation reflected at the surface towards the sensor $L_{\downarrow \text{diffuse}}$. Together they are combined in the

component $L_{\uparrow sfc}$ of light that touched the surface. On the way from the surface to the sensor $L_{\uparrow sfc}$ experiences attenuation following Lambert-Beer and depending on the atmospheric optical thickness τ and the cosine of the sensor or view zenith angle v_z . In addition, there is component (3), the diffuse light from single-scattering events happening within the atmosphere $L_{\uparrow atm}$.

$$L = L_{\uparrow sfc} + L_{\uparrow atm} \quad (B.14)$$

$$= \exp\left(\frac{-\tau}{v_z}\right) [L_{\downarrow direct} + L_{\downarrow diffuse}] + L_{\uparrow atm} \quad (B.15)$$

In the following, we describe the derivation of L based on the vector \vec{s} pointing from an observed location on the ground to the sun, and the view vector \vec{v} pointing to the sensor (see Fig. B.11 b)).

$$\vec{s} = \begin{pmatrix} s_x \\ s_y \\ s_z \end{pmatrix}, \vec{v} = \begin{pmatrix} v_x \\ v_y \\ v_z \end{pmatrix} \quad (B.16)$$

\vec{s} and \vec{v} are unit vectors meaning that they satisfy the condition:

$$|\vec{s}| = |\vec{v}| = 1. \quad (B.17)$$

Working with vectors instead of the traditional approach with angles simplifies several of the following calculations next to a significant enhancement in computational speed. For example, the previously mentioned view zenith angle v_z is simply the third component of the view vector \vec{v} .

B.7.1.1 Direct radiance and the bi-directional reflection function (BRDF)

$L_{\downarrow direct}$ is defined by the sensor-sun geometry with the cosine of the sun zenith angle s_z and the corresponding aerosol extinction along the path from the top of atmosphere (TOA) to the surface where the reflection is characterized by the bi-directional reflection function (BRDF) ρ .

$$L_{\downarrow direct} = E_0 \exp\left(\frac{-\tau}{s_z}\right) \rho(\vec{s}, \vec{v}, ws, n_i, n_t) \quad (B.18)$$

How a sun ray is reflected at the ocean surface mostly depends on the surface wind speed ws and the generated wave slopes. The earliest and still widely used surface slope parametrization goes back to photographic measurements by Cox

and Munk in 1954. Their parametrization is embedded in a 1D Guassian surface slope distribution p , combined with Fresnel reflection coefficients for unpolarized light r and a prefactor handling the sensor-sun geometry with the sun \vec{s} and view \vec{v} vectors. For the general equation for ρ we follow Stamnes, Thomas, and Stamnes (2017):

$$\rho(\vec{s}, \vec{v}, ws, n_i, n_t) = \frac{1}{4v_z s_z (n_z)^4} \cdot p(\vec{s}, \vec{v}, ws) \cdot r(\vec{s}, \vec{v}, n_i, n_t) \quad (\text{B.19})$$

In the first factor, n_z is the third component of the wave facet normal \vec{n} with

$$\vec{n} = \begin{pmatrix} n_x \\ n_y \\ n_z \end{pmatrix} = \frac{\vec{s} + \vec{v}}{|\vec{s} + \vec{v}|} \quad (\text{B.20})$$

The second factor in Eq. B.19 gives the probability of a specular reflection p and the third the intensity of the reflected light r . In detail, we assume a 1D Guassian surface slope probability distribution p with

$$p(\vec{s}, \vec{v}, ws) = \frac{1}{\pi \sigma(ws)^2} \exp\left(-\frac{1 - n_z^2}{n_z^2 \cdot \sigma(ws)^2}\right) \quad (\text{B.21})$$

and the variance σ^2 of the surface slope distribution. The Cox and Munk parametrization provides an empirical estimate for σ^2 depending on the 10 m surface wind speed ws (Cox and Munk, 1954):

$$\sigma(ws)^2 = 0.003 + 0.00512 \cdot ws. \quad (\text{B.22})$$

The intensity of the reflected light r is given by the unpolarized Fresnel reflection coefficient:

$$r(\vec{s}, \vec{v}, n_i, n_t) = \frac{1}{2} \left[\left(\frac{\mu_i - n_r \mu_t}{\mu_i + n_r \mu_t} \right)^2 + \left(\frac{\mu_t - n_r \mu_i}{\mu_t + n_r \mu_i} \right)^2 \right] \quad (\text{B.23})$$

with $n_r = \frac{n_t}{n_i}$, the ratio of the refractive index of the transmitted medium $n_t = 1.333$ (ocean) and the refractive index of the incoming medium $n_i = 1$ (atmosphere). Further, μ_i is the cosine of the incidence angle and is given by the dot product of the sun and wave facet normal vector:

$$\mu_i = \vec{s} \cdot \vec{n} \quad (\text{B.24})$$

μ_t is the cosine of the transmission angle, which follows directly from Snell's law by transformation:

$$\mu_t = \sqrt{1 - \frac{1 - \mu_i^2}{n_r^2}} \quad (\text{B.25})$$

B.7.1.2 Diffuse downward radiance and hemispheric BRDF

The hemispheric diffuse radiance $L_{\downarrow \text{diffuse}}$ includes sun rays that are scattered within the atmosphere on their way to the ground and get reflected at the pixel of interest into the direction of the sensor view. Thus, we integrate the integration vector \vec{x} over the hemisphere Ω :

$$L_{\downarrow \text{diffuse}} = \int_{\Omega} \rho(\vec{x}, \vec{v}, ws) \cdot L_{\text{in}}(\tau, \vec{x}) d\vec{x} \quad (\text{B.26})$$

Assuming that the incoming diffuse downward radiance $L_{\text{in}}(\tau, \vec{x})$ is isotropic, we can pull L_{in} out of the integral and derive a hemispheric BRDF by integrating equation B.19 over Ω . Here, we make use of the Gauss-Legendre quadrature to approximate the integral based on only a few nodes in the μ space while keeping a high accuracy.

The diffuse downward irradiance on the other hand is difficult to approximate. Thus, we sample from a pre-calculated look-up table of diffuse downward irradiance for a range of sun zenith angles and aerosol optical depths. The look-up table was calculated with the full radiative transfer model libRadtran for a sensor at the surface pointing up nadir and observing at ASTER's band 3 central wavelength 807 nm (Emde et al., 2016; Mayer and Kylling, 2005). The input file defines a U.S. Standard Atmosphere with default molecular absorption calculated with the representative wavelengths parameterization REPTRAN (medium) where the absorption is based on the HITRAN 2004 catalog. The aerosols species is set to be *maritime tropical* as defined by the OPAC package and finally, the radiative transfer equation is solved with DISORT. We further use the bivariate spline approximation provided within the Python package *scipy* (version 1.5.2) to interpolate over the output look-up table.

B.7.1.3 Diffuse upward radiance from single-scattering events

The atmospheric diffuse scattering $L_{\uparrow\text{atm}}$ describes sun rays that are reflected within the atmosphere into the view direction of the sensor. We only consider single scattering events as the aerosol optical depth over tropical ocean is mostly below or in the order of 0.1 and the probability of further scattering events is unlikely. The extinction within an atmospheric column is generally given by the integral over the extinction coefficients $\sigma_{\text{ext},i}$ in single atmospheric layers depending on their density (temperature) and particles. We simplify the problem by integrating over τ instead of the atmospheric path lengths with $dl = \frac{dz}{\cos(\theta)}$ of a respective zenith angle θ . Correspondingly, we can write the integral over all single (aerosol) scattering events along an atmospheric path l from the surface to TOA

$$L_{\uparrow\text{atm}} = E_0 \int_{\text{sfc}}^{\text{TOA}} \exp\left(-\frac{1}{s_z} \int_{z_{\text{scat}}}^{\text{TOA}} \sigma_{\text{ext}}(z) dz\right) \quad (\text{B.27})$$

$$\cdot \exp\left(-\frac{1}{v_z} \int_{z_{\text{scat}}}^{\text{TOA}} \sigma_{\text{ext}}(z) dz\right) \quad (\text{B.28})$$

$$\cdot \sigma_{\text{scat}} \Theta_{\text{HG}} dz_{\text{scat}} \quad (\text{B.29})$$

where the extinction is accounted for in the exponential functions with the scattering event happening at the height z_{scat} . The product of the scattering coefficient σ_{scat} and the scattering phase function Θ_{HG} describes the scattering efficiency.

In our atmospheric column of constant density, σ_{scat} is independent of height and the integral $\int_{\text{sfc}}^{\text{TOA}} \sigma_{\text{scat}} l dl$ simplifies to $\int_0^\tau d\tau'$ with τ being the optical depth of the atmospheric column. In more detail, we can rewrite the relation and include the single scattering albedo ω_0

$$\sigma_{\text{scat}} \cdot dl = \omega_0 \sigma_{\text{ext}} \cdot \frac{dz}{\mu_v} = \frac{\omega_0}{\mu_v} d\tau \quad (\text{B.30})$$

and further include those in Eq. B.27:

$$L_{\uparrow\text{atm}} = \Theta_{\text{HG}} \frac{\omega_o}{\mu_v} \int_0^\tau \exp\left(\frac{-\tau'}{\mu_o}\right) \exp\left(\frac{-\tau'}{\mu_v}\right) d\tau' \quad (\text{B.31})$$

The Henyey Greenstein phase function Θ_{HG} is an approximation for the scattering phase function and only depends on the asymmetry parameter g , that is the

mean cosine of the scattering angle calculated by integrating over the scattering phase function (Henyey and Greenstein, 1941):

$$\Theta_{\text{HG}} = \frac{1}{4\pi} \frac{1 - g^2}{1 + g^2 - 2g(\mu_{\text{scat}})^{3/2}} \quad (\text{B.32})$$

For ω_0 and g we use constant values taken from the libRadtran calculations with the input setup described in Sect. B.7.1.2.

B.7.2 Derivation of the clear-sky fraction

Based on equations Eq. B.6 and Eq. B.7 we could directly solve for the clear-sky fraction $p(\text{F}_{\text{CLEAR}})$.

We start with the clear-sky model output and apply Bayes' theorem:

$$p(\text{F}_{\text{CLEAR}}|\text{R}) = \frac{p(\text{R}|\text{F}_{\text{CLEAR}})}{p(\text{R})} \cdot p(\text{F}_{\text{CLEAR}}) \quad (\text{B.33})$$

We can add this information to Eq. B.7

$$1 - p(\text{F}_{\text{CLOUD}}|\text{R}') = \frac{p(\text{R} = \text{R}'|\text{F}_{\text{CLEAR}})}{p(\text{R} = \text{R}')} \cdot p(\text{F}_{\text{CLEAR}}) \quad (\text{B.34})$$

and solve for $p(\text{F}_{\text{CLEAR}})$

$$p(\text{F}_{\text{CLEAR}}) = \frac{p(\text{R} = \text{R}')}{p(\text{R} = \text{R}'|\text{F}_{\text{CLEAR}})} (1 - p(\text{F}_{\text{CLOUD}}|\text{R}')) \quad (\text{B.35})$$

We further add the information from Eq. B.33 and Eq. B.35 to our constraint stated in Eq. B.6:

$$1 \geq p(\text{F}_{\text{CLEAR}}|\text{R}) + p(\text{F}_{\text{CLOUD}}|\text{R}) \quad (\text{B.36})$$

$$1 \geq \frac{p(\text{R}|\text{F}_{\text{CLEAR}})}{p(\text{R})} \cdot \frac{p(\text{R} = \text{R}')}{p(\text{R} = \text{R}'|\text{F}_{\text{CLEAR}})} (1 - p(\text{F}_{\text{CLOUD}}|\text{R}')) \quad (\text{B.37})$$

$$+ p(\text{F}_{\text{CLOUD}}|\text{R}) \quad (\text{B.38})$$

Rearranging the equation we get

$$\frac{p(\text{R} = \text{R}'')}{p(\text{R} = \text{R}''|\text{F}_{\text{CLEAR}})} (1 - p(\text{F}_{\text{CLOUD}}|\text{R}'')) \quad (\text{B.39})$$

$$\geq \frac{p(\text{R} = \text{R}')}{p(\text{R} = \text{R}'|\text{F}_{\text{CLEAR}})} (1 - p(\text{F}_{\text{CLOUD}}|\text{R}')) \quad \forall \text{R}'' \in \text{R} \quad (\text{B.40})$$

and consequently we can find R' by searching for the minimum:

$$R' = \operatorname{argmin}_{R''} \left(\frac{p(R = R'')}{p(R = R'' | F_{\text{CLEAR}})} - (1 - p(F_{\text{CLOUD}} | R'')) \right) \quad (\text{B.41})$$

Knowing the R' we could in principle derive the clear-sky fraction $p(F_{\text{CLEAR}})$ from Equ. B.35. However, Equ. B.41 becomes unstable where $p(F_{\text{CLOUD}} | R'')$ is close to 1 which corresponds to cloudy parts while we are interested in the clear part of the distribution. We therefore apply the modified method described in Sec. ?? in the current study.

AUTHOR CONTRIBUTIONS BS and TM conceptualized the study. TK, MB, and TM worked out the methodology. MW derived the lidar cloud optical thickness data. SB and BS supervised the project. TM conducted the analysis, and prepared the manuscript with contributions from all co-authors.

COMPETING INTERESTS The authors declare that they have no conflict of interest.

ACKNOWLEDGEMENTS This study was supported by the International Max Planck Research School on Earth System Modelling (IMPRS-ESM), Hamburg, and the Universität Hamburg. It also contributes to the Cluster of Excellence “CLICCS—Climate, Climatic Change, and Society” funded by DFG (EXC 2037, Project Number 390683824), and to the Center for Earth System Research and Sustainability (CEN) of Universität Hamburg.

The ASTER L1B data product was retrieved from the online Data Pool, courtesy of the NASA Land Processes Distributed Active Archive Center (LP DAAC), USGS/Earth Resources Observation and Science (EROS) Center, Sioux Falls, South Dakota (Last accessed 2021-04-21 from https://doi.org/10.5067/ASTER/AST_L1B.003). We would like to thank the ASTER Science Team for scheduling the ASTER data acquisition in support of the EUREC⁴A field campaign. We acknowledge ECMWF and the Copernicus Climate Change Service for providing access to the ERA5 data set through the Climate Data Storage API (last accessed 2021-04-21). Theresa Mieslinger would like to thank Bernhard Mayer for his feedback on a suitable libRadtran setup, as well as Jean-Louis Dufresne for helpful discussions on the cloud cover - cloud reflectance relationship in climate models.

BIBLIOGRAPHY

- Albrecht, Bruce A. (1989). "Aerosols, Cloud Microphysics, and Fractional Cloudiness." *Science* 245.4923, pp. 1227–1230. ISSN: 0036-8075. DOI: [10.1126/science.245.4923.1227](https://doi.org/10.1126/science.245.4923.1227). eprint: <https://science.sciencemag.org/content/245/4923/1227.full.pdf>. URL: <https://science.sciencemag.org/content/245/4923/1227>.
- Baum, Bryan A., W. Paul Menzel, Richard A. Frey, David C. Tobin, Robert E. Holz, Steve A. Ackerman, Andrew K. Heidinger, and Ping Yang (2012). "MODIS Cloud-Top Property Refinements for Collection 6." *Journal of Applied Meteorology and Climatology* 51.6, pp. 1145–1163. DOI: [10.1175/JAMC-D-11-0203.1](https://doi.org/10.1175/JAMC-D-11-0203.1). eprint: <http://dx.doi.org/10.1175/JAMC-D-11-0203.1>. URL: <http://dx.doi.org/10.1175/JAMC-D-11-0203.1>.
- Belmonte Rivas, M. and A. Stoffelen (2019). "Characterizing ERA-Interim and ERA5 surface wind biases using ASCAT." *Ocean Science* 15.3, pp. 831–852. DOI: [10.5194/os-15-831-2019](https://doi.org/10.5194/os-15-831-2019). URL: <https://os.copernicus.org/articles/15/831/2019/>.
- Benner, Timothy C. and Judith A. Curry (1998). "Characteristics of small tropical cumulus clouds and their impact on the environment." *Journal of Geophysical Research: Atmospheres* 103.D22, pp. 28753–28767. DOI: [10.1029/98JD02579](https://doi.org/10.1029/98JD02579). eprint: <https://agupubs.onlinelibrary.wiley.com/doi/pdf/10.1029/98JD02579>. URL: <https://agupubs.onlinelibrary.wiley.com/doi/abs/10.1029/98JD02579>.
- Berrisford, P., D.P. Dee, P. Poli, R. Brugge, K. Fielding, M. Fuentes, P.W. Kållberg, S. Kobayashi, S. Uppala, and A. Simmons (2011). *The ERA-Interim archive Version 2.0*. Shinfield Park, Reading, p. 23.
- Bony, Sandrine and Jean-Louis Dufresne (2005). "Marine boundary layer clouds at the heart of tropical cloud feedback uncertainties in climate models." *Geophysical Research Letters* 32.20. DOI: [10.1029/2005GL023851](https://doi.org/10.1029/2005GL023851). eprint: <https://agupubs.onlinelibrary.wiley.com/doi/pdf/10.1029/2005GL023851>. URL: <https://agupubs.onlinelibrary.wiley.com/doi/abs/10.1029/2005GL023851>.
- Bony, Sandrine, Hauke Schulz, Jessica Vial, and Bjorn Stevens (2020). "Sugar, Gravel, Fish, and Flowers: Dependence of Mesoscale Patterns of Trade-Wind Clouds on Environmental Conditions." *Geophysical Research Letters* 47.7. e2019GL085988. DOI: <https://doi.org/10.1029/2019GL085988>. eprint: <https://agupubs.onlinelibrary.wiley.com/doi/pdf/10.1029/2019GL085988>. URL: <https://agupubs.onlinelibrary.wiley.com/doi/abs/10.1029/2019GL085988>.

- Bony, Sandrine et al. (Mar. 2015). "Clouds, circulation and climate sensitivity." *Nature Geoscience* 8.4, pp. 261–268. ISSN: 1752-0894. DOI: [10.1038/ngeo2398](https://doi.org/10.1038/ngeo2398). URL: <http://dx.doi.org/10.1038/ngeo2398>.
- Bony, Sandrine et al. (Nov. 2017). "EUREC4A: A Field Campaign to Elucidate the Couplings Between Clouds, Convection and Circulation." *Surveys in Geophysics* 38.6, pp. 1529–1568. ISSN: 1573-0956. DOI: [10.1007/s10712-017-9428-0](https://doi.org/10.1007/s10712-017-9428-0). URL: <https://doi.org/10.1007/s10712-017-9428-0>.
- Bretherton, Christopher S. and Peter N. Blossey (2014). "Low cloud reduction in a greenhouse-warmed climate: Results from Lagrangian LES of a subtropical marine cloudiness transition." *Journal of Advances in Modeling Earth Systems* 6.1, pp. 91–114. DOI: [10.1002/2013MS000250](https://doi.org/10.1002/2013MS000250). eprint: <https://agupubs.onlinelibrary.wiley.com/doi/pdf/10.1002/2013MS000250>. URL: <https://agupubs.onlinelibrary.wiley.com/doi/abs/10.1002/2013MS000250>.
- Bretherton, Christopher S., Peter N. Blossey, and Christopher R. Jones (2013). "Mechanisms of marine low cloud sensitivity to idealized climate perturbations: A single-LES exploration extending the CGILS cases." *Journal of Advances in Modeling Earth Systems* 5.2, pp. 316–337. DOI: [10.1002/jame.20019](https://doi.org/10.1002/jame.20019). eprint: <https://agupubs.onlinelibrary.wiley.com/doi/pdf/10.1002/jame.20019>. URL: <https://agupubs.onlinelibrary.wiley.com/doi/abs/10.1002/jame.20019>.
- Brient, F. and S. Bony (2012). "How may low-cloud radiative properties simulated in the current climate influence low-cloud feedbacks under global warming?" *Geophysical Research Letters* 39.20. DOI: <https://doi.org/10.1029/2012GL053265>. eprint: <https://agupubs.onlinelibrary.wiley.com/doi/pdf/10.1029/2012GL053265>. URL: <https://agupubs.onlinelibrary.wiley.com/doi/abs/10.1029/2012GL053265>.
- Brueck, Matthias, Louise Nuijens, and Bjorn Stevens (2015). "On the Seasonal and Synoptic Time-Scale Variability of the North Atlantic Trade Wind Region and Its Low-Level Clouds." *Journal of the Atmospheric Sciences* 72.4, pp. 1428–1446. DOI: [10.1175/JAS-D-14-0054.1](https://doi.org/10.1175/JAS-D-14-0054.1). eprint: <http://dx.doi.org/10.1175/JAS-D-14-0054.1>. URL: <http://dx.doi.org/10.1175/JAS-D-14-0054.1>.
- Cahalan, Robert F. and Joachim H. Joseph (1989). "Fractal Statistics of Cloud Fields." *Monthly Weather Review* 117.2, pp. 261–272. DOI: [10.1175/1520-0493\(1989\)117<0261:FSOCF>2.0.CO;2](https://doi.org/10.1175/1520-0493(1989)117<0261:FSOCF>2.0.CO;2). eprint: [http://dx.doi.org/10.1175/1520-0493\(1989\)117<0261:FSOCF>2.0.CO;2](http://dx.doi.org/10.1175/1520-0493(1989)117<0261:FSOCF>2.0.CO;2). URL: [http://dx.doi.org/10.1175/1520-0493\(1989\)117<0261:FSOCF>2.0.CO;2](http://dx.doi.org/10.1175/1520-0493(1989)117<0261:FSOCF>2.0.CO;2).
- Clauset, A., C. Shalizi, and M. Newman (2009). "Power-Law Distributions in Empirical Data." *SIAM Review* 51.4, pp. 661–703. DOI: [10.1137/070710111](https://doi.org/10.1137/070710111). eprint: <https://doi.org/10.1137/070710111>. URL: <https://doi.org/10.1137/070710111>.
- Cox, Charles and Walter Munk (1954). "Measurement of the Roughness of the Sea Surface from Photographs of the Sun's Glitter." *J. Opt. Soc. Am.* 44.11, pp. 838–850.

- DOI: 10.1364/JOSA.44.000838. URL: <http://www.osapublishing.org/abstract.cfm?URI=josa-44-11-838>.
- Davies, R. (1978). "The Effect of Finite Geometry on the Three-Dimensional Transfer of Solar Irradiance in Clouds." *Journal of Atmospheric Sciences* 35.9, pp. 1712 – 1725. DOI: 10.1175/1520-0469(1978)035<1712:TE0FG0>2.0.CO;2. URL: https://journals.ametsoc.org/view/journals/atsc/35/9/1520-0469_1978_035_1712_teofgo_2_0_co_2.xml.
- Dawe, J. T. and P. H. Austin (2012). "Statistical analysis of an LES shallow cumulus cloud ensemble using a cloud tracking algorithm." *Atmospheric Chemistry and Physics* 12.2, pp. 1101–1119. DOI: 10.5194/acp-12-1101-2012. URL: <https://www.atmos-chem-phys.net/12/1101/2012/>.
- Dee, D. P. et al. (2011). "The ERA-Interim reanalysis: configuration and performance of the data assimilation system." *Quarterly Journal of the Royal Meteorological Society* 137.656, pp. 553–597. ISSN: 1477-870X. DOI: 10.1002/qj.828. URL: <http://dx.doi.org/10.1002/qj.828>.
- Dey, Sagnik, Larry Di Girolamo, and Guangyu Zhao (2008). "Scale effect on statistics of the macrophysical properties of trade wind cumuli over the tropical western Atlantic during RICO." *Journal of Geophysical Research: Atmospheres* 113.D24. DOI: <https://doi.org/10.1029/2008JD010295>. eprint: <https://agupubs.onlinelibrary.wiley.com/doi/pdf/10.1029/2008JD010295>. URL: <https://agupubs.onlinelibrary.wiley.com/doi/abs/10.1029/2008JD010295>.
- Dussen, J. J. van der, S. R. de Roode, S. Dal Gesso, and A. P. Siebesma (2015). "An LES model study of the influence of the free tropospheric thermodynamic conditions on the stratocumulus response to a climate perturbation." *Journal of Advances in Modeling Earth Systems* 7.2, pp. 670–691. DOI: 10.1002/2014MS000380. eprint: <https://agupubs.onlinelibrary.wiley.com/doi/pdf/10.1002/2014MS000380>. URL: <https://agupubs.onlinelibrary.wiley.com/doi/abs/10.1002/2014MS000380>.
- Eitzen, Zachary A., Kuan-Man Xu, and Takmeng Wong (2011). "An Estimate of Low-Cloud Feedbacks from Variations of Cloud Radiative and Physical Properties with Sea Surface Temperature on Interannual Time Scales." *Journal of Climate* 24.4, pp. 1106–1121. DOI: 10.1175/2010JCLI3670.1. eprint: <https://doi.org/10.1175/2010JCLI3670.1>. URL: <https://doi.org/10.1175/2010JCLI3670.1>.
- Emde, C. et al. (2016). "The libRadtran software package for radiative transfer calculations (version 2.0.1)." *Geoscientific Model Development* 9.5, pp. 1647–1672. DOI: 10.5194/gmd-9-1647-2016. URL: <https://gmd.copernicus.org/articles/9/1647/2016/>.
- Esselborn, Michael, Martin Wirth, Andreas Fix, Matthias Tesche, and Gerhard Ehret (2008). "Airborne high spectral resolution lidar for measuring aerosol extinction and backscatter coefficients." *Appl. Opt.* 47.3, pp. 346–358. DOI: 10.1364/AO.47.000346. URL: <http://ao.osa.org/abstract.cfm?URI=ao-47-3-346>.

- Genkova, Iliana, Gabriela Seiz, Paquita Zuidema, Guangyu Zhao, and Larry Di Girolamo (2007). "Cloud top height comparisons from ASTER, MISR, and {MODIS} for trade wind cumuli." *Remote Sensing of Environment* 107.1–2. Multi-angle Imaging SpectroRadiometer (MISR) Special IssueMISR Special Issue, pp. 211 –222. ISSN: 0034-4257. DOI: <https://doi.org/10.1016/j.rse.2006.07.021>. URL: <http://www.sciencedirect.com/science/article/pii/S0034425706004421>.
- George, G. et al. (under review). "JOANNE : Joint dropsonde Observations of the Atmosphere in tropical North atlaNtic meso-scale Environments." *Earth System Science Data Discussions* 2021, pp. 1–33. DOI: [10.5194/essd-2021-162](https://doi.org/10.5194/essd-2021-162). URL: <https://essd.copernicus.org/preprints/essd-2021-162/>.
- George, Geet, Bjorn Stevens, Sandrine Bony, Marcus Klingebiel, and Raphaela Vogel (May 2021). "Observed impact of meso-scale vertical motion on cloudiness." *Journal of the Atmospheric Sciences*. DOI: [10.1175/jas-d-20-0335.1](https://doi.org/10.1175/jas-d-20-0335.1). URL: <https://doi.org/10.1175%2Fjas-d-20-0335.1>.
- Gotoh, Kazuo and Yasuhiko Fujii (1998). "A Fractal Dimensional Analysis on the Cloud Shape Parameters of Cumulus over Land." *Journal of Applied Meteorology* 37.10, pp. 1283–1292. DOI: [10.1175/1520-0450\(1998\)037<1283:AFDAOT>2.0.CO;2](https://doi.org/10.1175/1520-0450(1998)037<1283:AFDAOT>2.0.CO;2). eprint: [https://doi.org/10.1175/1520-0450\(1998\)037<1283:AFDAOT>2.0.CO;2](https://doi.org/10.1175/1520-0450(1998)037<1283:AFDAOT>2.0.CO;2). URL: [https://doi.org/10.1175/1520-0450\(1998\)037<1283:AFDAOT>2.0.CO;2](https://doi.org/10.1175/1520-0450(1998)037<1283:AFDAOT>2.0.CO;2).
- Greenwald, Thomas J., Ralf Bennartz, Matthew Lebsock, and João Teixeira (2018). "An Uncertainty Data Set for Passive Microwave Satellite Observations of Warm Cloud Liquid Water Path." *Journal of Geophysical Research: Atmospheres* 123.7, pp. 3668–3687. DOI: [10.1002/2017JD027638](https://doi.org/10.1002/2017JD027638). eprint: <https://agupubs.onlinelibrary.wiley.com/doi/pdf/10.1002/2017JD027638>. URL: <https://agupubs.onlinelibrary.wiley.com/doi/abs/10.1002/2017JD027638>.
- Gryspeerdt, E., J. Quaas, and N. Bellouin (2016). "Constraining the aerosol influence on cloud fraction." *Journal of Geophysical Research: Atmospheres* 121.7, pp. 3566–3583. DOI: <https://doi.org/10.1002/2015JD023744>. eprint: <https://agupubs.onlinelibrary.wiley.com/doi/pdf/10.1002/2015JD023744>. URL: <https://agupubs.onlinelibrary.wiley.com/doi/abs/10.1002/2015JD023744>.
- Gutleben, Manuel, Silke Groß, Martin Wirth, Claudia Emde, and Bernhard Mayer (2019). "Impacts of water vapor on Saharan air layer radiative heating." *Geophysical Research Letters* 46.24, pp. 14854–14862. URL: <https://elib.dlr.de/134038/>.
- Hadley, George (1734). "Concerning the Cause of the General Trade-Winds." *Phil Trans, Roy. Soc.* 34.
- Halley, Edmond (1686). "An Historical Account of the trade Winds, and Monsoons, observable in the Seas between and near the Tropics, with an attempt to assign the Physical Cause of said Winds." *Phil Trans, Roy. Soc.* 16.
- Hartmann, Dennis L. and David A. Short (June 1980). "On the Use of Earth Radiation Budget Statistics for Studies of Clouds and Climate." *Journal of the At-*

- Atmospheric Sciences* 37.6, pp. 1233–1250. DOI: [10.1175/1520-0469\(1980\)037<1233:atuoer>2.0.co;2](https://doi.org/10.1175/1520-0469(1980)037<1233:atuoer>2.0.co;2). URL: <https://doi.org/10.1175%2F1520-0469%281980%29037%3C1233%3Aotuoer%3E2.0.co%3B2>.
- Heinze, Rieke et al. (2017). “Large-eddy simulations over Germany using ICON: a comprehensive evaluation.” *Quarterly Journal of the Royal Meteorological Society* 143.702, pp. 69–100. DOI: <https://doi.org/10.1002/qj.2947>. eprint: <https://rmets.onlinelibrary.wiley.com/doi/pdf/10.1002/qj.2947>. URL: <https://rmets.onlinelibrary.wiley.com/doi/abs/10.1002/qj.2947>.
- Heney, L. G. and J. L. Greenstein (Jan. 1941). “Diffuse radiation in the Galaxy.” *Astrophysical Journal* 93, pp. 70–83. DOI: [10.1086/144246](https://doi.org/10.1086/144246).
- Hersbach, Hans et al. (2020). “The ERA5 global reanalysis.” *Quarterly Journal of the Royal Meteorological Society* 146.730, pp. 1999–2049. DOI: <https://doi.org/10.1002/qj.3803>. eprint: <https://rmets.onlinelibrary.wiley.com/doi/pdf/10.1002/qj.3803>. URL: <https://rmets.onlinelibrary.wiley.com/doi/abs/10.1002/qj.3803> (visited on 01/05/2021).
- Heus, T. and A. Seifert (2013). “Automated tracking of shallow cumulus clouds in large domain, long duration large eddy simulations.” *Geoscientific Model Development* 6.4, pp. 1261–1273. DOI: [10.5194/gmd-6-1261-2013](https://doi.org/10.5194/gmd-6-1261-2013). URL: <http://www.geosci-model-dev.net/6/1261/2013/>.
- Hildebrandsson, Hugo Hildebrand, Wladimir Peter Köppen, and Georg Neumayer (1890). “*Wolken-Atlas / Atlas des nuages / Cloud-Atlas*.”
- Hinkelman, Laura M., K. Franklin Evans, Eugene E. Clothiaux, Thomas P. Ackerman, and Paul W. Stackhouse (2007). “The Effect of Cumulus Cloud Field Anisotropy on Domain-Averaged Solar Fluxes and Atmospheric Heating Rates.” *Journal of the Atmospheric Sciences* 64.10, pp. 3499–3520. DOI: [10.1175/JAS4032.1](https://doi.org/10.1175/JAS4032.1). eprint: <https://doi.org/10.1175/JAS4032.1>. URL: <https://doi.org/10.1175/JAS4032.1>.
- Hohenegger, Cathy and Bjorn Stevens (2016). “Coupled radiative convective equilibrium simulations with explicit and parameterized convection.” *Journal of Advances in Modeling Earth Systems* 8.3, pp. 1468–1482. DOI: <https://doi.org/10.1002/2016MS000666>. eprint: <https://agupubs.onlinelibrary.wiley.com/doi/pdf/10.1002/2016MS000666>. URL: <https://agupubs.onlinelibrary.wiley.com/doi/abs/10.1002/2016MS000666>.
- Howard, Luke (1803). “XVIII. On the modifications of clouds, and on the principles of their production, suspension, and destruction; being the substance of an essay read before the Askesian Society in the session 1802–3.” *The Philosophical Magazine* 16.62, pp. 97–107. DOI: [10.1080/14786440308676310](https://doi.org/10.1080/14786440308676310). eprint: <https://doi.org/10.1080/14786440308676310>. URL: <https://doi.org/10.1080/14786440308676310>.
- Jacob, M., P. Kollias, F. Ament, V. Schemann, and S. Crewell (2020). “Multilayer cloud conditions in trade wind shallow cumulus – confronting two ICON model derivatives with airborne observations.” *Geoscientific Model Development* 13.11,

- pp. 5757–5777. DOI: [10.5194/gmd-13-5757-2020](https://doi.org/10.5194/gmd-13-5757-2020). URL: <https://gmd.copernicus.org/articles/13/5757/2020/>.
- Jiang, Hongli, Graham Feingold, Haflidi H. Jonsson, Miao-Ling Lu, Patrick Y. Chuang, Richard C. Flagan, and John H. Seinfeld (2008). “Statistical comparison of properties of simulated and observed cumulus clouds in the vicinity of Houston during the Gulf of Mexico Atmospheric Composition and Climate Study (GoMACCS).” *Journal of Geophysical Research: Atmospheres* 113.D13. DOI: [10.1029/2007JD009304](https://doi.org/10.1029/2007JD009304). eprint: <https://agupubs.onlinelibrary.wiley.com/doi/pdf/10.1029/2007JD009304>. URL: <https://agupubs.onlinelibrary.wiley.com/doi/abs/10.1029/2007JD009304>.
- Kaufman, Yoram J., Ilan Koren, Lorraine A. Remer, Daniel Rosenfeld, and Yinon Rudich (2005). “The effect of smoke, dust, and pollution aerosol on shallow cloud development over the Atlantic Ocean.” *Proceedings of the National Academy of Sciences* 102.32, pp. 11207–11212. ISSN: 0027-8424. DOI: [10.1073/pnas.0505191102](https://doi.org/10.1073/pnas.0505191102). eprint: <https://www.pnas.org/content/102/32/11207.full.pdf>. URL: <https://www.pnas.org/content/102/32/11207>.
- King, M. D., W. P. Menzel, Y. J. Kaufman, D. Tanre, Bo-Cai Gao, S. Platnick, S. A. Ackerman, L. A. Remer, R. Pincus, and P. A. Hubanks (2003). “Cloud and aerosol properties, precipitable water, and profiles of temperature and water vapor from MODIS.” *IEEE Transactions on Geoscience and Remote Sensing* 41.2, pp. 442–458. ISSN: 0196-2892. DOI: [10.1109/TGRS.2002.808226](https://doi.org/10.1109/TGRS.2002.808226).
- Klein, Stephen A. (1997). “Synoptic Variability of Low-Cloud Properties and Meteorological Parameters in the Subtropical Trade Wind Boundary Layer.” *Journal of Climate* 10.8, pp. 2018–2039. DOI: [10.1175/1520-0442\(1997\)010<2018:SVOLCP>2.0.CO;2](https://doi.org/10.1175/1520-0442(1997)010<2018:SVOLCP>2.0.CO;2). eprint: [https://doi.org/10.1175/1520-0442\(1997\)010<2018:SVOLCP>2.0.CO;2](https://doi.org/10.1175/1520-0442(1997)010<2018:SVOLCP>2.0.CO;2). URL: [https://doi.org/10.1175/1520-0442\(1997\)010<2018:SVOLCP>2.0.CO;2](https://doi.org/10.1175/1520-0442(1997)010<2018:SVOLCP>2.0.CO;2).
- Klein, Stephen A., Alex Hall, Joel R. Norris, and Robert Pincus (2018). “Low-Cloud Feedbacks from Cloud-Controlling Factors: A Review.” In: *Shallow Clouds, Water Vapor, Circulation, and Climate Sensitivity*. Ed. by Robert Pincus, David Winker, Sandrine Bony, and Bjorn Stevens. Cham: Springer International Publishing, pp. 135–157. ISBN: 978-3-319-77273-8. DOI: [10.1007/978-3-319-77273-8_7](https://doi.org/10.1007/978-3-319-77273-8_7). URL: https://doi.org/10.1007/978-3-319-77273-8_7.
- Klein, Stephen A. and Dennis L. Hartmann (1993). “The Seasonal Cycle of Low Stratiform Clouds.” *Journal of Climate* 6.8, pp. 1587–1606. DOI: [10.1175/1520-0442\(1993\)006<1587:TSCOLS>2.0.CO;2](https://doi.org/10.1175/1520-0442(1993)006<1587:TSCOLS>2.0.CO;2). eprint: [https://doi.org/10.1175/1520-0442\(1993\)006<1587:TSCOLS>2.0.CO;2](https://doi.org/10.1175/1520-0442(1993)006<1587:TSCOLS>2.0.CO;2). URL: [https://doi.org/10.1175/1520-0442\(1993\)006<1587:TSCOLS>2.0.CO;2](https://doi.org/10.1175/1520-0442(1993)006<1587:TSCOLS>2.0.CO;2).
- Klein, Stephen A., Yuying Zhang, Mark D. Zelinka, Robert Pincus, James Boyle, and Peter J. Gleckler (2013). “Are climate model simulations of clouds improving? An evaluation using the ISCCP simulator.” *Journal of Geophysical Research: Atmospheres*

- 118.3, pp. 1329–1342. DOI: <https://doi.org/10.1002/jgrd.50141>. eprint: <https://agupubs.onlinelibrary.wiley.com/doi/pdf/10.1002/jgrd.50141>. URL: <https://agupubs.onlinelibrary.wiley.com/doi/abs/10.1002/jgrd.50141>.
- Klocke, Daniel, Matthias Brueck, Cathy Hohenegger, and Bjorn Stevens (2017). “Rediscovery of the doldrums in storm-resolving simulations over the tropical Atlantic.” *Nature Geoscience* 10.12, pp. 891–896. ISSN: 1752-0908. DOI: [10.1038/s41561-017-0005-4](https://doi.org/10.1038/s41561-017-0005-4). URL: <https://doi.org/10.1038/s41561-017-0005-4>.
- Knofczynski, Gregory T. and Daniel Mundfrom (2008). “Sample Sizes When Using Multiple Linear Regression for Prediction.” *Educational and Psychological Measurement* 68.3, pp. 431–442. DOI: [10.1177/0013164407310131](https://doi.org/10.1177/0013164407310131). eprint: <https://doi.org/10.1177/0013164407310131>. URL: <https://doi.org/10.1177/0013164407310131>.
- Kölling, Tobias (2020). “Cloud geometry for passive remote sensing.” URL: <http://nbn-resolving.de/urn:nbn:de:bvb:19-261616>.
- Konow, H. et al. (2021). “EUREC⁴A’s HALO.” *Earth System Science Data Discussions* 2021, pp. 1–26. DOI: [10.5194/essd-2021-193](https://doi.org/10.5194/essd-2021-193). URL: <https://essd.copernicus.org/preprints/essd-2021-193/>.
- Konsta, D., J.-L. Dufresne, H. Chepfer, A. Idelkadi, and G. Cesana (2016). “Use of A-train satellite observations (CALIPSO–PARASOL) to evaluate tropical cloud properties in the LMDZ5 GCM.” *Climate Dynamics* 47.3, pp. 1263–1284. ISSN: 1432-0894. DOI: [10.1007/s00382-015-2900-y](https://doi.org/10.1007/s00382-015-2900-y). URL: <https://doi.org/10.1007/s00382-015-2900-y>.
- Koren, I., L. Oreopoulos, G. Feingold, L. A. Remer, and O. Altaratz (2008). “How small is a small cloud?” *Atmospheric Chemistry and Physics* 8.14, pp. 3855–3864. DOI: [10.5194/acp-8-3855-2008](https://doi.org/10.5194/acp-8-3855-2008). URL: <https://acp.copernicus.org/articles/8/3855/2008/>.
- Koren, Ilan, Lorraine A. Remer, Yoram J. Kaufman, Yinon Rudich, and J. Vanderlei Martins (2007). “On the twilight zone between clouds and aerosols.” *Geophysical Research Letters* 34.8. DOI: <https://doi.org/10.1029/2007GL029253>. eprint: <https://agupubs.onlinelibrary.wiley.com/doi/pdf/10.1029/2007GL029253>. URL: <https://agupubs.onlinelibrary.wiley.com/doi/abs/10.1029/2007GL029253>.
- Krautstrunk, Monika and Andreas Giez (2012). “The Transition From FALCON to HALO Era Airborne Atmospheric Research.” In: *Atmospheric Physics: Background – Methods – Trends*. Ed. by Ulrich Schumann. Berlin, Heidelberg: Springer Berlin Heidelberg, pp. 609–624. ISBN: 978-3-642-30183-4. DOI: [10.1007/978-3-642-30183-4_37](https://doi.org/10.1007/978-3-642-30183-4_37). URL: https://doi.org/10.1007/978-3-642-30183-4_37.
- Kubar, Terence L., Duane E. Waliser, J.-L. Li, and Xianan Jiang (2012). “On the Annual Cycle, Variability, and Correlations of Oceanic Low-Topped Clouds with Large-Scale Circulation Using Aqua MODIS and ERA-Interim.” *Journal of Climate* 25.18, pp. 6152–6174. DOI: [10.1175/JCLI-D-11-00478.1](https://doi.org/10.1175/JCLI-D-11-00478.1). eprint: <https://doi.org/10.1175/JCLI-D-11-00478.1>.

- [//doi.org/10.1175/JCLI-D-11-00478.1](https://doi.org/10.1175/JCLI-D-11-00478.1). URL: <https://doi.org/10.1175/JCLI-D-11-00478.1>.
- Lacis, Andrew A. and James Hansen (1974). "A Parameterization for the Absorption of Solar Radiation in the Earth's Atmosphere." *Journal of Atmospheric Sciences* 31.1, pp. 118–133. DOI: [10.1175/1520-0469\(1974\)031<0118:APFTA0>2.0.CO;2](https://doi.org/10.1175/1520-0469(1974)031<0118:APFTA0>2.0.CO;2). URL: https://journals.ametsoc.org/view/journals/atsc/31/1/1520-0469_1974_031_0118_apftao_2_0_co_2.xml.
- Leahy, L. V., R. Wood, R. J. Charlson, C. A. Hostetler, R. R. Rogers, M. A. Vaughan, and D. M. Winker (2012). "On the nature and extent of optically thin marine low clouds." *Journal of Geophysical Research: Atmospheres* 117.D22. DOI: <https://doi.org/10.1029/2012JD017929>. eprint: <https://agupubs.onlinelibrary.wiley.com/doi/pdf/10.1029/2012JD017929>. URL: <https://agupubs.onlinelibrary.wiley.com/doi/abs/10.1029/2012JD017929>.
- Loeb, Norman G. and Natividad Manalo-Smith (2005). "Top-of-Atmosphere Direct Radiative Effect of Aerosols over Global Oceans from Merged CERES and MODIS Observations." *Journal of Climate* 18.17, pp. 3506–3526. DOI: [10.1175/JCLI3504.1](https://doi.org/10.1175/JCLI3504.1). URL: <https://journals.ametsoc.org/view/journals/clim/18/17/jcli3504.1.xml>.
- Loeb, Norman G., Natividad Manalo-Smith, Seiji Kato, Walter F. Miller, Shashi K. Gupta, Patrick Minnis, and Bruce A. Wielicki (2003). "Angular Distribution Models for Top-of-Atmosphere Radiative Flux Estimation from the Clouds and the Earth's Radiant Energy System Instrument on the Tropical Rainfall Measuring Mission Satellite. Part I: Methodology." *Journal of Applied Meteorology* 42.2, pp. 240–265. DOI: [10.1175/1520-0450\(2003\)042<0240:ADMFT0>2.0.CO;2](https://doi.org/10.1175/1520-0450(2003)042<0240:ADMFT0>2.0.CO;2). URL: https://journals.ametsoc.org/view/journals/apme/42/2/1520-0450_2003_042_0240_admfto_2.0.co_2.xml.
- Loeb, Norman G., Tamás Várnai, and Roger Davies (1997). "Effect of cloud inhomogeneities on the solar zenith angle dependence of nadir reflectance." *Journal of Geophysical Research: Atmospheres* 102.D8, pp. 9387–9395. DOI: <https://doi.org/10.1029/96JD03719>. eprint: <https://agupubs.onlinelibrary.wiley.com/doi/pdf/10.1029/96JD03719>. URL: <https://agupubs.onlinelibrary.wiley.com/doi/abs/10.1029/96JD03719>.
- López, Raúl Erlando (1977). "The Lognormal Distribution and Cumulus Cloud Populations." *Monthly Weather Review* 105.7, pp. 865–872. DOI: [10.1175/1520-0493\(1977\)105<0865:TLDACC>2.0.CO;2](https://doi.org/10.1175/1520-0493(1977)105<0865:TLDACC>2.0.CO;2). eprint: [http://dx.doi.org/10.1175/1520-0493\(1977\)105<0865:TLDACC>2.0.CO;2](http://dx.doi.org/10.1175/1520-0493(1977)105<0865:TLDACC>2.0.CO;2). URL: [http://dx.doi.org/10.1175/1520-0493\(1977\)105<0865:TLDACC>2.0.CO;2](http://dx.doi.org/10.1175/1520-0493(1977)105<0865:TLDACC>2.0.CO;2).
- Lovejoy, S. (1982). "Area-Perimeter Relation for Rain and Cloud Areas." *Science* 216.4542, pp. 185–187. ISSN: 0036-8075. DOI: [10.1126/science.216.4542.185](https://doi.org/10.1126/science.216.4542.185). eprint: <http://science.sciencemag.org/content/216/4542/185.full.pdf>. URL: <http://science.sciencemag.org/content/216/4542/185>.

- M. Abrams, S. Hook and B. Ramachandran (2002). *ASTER User Handbook Version 2*. Jet Propulsion Laboratory, 4800 Oak Grove Dr., Pasadena, CA 91109. URL: https://asterweb.jpl.nasa.gov/content/03_data/04_Documents/aster_user_guide_v2.pdf (visited on 05/25/2017).
- Malkus, Joanne S. and Herbert Riehl (1964). "Cloud structure and distributions over the tropical Pacific Ocean1." *Tellus* 16.3, pp. 275–287. DOI: <https://doi.org/10.1111/j.2153-3490.1964.tb00167.x>. eprint: <https://onlinelibrary.wiley.com/doi/pdf/10.1111/j.2153-3490.1964.tb00167.x>. URL: <https://onlinelibrary.wiley.com/doi/abs/10.1111/j.2153-3490.1964.tb00167.x>.
- Marshak, Alexander, Steven Platnick, Tamás Várnai, Guoyong Wen, and Robert F. Cahalan (2006). "Impact of three-dimensional radiative effects on satellite retrievals of cloud droplet sizes." *Journal of Geophysical Research: Atmospheres* 111.D9. DOI: <https://doi.org/10.1029/2005JD006686>. eprint: <https://agupubs.onlinelibrary.wiley.com/doi/pdf/10.1029/2005JD006686>. URL: <https://agupubs.onlinelibrary.wiley.com/doi/abs/10.1029/2005JD006686>.
- Mayer, B. and A. Kylling (2005). "Technical note: The libRadtran software package for radiative transfer calculations - description and examples of use." *Atmospheric Chemistry and Physics* 5.7, pp. 1855–1877. DOI: [10.5194/acp-5-1855-2005](https://doi.org/10.5194/acp-5-1855-2005). URL: <https://acp.copernicus.org/articles/5/1855/2005/>.
- Medeiros, Brian and Bjorn Stevens (2011). "Revealing differences in GCM representations of low clouds." *Climate Dynamics* 36.1, pp. 385–399. ISSN: 1432-0894. DOI: [10.1007/s00382-009-0694-5](https://doi.org/10.1007/s00382-009-0694-5). URL: <https://doi.org/10.1007/s00382-009-0694-5>.
- Mieslinger, T., B. Stevens, T. Kölling, M. Brath, M. Wirth, and S. A. Buehler (2021). "Optically thin clouds in the trades." *Atmospheric Chemistry and Physics Discussions* 2021, pp. 1–33. DOI: [10.5194/acp-2021-453](https://doi.org/10.5194/acp-2021-453). URL: <https://acp.copernicus.org/preprints/acp-2021-453/>.
- Mieslinger, Theresa, Ákos Horváth, Stefan A. Buehler, and Mirjana Sakradzija (2019). "The Dependence of Shallow Cumulus Macrophysical Properties on Large-Scale Meteorology as Observed in ASTER Imagery." *Journal of Geophysical Research: Atmospheres* 124.21, pp. 11477–11505. DOI: <https://doi.org/10.1029/2019JD030768>. eprint: <https://agupubs.onlinelibrary.wiley.com/doi/pdf/10.1029/2019JD030768>. URL: <https://agupubs.onlinelibrary.wiley.com/doi/abs/10.1029/2019JD030768>.
- Myers, Timothy A. and Joel R. Norris (2013). "Observational Evidence That Enhanced Subsidence Reduces Subtropical Marine Boundary Layer Cloudiness." *Journal of Climate* 26.19, pp. 7507–7524. DOI: [10.1175/JCLI-D-12-00736.1](https://doi.org/10.1175/JCLI-D-12-00736.1). eprint: <https://doi.org/10.1175/JCLI-D-12-00736.1>. URL: <https://doi.org/10.1175/JCLI-D-12-00736.1>.
- Myers, Timothy A. and Joel R. Norris (2016). "Reducing the uncertainty in subtropical cloud feedback." *Geophysical Research Letters* 43.5, pp. 2144–2148. DOI:

- 10.1002/2015GL067416. eprint: <https://agupubs.onlinelibrary.wiley.com/doi/pdf/10.1002/2015GL067416>. URL: <https://agupubs.onlinelibrary.wiley.com/doi/abs/10.1002/2015GL067416>.
- Myers, Timothy A., Ryan C. Scott, Mark D. Zelinka, Stephen A. Klein, Joel R. Norris, and Peter M. Caldwell (June 2021). "Observational constraints on low cloud feedback reduce uncertainty of climate sensitivity." *Nature Climate Change* 11.6, pp. 501–507. ISSN: 1758-6798. DOI: 10.1038/s41558-021-01039-0. URL: <https://doi.org/10.1038/s41558-021-01039-0>.
- Nam, C., S. Bony, J.-L. Dufresne, and H. Chepfer (2012). "The 'too few, too bright' tropical low-cloud problem in CMIP5 models." *Geophysical Research Letters* 39.21. DOI: <https://doi.org/10.1029/2012GL053421>. eprint: <https://agupubs.onlinelibrary.wiley.com/doi/pdf/10.1029/2012GL053421>. URL: <https://agupubs.onlinelibrary.wiley.com/doi/abs/10.1029/2012GL053421>.
- Neggers, R. A. J. (2015). "Exploring bin-macrophysics models for moist convective transport and clouds." *Journal of Advances in Modeling Earth Systems* 7.4, pp. 2079–2104. DOI: 10.1002/2015MS000502. eprint: <https://agupubs.onlinelibrary.wiley.com/doi/pdf/10.1002/2015MS000502>. URL: <https://agupubs.onlinelibrary.wiley.com/doi/abs/10.1002/2015MS000502>.
- Neggers, R. A. J., H. J. J. Jonker, and A. P. Siebesma (2003). "Size Statistics of Cumulus Cloud Populations in Large-Eddy Simulations." *Journal of the Atmospheric Sciences* 60.8, pp. 1060–1074. DOI: 10.1175/1520-0469(2003)60<1060:SSOCCP>2.0.CO;2. eprint: [http://dx.doi.org/10.1175/1520-0469\(2003\)60<1060:SSOCCP>2.0.CO;2](http://dx.doi.org/10.1175/1520-0469(2003)60<1060:SSOCCP>2.0.CO;2). URL: [http://dx.doi.org/10.1175/1520-0469\(2003\)60<1060:SSOCCP>2.0.CO;2](http://dx.doi.org/10.1175/1520-0469(2003)60<1060:SSOCCP>2.0.CO;2).
- Norris, Joel R. and Sam F. Iacobellis (2005). "North Pacific Cloud Feedbacks Inferred from Synoptic-Scale Dynamic and Thermodynamic Relationships." *Journal of Climate* 18.22, pp. 4862–4878. DOI: 10.1175/JCLI3558.1. eprint: <https://doi.org/10.1175/JCLI3558.1>. URL: <https://doi.org/10.1175/JCLI3558.1>.
- Nuijens, L., I. Serikov, L. Hirsch, K. Lonitz, and B. Stevens (2014). "The distribution and variability of low-level cloud in the North Atlantic trades." *Quarterly Journal of the Royal Meteorological Society* 140.684, pp. 2364–2374. ISSN: 1477-870X. DOI: 10.1002/qj.2307. URL: <http://dx.doi.org/10.1002/qj.2307>.
- Nuijens, Louise, Brian Medeiros, Irina Sandu, and Maike Ahlgrimm (2015). "Observed and modeled patterns of covariability between low-level cloudiness and the structure of the trade-wind layer." *Journal of Advances in Modeling Earth Systems* 7.4, pp. 1741–1764. ISSN: 1942-2466. DOI: 10.1002/2015MS000483. URL: <http://dx.doi.org/10.1002/2015MS000483>.
- Nuijens, Louise and Bjorn Stevens (2012). "The Influence of Wind Speed on Shallow Marine Cumulus Convection." *Journal of the Atmospheric Sciences* 69.1, pp. 168–184. DOI: 10.1175/JAS-D-11-02.1. eprint: <http://dx.doi.org/10.1175/JAS-D-11-02.1>. URL: <http://dx.doi.org/10.1175/JAS-D-11-02.1>.

- Nuijens, Louise, Bjorn Stevens, and A. Pier Siebesma (2009). "The Environment of Precipitating Shallow Cumulus Convection." *Journal of the Atmospheric Sciences* 66.7, pp. 1962–1979. DOI: [10.1175/2008JAS2841.1](https://doi.org/10.1175/2008JAS2841.1). eprint: <http://dx.doi.org/10.1175/2008JAS2841.1>. URL: <http://dx.doi.org/10.1175/2008JAS2841.1>.
- Parzen, Emanuel (1962). "On Estimation of a Probability Density Function and Mode." *The Annals of Mathematical Statistics* 33.3, pp. 1065–1076. DOI: [10.1214/aoms/1177704472](https://doi.org/10.1214/aoms/1177704472). URL: <https://doi.org/10.1214/aoms/1177704472>.
- Peters, Ole, J. David Neelin, and Stephen W. Nesbitt (2009). "Mesoscale Convective Systems and Critical Clusters." *Journal of the Atmospheric Sciences* 66.9, pp. 2913–2924. DOI: [10.1175/2008JAS2761.1](https://doi.org/10.1175/2008JAS2761.1). eprint: <http://dx.doi.org/10.1175/2008JAS2761.1>. URL: <http://dx.doi.org/10.1175/2008JAS2761.1>.
- Plank, Vernon G. (1969). "The Size Distribution of Cumulus Clouds in Representative Florida Populations." *Journal of Applied Meteorology* 8.1, pp. 46–67. DOI: [10.1175/1520-0450\(1969\)008<0046:TSD0CC>2.0.CO;2](https://doi.org/10.1175/1520-0450(1969)008<0046:TSD0CC>2.0.CO;2). eprint: [https://doi.org/10.1175/1520-0450\(1969\)008<0046:TSD0CC>2.0.CO;2](https://doi.org/10.1175/1520-0450(1969)008<0046:TSD0CC>2.0.CO;2). URL: [https://doi.org/10.1175/1520-0450\(1969\)008<0046:TSD0CC>2.0.CO;2](https://doi.org/10.1175/1520-0450(1969)008<0046:TSD0CC>2.0.CO;2).
- Qu, Xin, Alex Hall, Stephen A. Klein, and Anthony M. DeAngelis (2015). "Positive tropical marine low-cloud cover feedback inferred from cloud-controlling factors." *Geophysical Research Letters* 42.18, pp. 7767–7775. DOI: [10.1002/2015GL065627](https://doi.org/10.1002/2015GL065627). eprint: <https://agupubs.onlinelibrary.wiley.com/doi/pdf/10.1002/2015GL065627>. URL: <https://agupubs.onlinelibrary.wiley.com/doi/abs/10.1002/2015GL065627>.
- Quaas, J. et al. (2020). "Constraining the Twomey effect from satellite observations: issues and perspectives." *Atmospheric Chemistry and Physics* 20.23, pp. 15079–15099. DOI: [10.5194/acp-20-15079-2020](https://doi.org/10.5194/acp-20-15079-2020). URL: <https://acp.copernicus.org/articles/20/15079/2020/>.
- Quaas, Johannes, Olivier Boucher, Nicolas Bellouin, and Stefan Kinne (2008). "Satellite-based estimate of the direct and indirect aerosol climate forcing." *Journal of Geophysical Research: Atmospheres* 113.D5. DOI: <https://doi.org/10.1029/2007JD008962>. eprint: <https://agupubs.onlinelibrary.wiley.com/doi/pdf/10.1029/2007JD008962>. URL: <https://agupubs.onlinelibrary.wiley.com/doi/abs/10.1029/2007JD008962>.
- Rasch, P. J. and J. E. Kristjansson (1998). "A Comparison of the CCM3 Model Climate Using Diagnosed and Predicted Condensate Parameterizations." *Journal of Climate* 11.7, pp. 1587–1614. DOI: [10.1175/1520-0442\(1998\)011<1587:ACOTCM>2.0.CO;2](https://doi.org/10.1175/1520-0442(1998)011<1587:ACOTCM>2.0.CO;2). eprint: [https://doi.org/10.1175/1520-0442\(1998\)011<1587:ACOTCM>2.0.CO;2](https://doi.org/10.1175/1520-0442(1998)011<1587:ACOTCM>2.0.CO;2). URL: [https://doi.org/10.1175/1520-0442\(1998\)011<1587:ACOTCM>2.0.CO;2](https://doi.org/10.1175/1520-0442(1998)011<1587:ACOTCM>2.0.CO;2).
- Rieck, Malte, Louise Nuijens, and Bjorn Stevens (2012). "Marine Boundary Layer Cloud Feedbacks in a Constant Relative Humidity Atmosphere." *Journal of the Atmospheric Sciences* 69.8, pp. 2538–2550. DOI: [10.1175/JAS-D-11-0203.1](https://doi.org/10.1175/JAS-D-11-0203.1). eprint:

- <https://doi.org/10.1175/JAS-D-11-0203.1>. URL: <https://doi.org/10.1175/JAS-D-11-0203.1>.
- Rosenblatt, Murray (1956). "Remarks on Some Nonparametric Estimates of a Density Function." *The Annals of Mathematical Statistics* 27.3, pp. 832–837. DOI: [10.1214/aoms/1177728190](https://doi.org/10.1214/aoms/1177728190). URL: <https://doi.org/10.1214/aoms/1177728190>.
- Sakradzija, Mirjana and Cathy Hohenegger (2017). "What Determines the Distribution of Shallow Convective Mass Flux through a Cloud Base?" *Journal of the Atmospheric Sciences* 74.8, pp. 2615–2632. DOI: [10.1175/JAS-D-16-0326.1](https://doi.org/10.1175/JAS-D-16-0326.1). eprint: <https://doi.org/10.1175/JAS-D-16-0326.1>. URL: <https://doi.org/10.1175/JAS-D-16-0326.1>.
- Sandu, Irina and Bjorn Stevens (2011). "On the Factors Modulating the Stratocumulus to Cumulus Transitions." *Journal of the Atmospheric Sciences* 68.9, pp. 1865–1881. DOI: [10.1175/2011JAS3614.1](https://doi.org/10.1175/2011JAS3614.1). eprint: <https://doi.org/10.1175/2011JAS3614.1>. URL: <https://doi.org/10.1175/2011JAS3614.1>.
- Schulz, Hauke, Ryan M Eastman, and Bjorn Stevens (2021). "Characterization and Evolution of Organized Shallow Convection in the Trades." *Earth and Space Science Open Archive*, p. 34. DOI: [10.1002/essoar.10505836.1](https://doi.org/10.1002/essoar.10505836.1). URL: <https://doi.org/10.1002/essoar.10505836.1>.
- Seifert, Axel, Thijs Heus, Robert Pincus, and Bjorn Stevens (2015). "Large-eddy simulation of the transient and near-equilibrium behavior of precipitating shallow convection." *Journal of Advances in Modeling Earth Systems* 7.4, pp. 1918–1937. DOI: <https://doi.org/10.1002/2015MS000489>. eprint: <https://agupubs.onlinelibrary.wiley.com/doi/pdf/10.1002/2015MS000489>. URL: <https://agupubs.onlinelibrary.wiley.com/doi/abs/10.1002/2015MS000489>.
- Sengupta, S. K., R. M. Welch, M. S. Navar, T. A. Berendes, and D. W. Chen (1990). "Cumulus Cloud Field Morphology and Spatial Patterns Derived from High Spatial Resolution Landsat Imagery." *Journal of Applied Meteorology* 29.12, pp. 1245–1267. DOI: [10.1175/1520-0450\(1990\)029<1245:CCFMAS>2.0.CO;2](https://doi.org/10.1175/1520-0450(1990)029<1245:CCFMAS>2.0.CO;2). eprint: [https://doi.org/10.1175/1520-0450\(1990\)029<1245:CCFMAS>2.0.CO;2](https://doi.org/10.1175/1520-0450(1990)029<1245:CCFMAS>2.0.CO;2). URL: [https://doi.org/10.1175/1520-0450\(1990\)029<1245:CCFMAS>2.0.CO;2](https://doi.org/10.1175/1520-0450(1990)029<1245:CCFMAS>2.0.CO;2).
- Slingo, J. M. (1987). "The Development and Verification of A Cloud Prediction Scheme For the Ecmwf Model." *Quarterly Journal of the Royal Meteorological Society* 113.477, pp. 899–927. DOI: [10.1002/qj.49711347710](https://doi.org/10.1002/qj.49711347710). eprint: <https://rmets.onlinelibrary.wiley.com/doi/pdf/10.1002/qj.49711347710>. URL: <https://rmets.onlinelibrary.wiley.com/doi/abs/10.1002/qj.49711347710>.
- Stamnes, Knut, Gary E. Thomas, and Jakob J. Stamnes (2017). *Radiative Transfer in the Atmosphere and Ocean*. 2nd ed. Cambridge University Press. DOI: [10.1017/9781316148549](https://doi.org/10.1017/9781316148549).
- Stein, T. H. M., C. E. Holloway, I. Tobin, and S. Bony (2017). "Observed Relationships between Cloud Vertical Structure and Convective Aggregation over Tropical

- Ocean." *Journal of Climate* 30.6, pp. 2187–2207. DOI: [10.1175/JCLI-D-16-0125.1](https://doi.org/10.1175/JCLI-D-16-0125.1). eprint: <https://doi.org/10.1175/JCLI-D-16-0125.1>. URL: <https://doi.org/10.1175/JCLI-D-16-0125.1>.
- Stevens, B. et al. (2021). "EUREC⁴A." *Earth System Science Data Discussions* 2021, pp. 1–78. DOI: [10.5194/essd-2021-18](https://doi.org/10.5194/essd-2021-18). URL: <https://essd.copernicus.org/preprints/essd-2021-18/>.
- Stevens, Bjorn (2005). "ATMOSPHERIC MOIST CONVECTION." *Annual Review of Earth and Planetary Sciences* 33.1, pp. 605–643. DOI: [10.1146/annurev.earth.33.092203.122658](https://doi.org/10.1146/annurev.earth.33.092203.122658). eprint: <https://doi.org/10.1146/annurev.earth.33.092203.122658>. URL: <https://doi.org/10.1146/annurev.earth.33.092203.122658>.
- Stevens, Bjorn and Sandrine Bony (2013). "What Are Climate Models Missing?" *Science* 340.6136, pp. 1053–1054. ISSN: 0036-8075. DOI: [10.1126/science.1237554](https://doi.org/10.1126/science.1237554). eprint: <https://science.sciencemag.org/content/340/6136/1053.full.pdf>. URL: <https://science.sciencemag.org/content/340/6136/1053>.
- Stevens, Bjorn, Hélène Brogniez, Christoph Kiemle, Jean-Lionel Lacour, Cyril Crevoisier, and Johannes Kiliani (2018). "Structure and Dynamical Influence of Water Vapor in the Lower Tropical Troposphere." In: *Shallow Clouds, Water Vapor, Circulation, and Climate Sensitivity*. Ed. by Robert Pincus, David Winker, Sandrine Bony, and Bjorn Stevens. Cham: Springer International Publishing, pp. 199–225. ISBN: 978-3-319-77273-8. DOI: [10.1007/978-3-319-77273-8_10](https://doi.org/10.1007/978-3-319-77273-8_10). URL: https://doi.org/10.1007/978-3-319-77273-8_10.
- Stevens, Bjorn and Graham Feingold (Oct. 2009). "Untangling aerosol effects on clouds and precipitation in a buffered system." *Nature* 461.7264, pp. 607–613. ISSN: 1476-4687. DOI: [10.1038/nature08281](https://doi.org/10.1038/nature08281). URL: <https://doi.org/10.1038/nature08281>.
- Stevens, Bjorn et al. (2016). "The Barbados Cloud Observatory: Anchoring Investigations of Clouds and Circulation on the Edge of the ITCZ." *Bulletin of the American Meteorological Society* 97.5, pp. 787–801. DOI: [10.1175/BAMS-D-14-00247.1](https://doi.org/10.1175/BAMS-D-14-00247.1). URL: <https://journals.ametsoc.org/view/journals/bams/97/5/bams-d-14-00247.1.xml>.
- Stevens, Bjorn et al. (2019). "A High-Altitude Long-Range Aircraft Configured as a Cloud Observatory: The NARVAL Expeditions." *Bulletin of the American Meteorological Society* 100.6, pp. 1061–1077. DOI: [10.1175/BAMS-D-18-0198.1](https://doi.org/10.1175/BAMS-D-18-0198.1). URL: <https://journals.ametsoc.org/view/journals/bams/100/6/bams-d-18-0198.1.xml>.
- Stevens, Bjorn et al. (2020). "Sugar, gravel, fish and flowers: Mesoscale cloud patterns in the trade winds." *Quarterly Journal of the Royal Meteorological Society* 146.726, pp. 141–152. DOI: <https://doi.org/10.1002/qj.3662>. eprint: <https://rmets.onlinelibrary.wiley.com/doi/pdf/10.1002/qj.3662>. URL: <https://rmets.onlinelibrary.wiley.com/doi/abs/10.1002/qj.3662>.

- Su, W., J. Corbett, Z. Eitzen, and L. Liang (2015). "Next-generation angular distribution models for top-of-atmosphere radiative flux calculation from CERES instruments: methodology." *Atmospheric Measurement Techniques* 8.2, pp. 611–632. DOI: [10.5194/amt-8-611-2015](https://doi.org/10.5194/amt-8-611-2015). URL: <https://amt.copernicus.org/articles/8/611/2015/>.
- Tobin, Isabelle, Sandrine Bony, Chris E. Holloway, Jean-Yves Grandpeix, Geneviève Sèze, David Coppin, Steve J. Woolnough, and Rémy Roca (2013). "Does convective aggregation need to be represented in cumulus parameterizations?" *Journal of Advances in Modeling Earth Systems* 5.4, pp. 692–703. ISSN: 1942-2466. DOI: [10.1002/jame.20047](https://doi.org/10.1002/jame.20047). URL: <http://dx.doi.org/10.1002/jame.20047>.
- Tobin, Isabelle, Sandrine Bony, and Remy Roca (2012). "Observational Evidence for Relationships between the Degree of Aggregation of Deep Convection, Water Vapor, Surface Fluxes, and Radiation." *Journal of Climate* 25.20, pp. 6885–6904. DOI: [10.1175/JCLI-D-11-00258.1](https://doi.org/10.1175/JCLI-D-11-00258.1). eprint: <http://dx.doi.org/10.1175/JCLI-D-11-00258.1>. URL: <http://dx.doi.org/10.1175/JCLI-D-11-00258.1>.
- Tompkins, Adrian M. and Addisu G. Semie (2017). "Organization of tropical convection in low vertical wind shears: Role of updraft entrainment." *Journal of Advances in Modeling Earth Systems* 9.2, pp. 1046–1068. DOI: [10.1002/2016MS000802](https://doi.org/10.1002/2016MS000802). eprint: <https://agupubs.onlinelibrary.wiley.com/doi/pdf/10.1002/2016MS000802>. URL: <https://agupubs.onlinelibrary.wiley.com/doi/abs/10.1002/2016MS000802>.
- Twomey, S. (1959). "The nuclei of natural cloud formation part II: The supersaturation in natural clouds and the variation of cloud droplet concentration." *Geofisica pura e applicata* 43.1, pp. 243–249. ISSN: 1420-9136. DOI: [10.1007/BF01993560](https://doi.org/10.1007/BF01993560). URL: <https://doi.org/10.1007/BF01993560>.
- Vial, Jessica, Sandrine Bony, Jean-Louis Dufresne, and Romain Roehrig (2016). "Coupling between lower-tropospheric convective mixing and low-level clouds: Physical mechanisms and dependence on convection scheme." *Journal of Advances in Modeling Earth Systems* 8.4, pp. 1892–1911. DOI: <https://doi.org/10.1002/2016MS000740>. eprint: <https://agupubs.onlinelibrary.wiley.com/doi/pdf/10.1002/2016MS000740>. URL: <https://agupubs.onlinelibrary.wiley.com/doi/abs/10.1002/2016MS000740>.
- Vial, Jessica, Sandrine Bony, Bjorn Stevens, and Raphaela Vogel (2018). "Mechanisms and Model Diversity of Trade-Wind Shallow Cumulus Cloud Feedbacks: A Review." In: *Shallow Clouds, Water Vapor, Circulation, and Climate Sensitivity*. Ed. by Robert Pincus, David Winker, Sandrine Bony, and Bjorn Stevens. Cham: Springer International Publishing, pp. 159–181. ISBN: 978-3-319-77273-8. DOI: [10.1007/978-3-319-77273-8_8](https://doi.org/10.1007/978-3-319-77273-8_8). URL: https://doi.org/10.1007/978-3-319-77273-8_8.
- Vial, Jessica, Jean-Louis Dufresne, and Sandrine Bony (Dec. 2013). "On the interpretation of inter-model spread in CMIP5 climate sensitivity estimates." *Climate*

- Dynamics* 41.11, pp. 3339–3362. ISSN: 1432-0894. DOI: [10.1007/s00382-013-1725-9](https://doi.org/10.1007/s00382-013-1725-9). URL: <https://doi.org/10.1007/s00382-013-1725-9>.
- Várnai, Tamás and Alexander Marshak (2003). “A method for analyzing how various parts of clouds influence each other’s brightness.” *Journal of Geophysical Research: Atmospheres* 108.D22. DOI: <https://doi.org/10.1029/2003JD003561>. eprint: <https://agupubs.onlinelibrary.wiley.com/doi/pdf/10.1029/2003JD003561>. URL: <https://agupubs.onlinelibrary.wiley.com/doi/abs/10.1029/2003JD003561>.
- Warren, Stephen G., Carole J. Hahn, and Julius London (1985). “Simultaneous Occurrence of Different Cloud Types.” *Journal of Applied Meteorology and Climatology* 24.7, pp. 658–667. DOI: [10.1175/1520-0450\(1985\)024<0658:S00DCT>2.0.CO;2](https://doi.org/10.1175/1520-0450(1985)024<0658:S00DCT>2.0.CO;2). URL: https://journals.ametsoc.org/view/journals/apme/24/7/1520-0450_1985_024_0658_soodct_2_0_co_2.xml.
- Weger, R. C., J. Lee, Tianri Zhu, and R. M. Welch (1992). “Clustering, randomness and regularity in cloud fields: 1. Theoretical considerations.” *Journal of Geophysical Research: Atmospheres* 97.D18, pp. 20519–20536. DOI: [10.1029/92JD02038](https://doi.org/10.1029/92JD02038). eprint: <https://agupubs.onlinelibrary.wiley.com/doi/pdf/10.1029/92JD02038>. URL: <https://agupubs.onlinelibrary.wiley.com/doi/abs/10.1029/92JD02038>.
- Werner, F., G. Wind, Z. Zhang, S. Platnick, L. Di Girolamo, G. Zhao, N. Amarasinghe, and K. Meyer (2016). “Marine boundary layer cloud property retrievals from high-resolution ASTER observations: case studies and comparison with Terra MODIS.” *Atmospheric Measurement Techniques* 9.12, pp. 5869–5894. DOI: [10.5194/amt-9-5869-2016](https://doi.org/10.5194/amt-9-5869-2016). URL: <https://amt.copernicus.org/articles/9/5869/2016/>.
- Wielicki, Bruce A. and Lindsay Parker (1992). “On the determination of cloud cover from satellite sensors: The effect of sensor spatial resolution.” *Journal of Geophysical Research: Atmospheres* 97.D12, pp. 12799–12823. DOI: <https://doi.org/10.1029/92JD01061>. eprint: <https://agupubs.onlinelibrary.wiley.com/doi/pdf/10.1029/92JD01061>. URL: <https://agupubs.onlinelibrary.wiley.com/doi/abs/10.1029/92JD01061>.
- Wielicki, Bruce A. and Ronald M. Welch (1986). “Cumulus Cloud Properties Derived Using Landsat Satellite Data.” *Journal of Climate and Applied Meteorology* 25.3, pp. 261–276. DOI: [10.1175/1520-0450\(1986\)025<0261:CCPDUL>2.0.CO;2](https://doi.org/10.1175/1520-0450(1986)025<0261:CCPDUL>2.0.CO;2). eprint: [http://dx.doi.org/10.1175/1520-0450\(1986\)025<0261:CCPDUL>2.0.CO;2](http://dx.doi.org/10.1175/1520-0450(1986)025<0261:CCPDUL>2.0.CO;2). URL: [http://dx.doi.org/10.1175/1520-0450\(1986\)025<0261:CCPDUL>2.0.CO;2](http://dx.doi.org/10.1175/1520-0450(1986)025<0261:CCPDUL>2.0.CO;2).
- Winker, David M., Mark A. Vaughan, Ali Omar, Yongxiang Hu, Kathleen A. Powell, Zhaoyan Liu, William H. Hunt, and Stuart A. Young (2009). “Overview of the CALIPSO Mission and CALIOP Data Processing Algorithms.” *Journal of Atmospheric and Oceanic Technology* 26.11, pp. 2310–2323. DOI: [10.1175/2009jtech1281.1](https://doi.org/10.1175/2009jtech1281.1). URL: <https://doi.org/10.1175/2009jtech1281.1>.

- Wirth, Martin, Andreas Fix, Peter Mahnke, Horst Schwarzer, Friedrich Schrandt, and Gerhard Ehret (2009). "The airborne multi-wavelength water vapor differential absorption lidar WALES: system design and performance." *Applied Physics B* 96, pp. 201–213. URL: <https://elib.dlr.de/58175/>.
- Wood, Robert and Christopher S. Bretherton (2006). "On the Relationship between Stratiform Low Cloud Cover and Lower-Tropospheric Stability." *Journal of Climate* 19.24, pp. 6425–6432. DOI: [10.1175/JCLI3988.1](https://doi.org/10.1175/JCLI3988.1). eprint: <http://dx.doi.org/10.1175/JCLI3988.1>. URL: <http://dx.doi.org/10.1175/JCLI3988.1>.
- Xue, Huiwen and Graham Feingold (2006). "Large-Eddy Simulations of Trade Wind Cumuli: Investigation of Aerosol Indirect Effects." *Journal of the Atmospheric Sciences* 63.6, pp. 1605–1622. DOI: [10.1175/JAS3706.1](https://doi.org/10.1175/JAS3706.1). URL: <https://journals.ametsoc.org/view/journals/atsc/63/6/jas3706.1.xml>.
- Yamaguchi, Y., A. B. Kahle, H. Tsu, T. Kawakami, and M. Pniel (1998). "Overview of Advanced Spaceborne Thermal Emission and Reflection Radiometer (ASTER)." *IEEE Transactions on Geoscience and Remote Sensing* 36.4, pp. 1062–1071. ISSN: 0196-2892. DOI: [10.1109/36.700991](https://doi.org/10.1109/36.700991).
- Yang, Kang, Huaguo Zhang, Bin Fu, Gang Zheng, Weibing Guan, Aiqin Shi, and Dongling Li (2015). "Observation of submarine sand waves using ASTER stereo sun glitter imagery." *International Journal of Remote Sensing* 36.22, pp. 5576–5592. DOI: [10.1080/01431161.2015.1101652](https://doi.org/10.1080/01431161.2015.1101652). eprint: <https://doi.org/10.1080/01431161.2015.1101652>. URL: <https://doi.org/10.1080/01431161.2015.1101652>.
- Zelinka, Mark D., Timothy A. Myers, Daniel T. McCoy, Stephen Po-Chedley, Peter M. Caldwell, Paulo Ceppi, Stephen A. Klein, and Karl E. Taylor (2020). "Causes of Higher Climate Sensitivity in CMIP6 Models." *Geophysical Research Letters* 47.1. e2019GL085782 [10.1029/2019GL085782](https://doi.org/10.1029/2019GL085782), e2019GL085782. DOI: <https://doi.org/10.1029/2019GL085782>. eprint: <https://agupubs.onlinelibrary.wiley.com/doi/pdf/10.1029/2019GL085782>. URL: <https://agupubs.onlinelibrary.wiley.com/doi/abs/10.1029/2019GL085782>.
- Zhao, Guangyu and Larry Di Girolamo (2006). "Cloud fraction errors for trade wind cumuli from EOS-Terra instruments." *Geophysical Research Letters* 33.20. DOI: <https://doi.org/10.1029/2006GL027088>. eprint: <https://agupubs.onlinelibrary.wiley.com/doi/pdf/10.1029/2006GL027088>. URL: <https://agupubs.onlinelibrary.wiley.com/doi/abs/10.1029/2006GL027088>.
- Zhao, Guangyu and Larry Di Girolamo (2007). "Statistics on the macrophysical properties of trade wind cumuli over the tropical western Atlantic." *Journal of Geophysical Research: Atmospheres* 112.D10. D10204, n/a–n/a. ISSN: 2156-2202. DOI: [10.1029/2006JD007371](https://doi.org/10.1029/2006JD007371). URL: <http://dx.doi.org/10.1029/2006JD007371>.

VERSICHERUNG AN EIDES STATT

Declaration of oath

Hiermit versichere ich an Eides statt, dass ich die vorliegende Dissertation mit dem Titel: „Small and optically thin clouds in the trades “ selbstständig verfasst und keine anderen als die angegebenen Hilfsmittel – insbesondere keine im Quellenverzeichnis nicht benannten Internet-Quellen – benutzt habe. Alle Stellen, die wörtlich oder sinngemäß aus Veröffentlichungen entnommen wurden, sind als solche kenntlich gemacht. Ich versichere weiterhin, dass ich die Dissertation oder Teile davon vorher weder im In- noch im Ausland in einem anderen Prüfungsverfahren eingereicht habe und die eingereichte schriftliche Fassung der auf dem elektronischen Speichermedium entspricht.

Hamburg, July 2021

Theresa Mieslinger